UNIVERSITY COLLEGE LONDON

DEPARTMENT OF PHYSICS AND ASTRONOMY

Thesis submitted for the degree

Doctor of Philosophy (PhD)

Defended by

Simon Nathan Ernleigh WARD

Spin ladder physics and the effect of random bond disorder

Thesis Supervisor: Prof Christian RÜEGG

Thesis Advisor: Prof Desmond F. MCMORROW

Referees :

Prof A. GREEN - University College London

Dr C. STOCK - University of Edinburgh

September 2014

I, Simon Ward confirm that the work presented in this thesis is my own. Where information has been derived from other sources, I confirm that this has been indicated in the thesis.

Simon Ward	Date

Chapter 1

Abstract

This PhD thesis concerns the physics of low-dimensional quantum systems and especially quantum spin ladders. Novel metal-organic compounds $(C_5H_{12}N)_2CuBr_4$ and $(C_5H_{12}N)_2CuCl_4$ are investigated as model materials for low-dimensional quantum behaviour by neutron scattering experiments and by measurements of magnetic and thermodynamic properties. The experimental results are compared quantitatively to calculations using a variety of theoretical and numerical methods (DMRG, ED) of the ground state and excitations of such systems. Key results are the determination of the Hamiltonian and its exchange parameters of $(C_5H_{12}N)_2CuCl_4$ studied here for the first time from quantitative modelling of magnetic susceptibility and neutron spectroscopy data. When a magnetic field is applied two quantum critical points occur at which fractionalization of the elementary quasi-particle excitations is observed. The characteristic excitation continua are explained by effective spin-chain and t-J models and are observed systematically as a function of magnetic field and temperature. Coherent and incoherent spin Luttinger-liquid physics is observed and for the first time modelled fully quantitatively.

The chemical flexibility of the these metal-organic compounds allows continuous solid-state mixtures of Br and Cl resulting in systems with quenched disorder. The rung and leg exchange parameters assume discrete values given by the specific chemical composition of the exchange pathways. The influence of such quenched disorder on the excitations of quantum spin ladders has been studied experimentally. The observed spectra with damped excitations of the unperturbed ladder and more localized modes provide detailed insights into the physics that may be observed in such systems if a magnetic field is applied and so called Bose glass phases are induced.

List of Figures

List of Tables

Contents

Chapter 2

Introduction

Contents

2.1 Quantum magnetism and phase transitions

Quantum magnetism can be defined as the quantum treatment of spin defined by the intrinsic angular momentum operator $\hat{S}$. The size of $\hat{S}$ is quantised into integer and half integer vales (S) with a total length given by $\sqrt{S(S+1)}$. All Cartesian components of $\hat{S}$ cannot be simultaneously measured and is instead described by a wave function which is made up of the product of individual states $|\Psi\rangle$ with spacial (ψ) and spin (χ) components. For an arbitrary operator S_z, a state $|m\rangle$ has an associated probability of being observable, $S_z|m\rangle = m|m\rangle$ and an expectation value of $\langle m|S_z|m\rangle$.

This can be expressed by a simple two S = 1/2 system where the particles are indistinguishable. The Hamiltonian for such a system is,

$$\mathcal{H} = J\mathbf{S}_1 \cdot \mathbf{S}_2, \tag{2.1}$$

where J is a rotationally invariant Heisenberg exchange matrix. When considered in terms of quantum operators a basis is selected (for example S_z), each spin can have $|\uparrow\rangle$ and $|\downarrow\rangle$ values. By superposition the combined spin states are;

$$|s\rangle = 1/\sqrt{2}\left(|\uparrow\downarrow\rangle - |\downarrow\uparrow\rangle\right), \ \left|t^0\right\rangle = 1/\sqrt{2}\left(|\uparrow\downarrow\rangle + |\downarrow\uparrow\rangle\right), \ \left|t^+\right\rangle = |\downarrow\downarrow\rangle, \ \left|t^-\right\rangle = |\uparrow\uparrow\rangle, \tag{2.2}$$

The groundstate has total spin 0 and is called a singlet with energy $-3/4J$. The other states have a total spin of 1 and energy $J/4$ and are degenerate. These states are called the singlet and triplet states and are a spin dimer. These form the building blocks for more complex spin configurations.

In systems which have structural dimerisation an exchange network exists, typically with a dominant exchange[a]. This dominant exchange can enforce singlet formation and suppress long range order. When temperatures are reduced competition between the thermal fluctuations and singlet formation, with singlet formation favoured below the temperature of the dominant exchange. This competition leads to an easing of phases rather than a sharp transition. Structural dimerisation can occur in any dimension, it occurs in the 3D exchange network of $TlCuCl_3$ [1], in 2D with $BaCuSi_20_6$ [2] and in 1D with the compound of this thesis BPCC.

The strength of the quantum fluctuations in a system are determined by spin and co-ordination number. If we consider the quantum corrections for classical energy ($\approx 1/S$) we find that for S = 1/2 and an ensemble of spins with co-ordination number z, the ratio $1/(Sz)$ describing the quantum fluctuations is maximised for low z [3]. This means that for a S = 1/2 and one dimension, quantum fluctuations are maximised. This is true for an individual spin and due to the mixing of states in a many body system, the ensemble as well. In one dimension these fluctuations are so strong that magnetic order is prevented from forming, even at T = 0.

In a classical phase transition it is the thermal fluctuations in the order parameter which drive the system from one state to another. As temperature increases, the thermal fluctuations in the order parameter increase and the disorder in the system increases. The thermally driven fluctuations in the order parameter can not occur at T = 0, so if a phase transition occurs, it is due to other fluctuations. These fluctuations are quantum fluctuations due to zero point fluctuations from the Heisenberg uncertainty principle. The fluctuations couple to a control parameter which continuously or discretely tuned across a phase boundary. The effect on

[a] We restrict ourselves to an antiferromagnetic exchange with S = 1/2 dimers for this argument.

quantum fluctuations of this control parameter g scales at $1/g$ [4]. The existence of a phase transition at T = 0, is called a quantum phase transition and the point separating the two phases is the quantum critical point.

The control parameter for a quantum phase transition can be magnetic field, hydrostatic pressure or chemical doping. For this work, magnetic field will be the control parameter.

It is important to note that around the vicinity of the quantum critical point physical properties can be described by universality classes. In this region the physics is described by scaling functions which are independent of material properties and rely on only the control parameter and the dimensionality of the system [5].

2.2 Spin ladder physics

The spin ladder is a geometry of spins which are connected with two sets of exchanges, called the rung and leg exchange. For an even legged ladder the ground state is a dimerised singlet state on the rung and hence has a spin gap. Ladders with an odd number of legs are gapless due to the inability of all spins to form singlets, leaving a chain like spin configuration. This has been numerically studied in reference [6]. For the case of a ladder with 2-legs, the spin geometry is shown in figure 2.1.

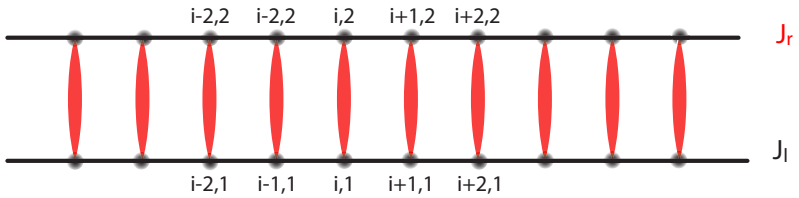

Figure 2.1: Schematic representation of exchange interactions in a spin ladder. Spins are shown as grey circles, black lines represent leg exchange and red ovals rung exchanges.

The simplest Hamiltonian for the spin ladder is;

$$\mathcal{H} = J_r \sum_{i=1}^{L} \mathbf{S}_{i,1} \cdot \mathbf{S}_{i,2} + J_l \sum_{j=1,2} \sum_{i=1}^{L-1} \mathbf{S}_{i,j} \cdot \mathbf{S}_{i+1,j} - g\mu_B h^z. \tag{2.3}$$

The generic two leg spin ladder phase diagram with weak inter-ladder exchange is shown in figure 2.2. There are 5 distinct phases which are explained below;

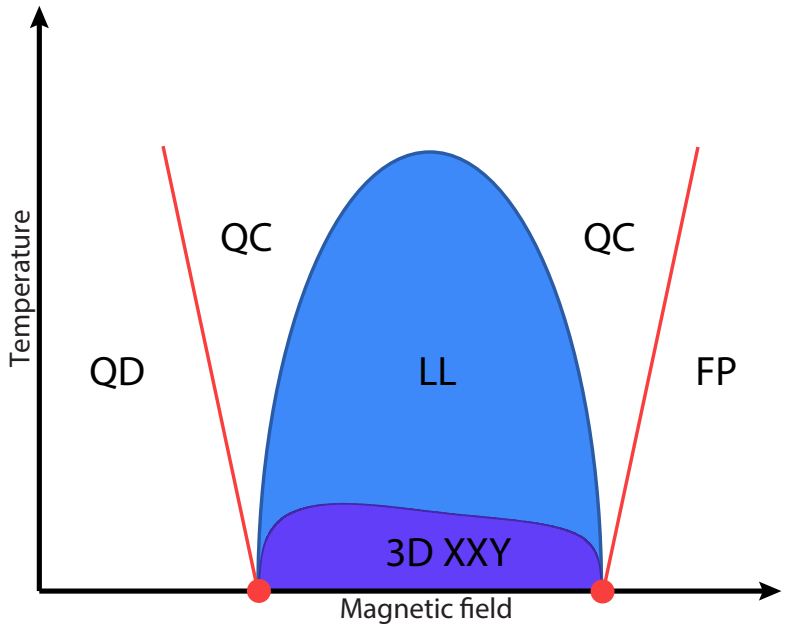

Figure 2.2: Generic phase diagram for a 2-leg spin ladder. Five phases are identified and described in the text. Filled red circles correspond to quantum critical points and phase boundaries are solid lines. It is noted that the phase boundaries in reality are continuous and not discreet as shown.

QD - Quantum disordered

The quantum disordered phase is characterised by singlet-triplet excitations with an energy gap Δ. The quantum fluctuations in this phase prevent long range order and correlations are short range. The triplet state undergoes Zeeman splitting in a finite magnetic field, with the $|t^+\rangle$ state softening. When the gap is closed a quantum critical point (H_c) occurs, the magnetic field creating triplons with finite magnetisation.

LL - Luttinger-liquid

In the spin Luttinger-liquid phase excitations are collective due to the hard-

core constraint of a triplon. The excitation spectrum is gapless, where a triplon undergoes fractionalization into two elementary and deconfined spinons. These can be described by Luttinger-liquid theory. High energy excitations can be thought of as spin and hole excitations which can be mapped to a t-J model. The density of triplons in this phase are controlled by the applied field. At the saturation field a quantum critical point occurs and the field polarised phase is entered.

3D XXY

The 3D XXY phase is a consequence of the finite coupling between ladders. In this phase the triplons undergo Bose Einstein condensation and order magnetically. This occurs at temperatures on the order of the inter-ladder coupling J'.

FP - Field polarised

In the field polarised phase all magnetic moments are aligned with the applied magnetic field. Excitations are spin-waves which have a field dependent gap energy due to the reopening of the single-triplet gap.

QC - Quantum critical

The quantum critical region is the area where the thermal energy is greater than that of the gap. In this region quantum and thermal fluctuations compete and are equally important. Around this region physics is governed by critical scaling.

The 3D XXZ phase introduced above can be treated with an extension of the basic Hamiltonian by using the mean-field approximation [7]. The mean field approximation is applied as an extension to the isolated ladder Hamiltonian, containing the inter-ladder coupling;

$$\begin{aligned}\mathcal{H} =& J_r \sum_{i=1}^{L} \mathbf{S}_{i,1} \cdot \mathbf{S}_{i,2} + J_l \sum_{j=1,2} \sum_{i=1}^{L-1} \mathbf{S}_{i,j} \cdot \mathbf{S}_{i+1,j} \\ &+ \frac{n_c J' m^z}{4} \sum_{i,j} S^z_{i,j} + \frac{n_c J' m^z_a}{2} \sum_{i,j} (-1)^{l+k} S^x_{i,j}. \end{aligned} \tag{2.4}$$

This represents a coupled ladder where a magnetic field is applied along the z direction and order occurs in the xy-plane. The site dependent magnetisation has a uniform component m^z and a in-plane staggered component m^x. In the case of the $BPCBC_x$ series the rung connectivity (n_c) is 4. Results for BPCB are shown in section 2.2.2 and in figure 2.5.

Details on the spin Luttinger-liquid phase can be found in chapter 7. Similarly, details about the field polarised phase and the elementary excitations in this phase can be found in section 5.2.

2.2.1 Spin ladder compounds

The main material in this thesis is the metal-organic S = 1/2 antiferromagnetic spin ladder compound BPCB and the $BPCBC_x$ series. This material has exchange parameters which allow the system to be described by weakly coupled dimers in a ladder geometry. In section 2.2.2 previous work on BPCB is summarised. Other model systems also exist, which are in the opposite exchange parameter limit and as such the physics can be described by weakly coupled chains. One such material is $(C_7H_{10}N)_2CuBr_4$ or DIMPY [8].

DIMPY is a complimentary material to BPCB as both are S = 1/2 metal-organic antiferromagnetic spin ladder compounds. DIMPY has exchange parameters J_l = 1.42(6) meV and J_r = 0.82(2) meV [9] which are derived from the excitation spectra at zero field. Due to the dominant leg exchange determination of the exchange parameters could not be achieved by perturbation theory as discussed is section 5.2 [8, 10]. Instead comparisons with numerical simulations from DMRG were used to extract the exchange parameters. DIMPY is an important compound in the understanding of spin ladder physics as it is an ideal material in the opposite coupling limit to BPCB and BPCC. The results of study between these two classes of compounds completes the understanding of spin ladders and shows that the underlying physics is identical despite the large difference in exchange ratios.

This material exhibits the magnetic phases presented in the generic spin ladder phase diagram (figure 2.2). The critical point H_c occurs at 2.85 T [9], signalling the onset of the spin Luttinger-liquid phase. The saturation field H_s had been determined to be 28 T, with low magnetisation measurements experimentally accessible.

The excitations in the spin Luttinger-liquid phase have been measured up to 9 T, where the characteristic signatures of the Luttinger-liquid have been observed [11].

Magnetic ordering due to a finite inter-ladder coupling occurs at 300 mK [9], which corresponds to a mean field inter-ladder exchange of 6.3 μeV.

To contrast with the metal-organic compounds DIMPY and BPCDC$_x$, which are clean model systems, low dimensional exchange structure also play a role in copper oxide materials. Often called telephone compounds (La,Y,Sr,Ca)$_{14}$Cu$_{24}$O$_{41}$ show properties of spin chains, ladders and at certain range of hole doping exhibit high temperature superconductivity. These compounds exhibit spin chain and spin ladder behaviour as well as charge density wave states making them complex and intriguing systems. As these are metallic systems instead of the magnetic insulating metal-organic compounds, other exchange interactions are present. These include ring exchange as is present in La$_4$Sr$_{10}$Cu$_{24}$O$_{41}$ [12, 13]. With exchange interactions in the hundreds of Kelvin only the quantum disordered phase is experimentally accessible. This twinned with additional exchanges makes them non-ideal candidates for the study of spin ladder physics. An excellent review on (La,Y,Sr,Ca)$_{14}$Cu$_{24}$O$_{41}$ compounds, the affect of doping and the present experimental situation can be found in reference [14].

Since the resurgence in the popularity of spin ladder physics there have been many attempts to find new model materials, which has been largely unsuccessful. One such material which had been considered a spin ladder candidate was Copper Nitride, which is examined in depth in chapter 6. Through neutron scattering the determination of the Hamiltonian was possible and it was found to be an alternating Heisenberg antiferromagnetic chain [15]. Recent detailed work has shown that the compound also exhibits many common features with the spin ladder such as 3D ordering, and a Luttinger-liquid phase [16]. Another such compound is piperazinium hexachlorodicuprate (PHCC), a frustrated quasi-2D Heisenberg antiferromagnet which shares an near identical magnetisation curve to a spin ladder [17]. In this case it is the lack of square-root singularities at the quantum critical points which pointed to it's true spin geometry.

2.2.2 Overview of $(C_5H_{12}N)_2CuBr_4$

The antiferromagnetic S = 1/2 metal-organic spin ladder compound $(C_5H_{12}N)_2CuBr_4$, commonly known as $(Hpip)_2CuBr_4$ or BPCB is a model spin ladder in the strong coupling limit. This material will be the starting point for the work in this thesis. Previous work on this compound is summarised below, as much of the physics presented is relevant for the chlorine analogue and cases of partial substitution. From here on, the shorthand nomenclature BPCB will be used for the pure bromine compound.

BPCB was first synthesised by B. Patyal *et al.* in 1990 [18] and has been intensively studied in subsequent years. This includes studies by neutron and x-ray diffraction [18], inelastic neutron spectroscopy (INS) [19], heat capacity and magnetocaloric effect (MCE) [20], nuclear magnetic resonance (NMR) [21], electron spin resonance (ESR) [22, 23] and magnetostrictive [24] measurements to name a few.

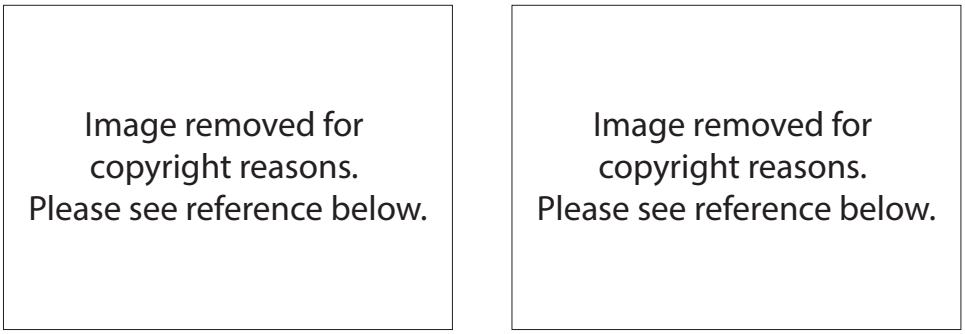

Figure 2.3: Magnetisation curves for BPCB. Left) Magnetisation curve for BPCB at various temperatures inset with the magnetisation differential [25]. Right) Magnetisation curve at 40 mK from NMR measurements and comparisons with an XXZ chain and DMRG calculations of a spin ladder [21]

Susceptibility and magnetisation measurements were initially performed by Watson *et al.* in reference [25]. The magnetisation measurements were performed at a base temperature of 0.7 K as shown in the left panel of figure 2.3. In the Watson paper a strong rung ladder was chosen as the appropriate model to describe the data, however a XXZ model could not be excluded due to the temperature which the measurements were performed. NMR was used in reference [21] to determine

the magnetisation at 40 mK as shown in the right panel of figure 2.3. From these measurements and comparisons with DMRG calculations it was unambiguously confirmed that the material was best described by a spin ladder model with exchange parameters J_r = 12.8 K, J_l = 3.3 K.

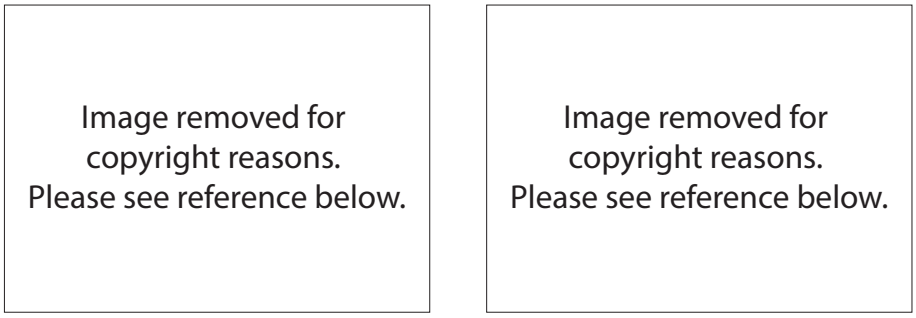

Figure 2.4: Zeeman splitting and the spinon continuum in BPCB. Left) Zeeman splitting in BPCB and the zero field dispersion for various reciprocal lattice vectors. Right) Low energy spinon continuum and associated numerical calculations using the extracted exchange parameters. Figures taken from reference [19]

In the work of Thielemann *et al.* inelastic neutron scattering measurements were performed on single crystals on BPCB [19]. The dispersion was measured in zero field and it was found that the exchange parameters were J_r = 12.8(1) K and J_l= 3:2(1) K. On application of magnetic field the triplet degeneracy lifts and a field dependent splitting occurs (figure 2.4).

On the closing of the spin gap the spin Luttinger-liquid phase is entered, where the low energy spectrum is the fractionalization of magnons into deconfined spinons. The low energy spectra for half magnetisation is shown in the right panel of figure 2.4 with results from a XXZ chain model.

Other exchange parameters such as the inter-ladder coupling J' are estimated to be J' = 20-100 mK [26, 21]. This has been established by observation of the Bose Einstein condensation of magnons at temperature below J'. The 3D exchange structure is shown in the left panel of figure 2.5. In the right panel is the boundary of the 3D XXZ phase as determined by neutron diffraction. The colour map above shows magnetocaloric effect data taken down to 100 mK. The 3D XXZ ordering is described by the mean field Hamiltonian given earlier (equation 2.4).

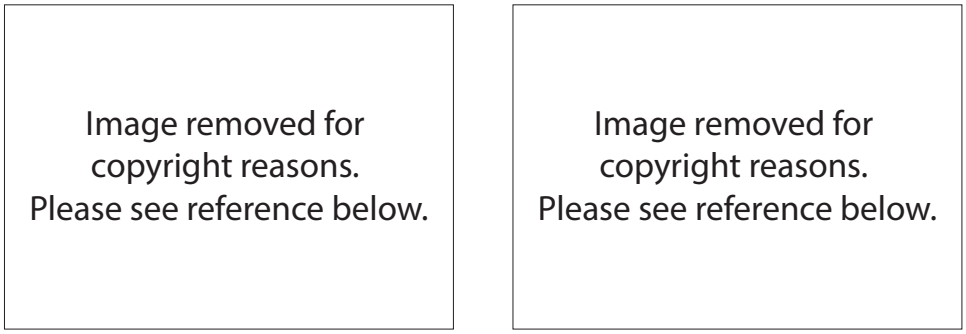

Figure 2.5: Magnetic order in the 3D XXZ phase of BPCB. Left) Exchange structure of BPCB with inter-ladder exchange J' shown in green. Right) Colour map of the MCE down to 100 mK and exchange boundary of the 3D XXZ phase from neutron diffraction experiments. Taken from reference [26]

Evidence of other interactions such as Dzyaloshinskii-Moriya (DM) and anisotropies have been suggested by ESR measurements in reference [22]. It was found that these additional exchanges are on the order of the inter-ladder exchange.

In section 2.2 the generic spin ladder phase diagram was introduced. For BPCB, the phase diagram has been experientially determined by Rüegg *et al.* [20] by thermodynamic measurements and is shown as a false colour C/T map in figure 2.6. The phase diagram shows exceptional agreement with the expected phase diagram of weakly coupled ladders, suggesting that the additional anisotropies do not have a measurable effect.

2.3 Scientific case

This work in this PhD will address the following;

The discovery of new spin ladder material with exotic properties.

There are few materials which exhibit spin structures which are an ideal representation of spin lattices. Typically in real materials other interactions are present which dilute or complicate one dimensional systems. Known model spin ladder compounds with experimentally accessible physics are scarce and with interactions which typically express characteristics of weakly coupled

Figure 2.6: Experimentally determined phase diagram for BPCB determined by specific heat measurements shown as a false colour C/T map. The gapped quantum disordered phase (QD) is shown below the first quantum critical point H_c (labelled as B_c). Around this point quantum criticality (QC) dominates before at higher fields the system crosses over to the Luttinger liquid (LL) phase. The boundary of which is denoted by white circles and extracted from MCE measurements. Black lines below H_c represent the closing of the spin gap. The second critical point at field H_c (labelled as B_c) represent the beginning of the field polarised (FP) phase. The blue dashed line shows the boundary of the anti-ferromagnetic phase at approximately 100 mK. Figure taken from reference [20].

chains or weakly interaction dimers. New model materials can bridge the gap between these two classes and explore the competition between the chain and dimer limits.

The effect of bond disorder on a model spin ladder system.

In the presence of bond disorder it has been theoretically predicted that new phases will be induced. The most discussed effect is the formation of a Bose-glass phases, a collection of locally fluctuating uncorrelated magnetic domains. This rare physics has not been conclusively observed in spin ladder systems, for which it's predicted to exist. Also questions on the elementary excitations and the dispersion of the systems exists and has little work published on the subject.

Excitations in the spin Luttinger-liquid phase and the effect of temperature.

The spin Luttinger-liquid phase of the spin ladder has been studied in a few materials. Inaccessible quantum critical points limit the study of this phase and the collective excitations present. The materials BPCB and BPCC have fully a accessible phase diagram and as such the spin dynamics in this phase can be fully measured at arbitrary magnetisations. Theoretical work on spin incoherence in this phase has been applied to spin ladders and unique features predicted, which have not been experimentally verified due to the lack of model materials.

Some of the questions stated above are addressed in the following papers;

- S. Ward, P. Bouillot, H. Ryll, K. Kiefer, K. Krämer, C. Rüegg, C. Kollath, and T. Giamarchi, J. Phys.: Condens. Matter **25**, 4004 (2013).
- H. Ryll, K. Kiefer, C. Rüegg, S. Ward, K. Krämer, D. Biner, P. Bouillot, E. Coira, T. Giamarchi, and C. Kollath, Phys. Rev. B **89**, 144416 (2014).

With a further 3 papers in preparation which cover results pertaining to the results presented in the following chapters. These include work on; the Hamiltonian of BPCC, covering the dispersion and exchange parameters to be presented in PRB.

Excitations and disorder effects in a random bond spin ladder material for PRL and a complete study of the spin Luttinger-liquid phase of an ideal ladder and spin incoherence on increased temperatures.

Chapter 3

Experimental Techniques

Contents

Many systems in a large variety of fields can be studied by neutron scattering. The systems of interest vary from the structural determination of solids, to the dynamics of liquids and the mechanical effects of stress to name a few. The unique properties of the neutron, a weakly interacting particle with a magnetic moment and a typical wavelength which is of the order inter-atomic spacing make it an invaluable tool for the study of condensed matter systems.

3.1 Neutron scattering

Neutrons for scattering experiments are produced by either nuclear fission or spallation. Institut Laue Langevin (ILL, Grenoble - Fr) provides the worlds highest flux of 10^{15} n/s, achieved by the fission of U^{235}. Spallation sources such as the the Spallation Neutron Source (SNS, Oak Ridge National Laboratory - USA) produce

neutrons by the thermal evaporation of neutrons from target nuclei by the application of intense proton beams. Pulses at the SNS produce 10^{17} n/s for a fraction of a millisecond. Spallation sources such as SINQ at the Paul Scherrer Institut (PSI, Villigen - CH) use much longer proton pulses, which create an effective constant neutron flux after moderation. In both cases the neutrons are initially highly energetic and cannot be used due to their small wavelength. Moderators of light materials such as Helium, Hydrogen and Methane reduce the neutrons energy by elastic collisions, giving a Boltzmann distribution of energies corresponding to the moderator temperature. Typically neutron energies are classified as hot (100-500 meV), thermal (5-100meV) and cold (0.1-10meV) [27]. These neutrons reach the experimental stations by supermirror guides, which reduce neutron loss.

3.1.0.1 Neutron scattering cross section

Neutron scattering theory has been derived and explained in many standard textbooks, including the works by Lovesey [28, 29], A. Furrer, J. Mesot and Th. Strässle [30] and G.L. Squires [27] and many more. The scattering theory presented follows the arguments presented in the latter.

To start, we consider a beam of monochromatic neutrons with wavevector $\mathbf{k_i}$ incident on a target, scattering to a final wavevector $\mathbf{k_f}$. The difference between $\mathbf{k_i}$ and $\mathbf{k_f}$ is the momentum transfer $\mathbf{Q}$. The wavevectors can also be converted to neutron energy as

$$\hbar\omega = \frac{\hbar}{2m_n}\left(\mathbf{k_i}^2 - \mathbf{k_f}^2\right). \tag{3.1}$$

The momentum $\mathbf{Q}$ can be represented as the sum of the wavevector $\mathbf{k}$ and the scattering vector $\mathbf{ø}$.

$$\mathbf{Q} = \mathbf{k} + \mathbf{ø}. \tag{3.2}$$

To describe the neutron scattering cross section we start at Fermi's golden rule,

$$W_{\Lambda\to\Lambda'} = \frac{2\pi}{\hbar}\rho\left(E'\right)|\langle\Lambda|V|\Lambda'\rangle|^2, \tag{3.3}$$

where $W_{\Lambda\to\Lambda'}$ is the probability to transition from state Λ to Λ' by perturbation V and $\rho\left(E'\right)$ is the density of states for the final energy. For neutron scattering, we

normalise the flux and sum over all available states.

$$\left(\frac{d^2\sigma}{d\Omega dE'}\right) = \frac{k_f}{k_i}\left(\frac{m_n}{2\pi\hbar^2}\right)\sum_{\lambda',\sigma'}\sum_{\lambda,\sigma} p(\lambda)\, p(\sigma)\, |\langle\Lambda'|V|\Lambda\rangle|^2 \delta\left(E_\lambda - E_{\lambda'} + \hbar\omega\right), \quad (3.4)$$

3.1.0.2 Nuclear scattering

We put in a Fermi pseudopotential $V_j(\mathbf{r})$ which corresponds to the potential the neutron experiences at a point. $\mathbf{r}$ and $\mathbf{R}_j$ are the position vectors of the neutron and the j^{th} nuclei respectively. Due to the nuclear interaction being short range, we can approximate the potential to a delta function.

$$V_j(\mathbf{r}) = \frac{2\pi\hbar^2}{m_n} b_j \delta\left(\mathbf{r} - \mathbf{R_j}\right), \quad (3.5)$$

where b_j is the nuclear scattering length of the isotope of a nuclei at position j and the neutron mass is given by m_n. Inserting equation 3.5 into 3.4 leads to the nuclear structure factor for nuclear scattering. This can be represented as a Fourier transform of time-dependent operators ($\mathbf{R_j}(t)$) where the delta function has been represented by an integral. Following the derivation in reference [27] gives,

$$\frac{d^2\sigma}{d\Omega dE'} = \frac{k_f}{k_i}\frac{m_n}{2\pi\hbar^2}\sum_{j,j'} b_j b_{j'} \int_{-\infty}^{\infty} \left\langle \exp\left\{-i\mathbf{Q}.\mathbf{R_{j'}}(0)\right\} \exp\left\{i\mathbf{Q}.\mathbf{R_j}(t)\right\}\right\rangle \exp\left(-i\omega t\right) dt. \quad (3.6)$$

Due to the large number of identical particles in a typical scattering system, it is easier to represent the scattering lengths b_j as the average values weighted by a frequency. If we assume that there is no correlation between the values of b, we can express the averages as

$$\overline{b_{j'} b_j} = \begin{cases} \left(\overline{b}\right)^2 & \text{for } j' \neq j \\ \left(\overline{b^2}\right) & \text{for } j' \equiv j. \end{cases} \quad (3.7)$$

This naturally splits equation 3.6 into two parts, which represent coherent and incoherent scattering.

$$\begin{aligned} \frac{d^2\sigma}{d\Omega dE'} &= \left(\frac{d^2\sigma}{d\Omega dE'}\right)_{coh} + \left(\frac{d^2\sigma}{d\Omega dE'}\right)_{inc} \\ &= \frac{k_f}{k_i}\frac{1}{4\pi}\left(\sigma_{coh} S\left(\mathbf{Q}, w\right) + \sigma_{inc} S_{inc}\left(\mathbf{Q}, w\right)\right), \end{aligned} \quad (3.8)$$

where

$$\sigma_{coh} = 4\pi \left(\overline{b}\right)^2 \ , \ \sigma_{inc} = 4\pi \left\{\overline{b^2} - \left(\overline{b}\right)^2\right\}. \tag{3.9}$$

The coherent and incoherent cross sections, $S(\mathbf{Q}, w)$ and $S_{inc}(\mathbf{Q}, w)$ are given by

$$\begin{aligned} S(\mathbf{Q}, w) =& \frac{1}{2\pi\hbar} \sum_{j,j'} \int_{-\infty}^{\infty} \left\langle \exp\left\{-i\mathbf{Q}.\mathbf{R_{j'}}(0)\right\} \exp\left\{i\mathbf{Q}.\mathbf{R_j}(t)\right\}\right\rangle \exp(-i\omega t)\, dt \\ S_{inc}(\mathbf{Q}, w) =& \frac{1}{2\pi\hbar} \sum_{j} \int_{-\infty}^{\infty} \left\langle \exp\left\{-i\mathbf{Q}.\mathbf{R_j}(0)\right\} \exp\left\{i\mathbf{Q}.\mathbf{R_j}(t)\right\}\right\rangle \exp(-i\omega t)\, dt. \end{aligned} \tag{3.10}$$

The coherent scattering cross section is closely related to the principle correlation function, which physically describes the correlations between the same nucleus at different times and the position of different nuclei at different times. This produces purely interference effects that lead to Bragg scattering and lattice excitations. The incoherent cross section is closely related to the self correlation function and purely provides information on the correlations of the same nucleus at different times. This physically describes the anisotropic background scattering and would be zero for a system without nuclear spin.

3.1.0.3 Magnetic scattering - Elastic

The neutron has a magnetic moment with spin $S = \frac{1}{2}$. This allows the neutron to scatter from unpaired electrons and magnetic atoms by its magnetic dipole moment. The unpaired electron in a system produces a local magnetic field from both its spin and angular momentum given by $\mathbf{B_i}$, with an interaction potential $V_i = \boldsymbol{\mu}_N \cdot \mathbf{B_i}$. Expanding this potential gives

$$V_i = \underbrace{-\gamma \frac{e\hbar}{2m_n}\boldsymbol{\sigma}}_{\boldsymbol{\mu}_N} \cdot \underbrace{-\frac{u_0}{4\pi}\left\{\mathrm{curl}\left(\frac{\mathbf{u_e} \times \widehat{\mathbf{R}}}{R^2}\right) - \frac{2u_B}{\hbar}\frac{\mathbf{p} \times \widehat{\mathbf{R}}}{R^2}\right\}}_{\mathbf{B_i}} \tag{3.11}$$

Here the magnetic dipole moment of the neutron ($\boldsymbol{\mu}_N$) consists of the electric charge e, the mass of the neutron m_n and the Pauli spin operator for the neutron $\boldsymbol{\sigma}$. γ is a positive constant of 1.913. The derivation of $\mathbf{B_i}$ is more complex and described in Squires (reference [27]). Following the long derivation described in Squires and other textbooks we arrive at the magnetic scattering cross section for a magnetically ordered single domain crystal;

$$\frac{d^2\sigma}{d\Omega dE'} = (\gamma r_0)^2 \left\{\tfrac{1}{2} gF(\mathbf{Q})\right\}^2 \exp(-2W) \sum_{\alpha,\beta} \left(\delta_{\alpha,\beta} - \widehat{Q}_\alpha \widehat{Q}_\beta\right) S^{\alpha,\beta}(\mathbf{Q},\omega). \quad (3.12)$$

$F(\mathbf{Q})$ is the magnetic form factor and W the Debye-Waller factor. The Debye-Waller factor represents the attenuation factor due to thermal motion. The dynamical spin-spin correlation function $S^{\alpha,\beta}(\mathbf{Q},\omega)$ is the Fourier transform in time and real space of the spin-spin correlation function.

3.1.0.4 Magnetic scattering - Inelastic

The dynamical spin-spin correlation function introduced in equation 3.12 in the most general form is

$$S^{\alpha,\beta}(\mathbf{Q},\omega) = \sum_{i,j} \exp(i\,\mathbf{Q}\cdot(\mathbf{R_i} - \mathbf{R_j})) \sum_{\Lambda,\Lambda'} \left\langle \Lambda|\widehat{S}_i^\alpha|\Lambda'\right\rangle \left\langle \Lambda|\widehat{S}_j^\beta|\Lambda'\right\rangle \delta(E_\Lambda - E_{\Lambda'} + \hbar\omega), \quad (3.13)$$

where only spin scattering is considered. The orbital contributions to the scattering magnetic-moment have been neglected. Two spin operators $\widehat{S}_i^\alpha$ and $\widehat{S}_j^\beta$ are introduced which correspond to α-component of spin on the magnetic ion i and the β-component of spin on the magnetic ion j. The δ function selects an energy transfer from state Λ to Λ'.

3.1.1 The triple-axis spectrometer

The triple-axis spectrometer or TAS was developed by Bertram Brockhouse in 1955-56 whilst working at the Chalk River Laboratories (Canada) and is arguably the most important piece of scientific equipment available to scientists who use neutrons to study condensed matter. The TAS allows for a direct measurement of the differential cross section, with freedom in both momentum and energy transfer. The experimentally obtained differential cross sections can easily be compared to theories, allowing for accurate determination of, for example spin dynamics. The flexibility of the TAS also makes it an excellent diffraction instrument and techniques such as neutron spin echo extend the energy resolution to unprecedented levels.

A schematic drawing of a TAS (IN14 - ILL) is shown in figure 3.1. A polychromatic beam of neutrons is guided from a source to the monochromator whereby a monochromatic beam is diffracted. The monochromator consists of a mosaic of crystals, typically Pyrolytic Graphite (PG), Silicon, or Copper, which have been co-aligned. Using Bragg's law $\left(n\lambda = 2d\sin\left(\frac{1}{2}\theta\right)\right)$, the angle of the monochromators rotation θ_{mono} selects the desired wavelength. This angle is typically called A1. The diffracted beam passes through shielding which rotates at an angle of twice θ_{mono} and is called A2. At this point the monochromatic beam can be horizontally/vertically collimated to reduce beam divergence. Due to n in Bragg's law unintended neutron energies are also transmitted. These energies can be filtered out with an efficient neutron filter, such as Beryllium or Graphite. The filter has a large neutron capture cross section, which is dependent on the incoming neutron energy. The efficiency of the filter depends on the neutron energy and temperature, due to the Debye-Waller factor.

The outgoing beam from the monochromator is incident on the sample with wavevector k_i and is scattered by the sample. For elastic scattering, the final wavevector k_f is equal to k_i and selected by rotating the angle A4 ($2\theta_{sample}$). To bring the scattering plane into the scattering condition the sample is rotated (A3).For the inelastic case where $k_i \neq k_f$ the desired energy transfer is selected by rotation of the analyser and detector. Similarly to the monochromator, the analyser selects the desired final energy by Bragg's law and rotating θ_{ana} by an angle A5. The detector position A6 is determined to be twice A5. These angles can be calculated from first principles or from an extension to the UB matrix formalism proposed by Busing and Levy in 1967 [31] and by Lumsden in 2005 [32] With the ability to select arbitrary points in $\mathbf{Q}$ and ω space, two classes of typical scan can be performed, one which consists of a constant $\mathbf{Q}$ and varying ω which is called an energy scan and the other where ω is kept constant and $\mathbf{Q}$ changes. The latter is called a constant wavevector scan.

Another important aspect of the triple-axis spectrometer is the neutron beam monitor. The monitor is a weak detector that is placed in the incoming beam. This monitor gives a time independent value to the number of neutrons that are incident on the sample. The neutron flux can vary due to the incoming energy selected

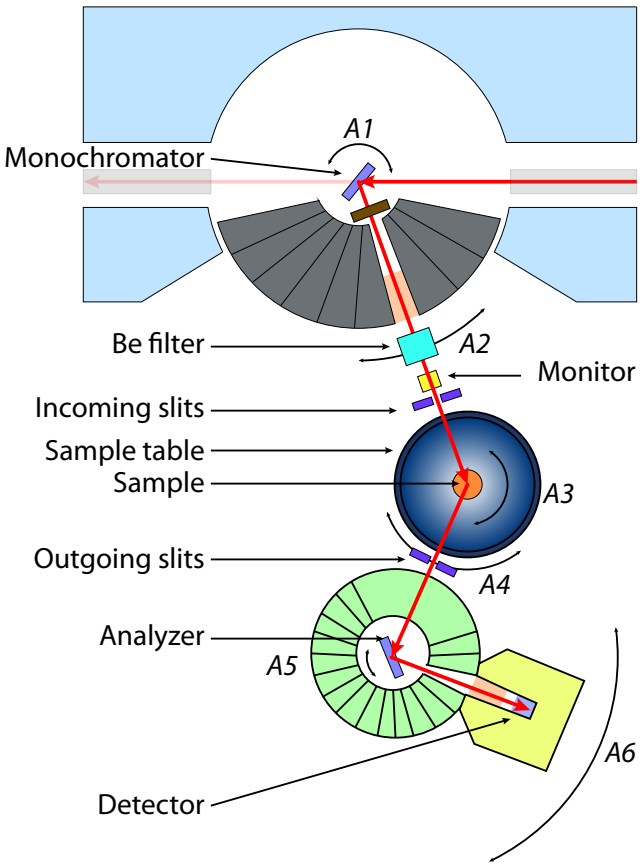

Figure 3.1: A schematic showing the triple-axis spectrometer IN14 for the w configuration. Angle definitions are explained in the text. This configuration has been used for all experiments in this thesis. Adapted from reference [33]

(Boltzmann distribution of beam energies) and beam stability. Most measurements are performed by normalising counting time to a monitor value as this removes variations in incoming neutron flux.

3.1.1.1 Resolution effects

One consideration when using a TAS is the effects of experimental resolution. The neutron distribution in both the incoming and outgoing beam is significantly effected by scattering from the monochromator, analyser, divergence and distance travelled. When focusing optics are also used the effects can become increasingly more pronounced and can lead to relaxation of resolution in $\mathbf{Q}$ and/or ω. The resolution

ellipsoids can be simulated by various techniques, including the Cooper-Nathans [34], Popovici [35] and ray-tracing [36]. The latter being a modern development spurred by exponential increases in computational power. In this work the Popovici will be used to calculate the resolution due to its accuracy and favourable performance scaling.

The resolution of the IN14 triple axis spectrometer (ILL, Grenoble) is shown for various ω points at fixed $\mathbf{Q}$ in figure 3.2. The ellipses in this figure correspond to the coverage of 3 sigma or 99.73% of all neutrons. In this example the sample was in the Q_h, Q_l plane and the resolution projections are shown in figure 3.2 *a*. Panels *b* and *c* show the $Q_{h,l}$ Vs. energy resolution ellipsoid.

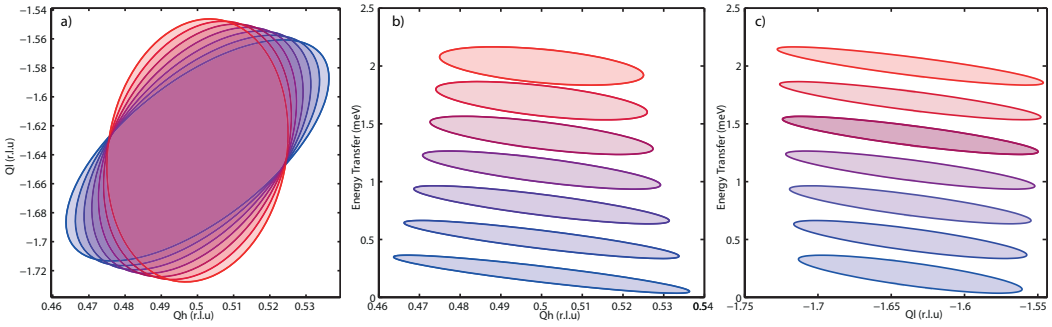

Figure 3.2: Resolution ellipsoid projected onto various scattering and energy transfer planes. Blue shading corresponds to low energy transfers and red high energy transfers. Left) Resolution ellipsoid in the Q1-Q2 plane for various energy transfers. Middle) Resolution ellipsoid in the Q1-Energy plane. Right) Resolution in the Q2-Energy plane.

The consequences of resolution on the measurement of a dispersion is shown in figure 3.3. Figure 3.3a2 shows a dispersion with a finite energy width of 0.0005 meV, corresponding to the near ideal case of a dispersion represented by a delta function. When the resolution is convolved for a typical cold neutron spectrometer, resolution effects are clearly visible (figure 3.3a1). A profound broadened line width appears and resolution focusing and defocusing is visible. Cuts of this dispersion represent energy scans and are shown in figure 3.3b and shows these effects in more detail.

Resolution is highly dependent on the neutrons energy and as such thermal spectrometers have worse resolution than cold spectrometers. Time-of-flight spectrome-

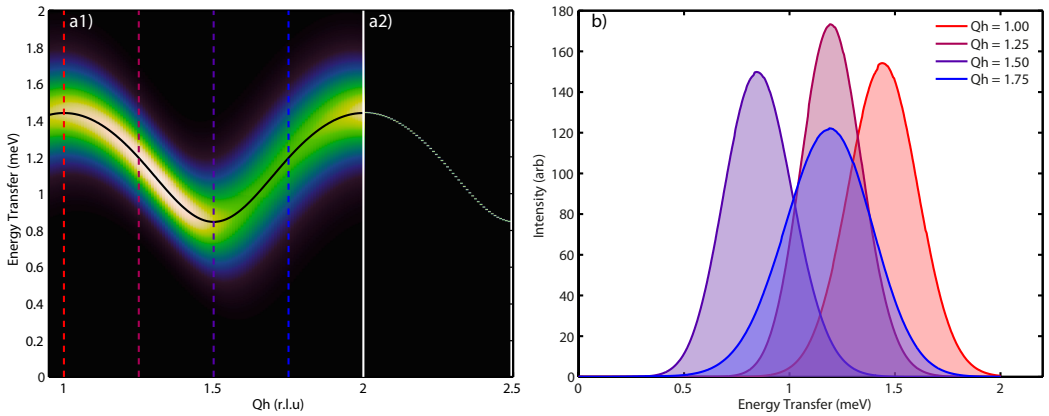

Figure 3.3: Resolution effects on a dispersion. Left) Dispersion which has been convolved with an example resolution from the triple-axis-spectrometer IN14. Focusing and defocusing effects are visible at $Q_h = 0.75$ and 0.25. Right) Energy transfers for various momentum points. Shaded areas correspond to dashed lines of the same color on the left panel.

ters have the advantage that resolution effects are less pronounced than the triple-axis spectrometer as the resolution ellipsoid is not convolved with the monochromator or analyser.

3.1.2 Time-of-flight spectrometers

Time-of-flight (ToF) spectrometers operate at pulsed neutron sources, the spectrometer being at a set distance from the moderator. The energy spectrum of the neutrons from the moderator follow a Boltzmann distribution. A set of disk choppers are placed at a set distance from the moderator. By timing the choppers frequency to the spallation event it is possible to select a near monochromatic neutron slice. This sub-distribution can be shaped and refined by additional choppers before reaching the sample. This allows for a known incoming energy and as such wavevector. One distinguishing feature of ToF spectrometers is that the stationary detectors cover a large solid angle. Position sensitive detectors and accurate event timing are used to recreate the precise momentum and energy transfer of the neutron.

The time-of-flight instrument Low Energy Transfer spectrometer (LET - ISIS)

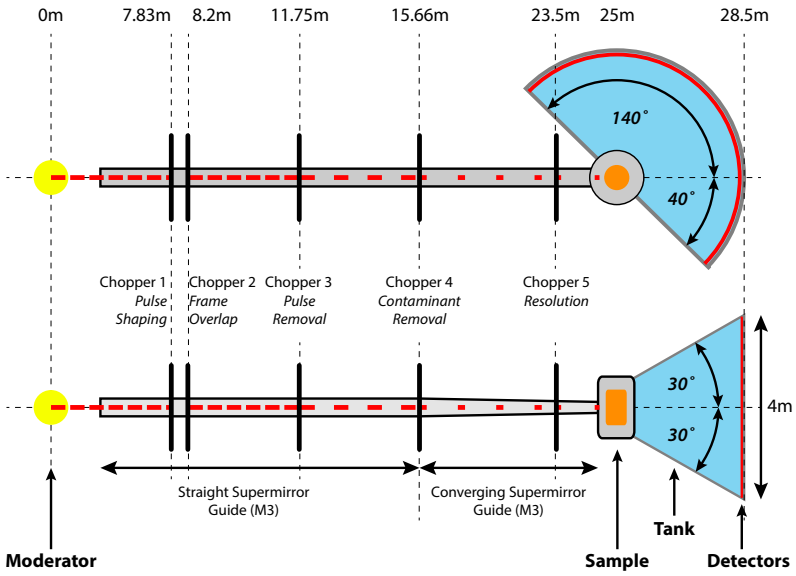

Figure 3.4: Schematic of the TOF spectrometer LET. Chopper functions and are described in the text. Adapted from reference [37]

is shown in figure 3.4 and is an instrument with 4 m detector tubes and π radians of detector coverage (when completed). It is specifically designed to look at low energy transfers and have exceptional resolution. Five sets of choppers select the appropriate energy, shape and remove contaminants from the beam. By modifying the chopper phases it is possible to obtain multiple incoming energies at the same time, and differentiate between them. In figure 3.5 a primary energy of 2.5 meV has been selected with energies 0.83 and 36.2 meV also being collected.

With the energy and momentum of the neutrons established the user obtains a 4-D data set of momentum and energy transfer. This can be manipulated through intricate software to take slices of energy and reciprocal space [38].

3.1.3 Sample environment

Temperature, magnetic field and pressure are crucial tuning parameters that allow us to access areas of the experimental phase diagram, each allowing for an addition degree of freedom. In this thesis high magnetic field and low temperatures will be employed to access the prototypical spin ladder phase diagram shown in figure 2.6.

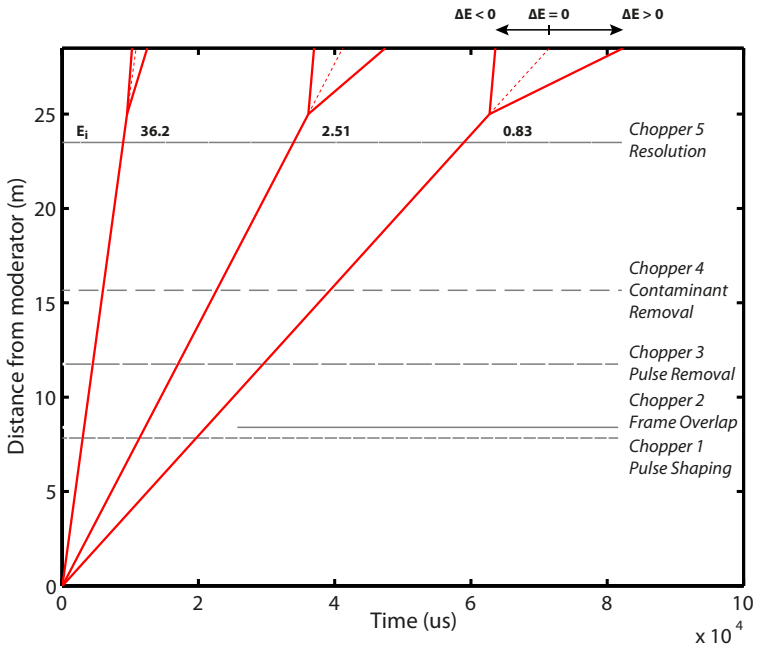

Figure 3.5: Schematic showing the opening of choppers for a primary incident energy of $E_i = 2.5$ on the ToF spectrometer LET. Chopper frequencies have been selected so that secondary incident energies of 36.2 and 0.83 meV are aquired at the same time (Frame rate multiplication). Red lines correspond to the speed of an incident energy. After the sample this splits into a time window corresponding to the neutrons energy transfer.

Refrigeration techniques

For measurements on condensed matters systems typical measurements are performed by the use of a Helium cryostat. Helium has a boiling point of 4.2 K, which can be reduced to approximately 1.8 K by pumping on the liquid ^{4}He. By substituting ^{4}He with liquid ^{3}He temperatures can be reduced to 300 mK. For BPCB lower temperatures are needed as thermal fluctuations hinder the investigation of quantum fluctuations. To obtain temperatures of 50 mK mixtures of $^{3/4}$He are needed.

Dilution refrigerators exploit the thermodynamics of $^{3/4}$He phases. ^{3}He has two phases, a dilute and concentrate phase which have different enthalpies below 0.9 K[39, 40]. Figure 3.6 shows the structure of a dilution refrigerator and how these phases are used to cool a sample.

The concentrated phase and the dilute phase of ^{3}He form a phase boundary in a part of the refrigerator called the mixing chamber. In the still the dilute phase is pumped and effectively only removes ^{3}He atoms due to their higher vapour pressure and kinetic energy [40]. This creates an imbalance in the $^{3/4}$He concentration, so ^{3}He atoms diffuse across the phase boundary (in the mixing chamber) causing cooling. The pumped ^{3}He is cooled, re-condensed and fed back into the mixing chamber. This process is constantly repeated to achieve temperatures of 20 mK. For neutron scattering experiments however, beam heating occurs and limits the lowest temperature to approximately 25 mK.

Cryomagnets

For this thesis there is an extensive use of high field cryomagnets. The magnets used for neutron scattering have particular properties due to the need for windows for the incoming and scattered beam.

The magnetic field is typically perpendicular to the neutron beam and is created by a split pair of superconducting coils either side of the beam. Typically the coils are made from NbTi/Nb_3Sn cables which have been cooled to liquid helium temperatures. The upper operating field for these magnets is $\approx$ 13 T, limited by the critical superconducting field. Similarly to the techniques noted above, the helium bath can be pumped through the helium lambda transition increasing the upper field to $\approx$ 15 T.

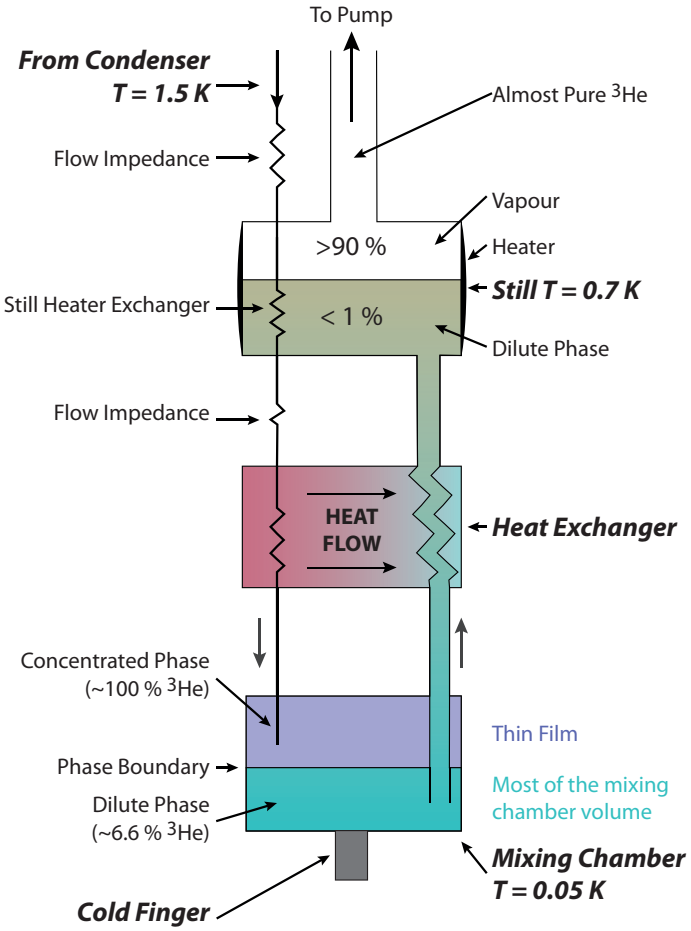

Figure 3.6: Schematic of a dilution insert showing the phases and $^{3/4}$He ratios present. The cooling method is describen in the text. Samples are attached onto the cold finger at the bottom of the figure.

Magnets with an upper field of 15 T exist in most neutron scattering facilities, though higher fields are limited by the superconducting cables and the forces they generate [41]. The 15 T split pair cryomagnet by *Oxford Instruments* will be used heavily in this thesis as the operating fields encompass the entire phase diagram of BPCB. This magnet can be used in collaboration with dilution equipment described above, allowing access to the complete phase diagram of BPCB and the BPCBC$_x$ series.

For small angle neutron scattering, a side loading 17 T magnet has been developed [42] which will hopefully lead to higher magnetic fields in other magnets. In a

laboratory setting fields of 22 T are possible and in dedicated high field laboratories pulsed fields can reach upto 300 T.

3.2 Magnetic measurements

In this thesis many magnetic measurement techniques will be used to analyse the magnetic properties of the $BPCBC_x$ series. This is a brief overview of the techniques used, technical details and the limits of the measurement techniques. These are summarised in the table below

Technique	AC	VSM	VCM	SQUID	Torque	Force
mK temperatures	+	-	+	+	+	+
High magnetic fields	+	+	+	-	+	+
In situ calibration	-	-	-	-	+	+
Angular dependence	-	+	-	-	+	+
Typical sensitivity (Am^2)	10^{-7}	10^{-10}	10^{-7}	10^{-11}	10^{-11}	10^{-9}

Table 3.1: Advantages and disadvantages of different magnetic measurement techniques. AC = Alternating current gradient, VSM = Vibrating sample magnetometer, VCM = Vibrating coil magnetometer, SQUID = Superconducting interference device (see section 3.2.1) and Force and torque magnetometer (see section 3.2.2). Adapted from [43]

3.2.1 Magnetic properties measurement systems

The Magnetic Properties Measurement System (MPMS by Quantum Designs) is a versatile piece of measurement apparatus for studying magnetic properties of materials. It has the ability to measure magnetisation and susceptibility of samples. The MPMS at the London Centre for Nanotechnology (LCN) operates between 0-7 T and 1.8-350 K. The MPMS has a high measurement accuracy as it uses a SQUID magnetometer to measure the changes in magnetic environment $\Delta M = 2 \cdot 10^{-8}$ emu. The operation of SQUID magnetometers is well understood, so only a brief summary of the most important points are given below.

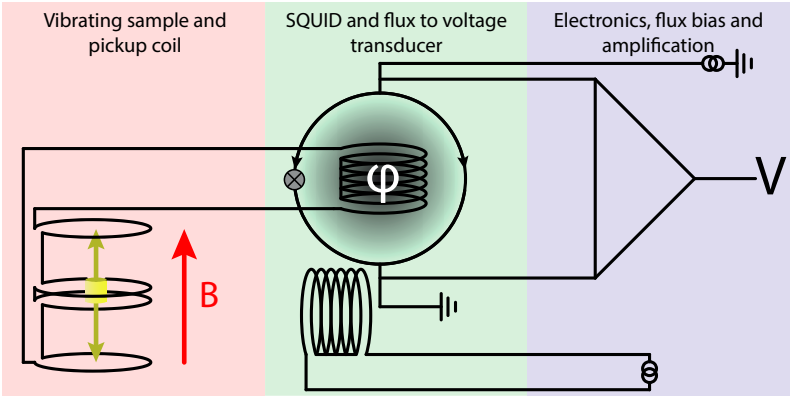

Figure 3.7: A schematic representation of the Quantum Design MPMS which has been adapted from user manual.

The SQUID or superconducting quantum interference device can come in two possible configurations, DC and RF-SQUID's. The MPMS uses a RF-SQUID the setup of which is shown in figure 3.7. The red section represents the sample and pickup stage. The sample undergoes reciprocating sample oscillation (RSO) inside a pickup coil, typically at 20-30 Hz. The movement of the magnetic sample induces a current in the pickup coil which is then transferred to the signal to flux converter. The green section shows how the signal to flux converter influences the flux in the SQUID, causing a change in the SQUID's internal flux state. By tuning reference oscillating voltages in the blue section to that of the RSO it is possible to determine when the flux state has changed by half a flux quantum ($\Phi_0/2$). At this stage signal amplification occurs and is converted into usable units.

3.2.2 Cantilever/torque magnetometry

One method of measuring the magnetic properties of a material is by cantilever magnetometry. The cantilever is formed by a silicon wafer with the lower surface coated in gold slightly above a sapphire substrate with gold contacts [44]. This forms a capacitor, which by careful calibration can achieve a resolution of 10^{-7} A/m^2. By rotating the cantilever in the magnetic field the torque the sample exerts on the plate can also be measured. The advantage of these measurements is that they can take place at dilution temperatures ($\approx$ 50 mK) and high magnetic fields.

The cantilever used for data collection in this thesis was made by our collaborator

H. Ryll (Helmholtz Zentrum Berlin - DE) as part of his PhD thesis. A full description of the calibration, measurements techniques and design can be found in reference [43].

3.3 Thermodynamic measurements

Thermodynamic measurements presented in this thesis are a result of a long standing a fruitful collaboration with the Laboratory for Magnetic Measurements (LaMM) at the Helmholtz Zentrum Berlin. Data was collected over a period of 1 year by H. Ryll as a part of his thesis [43].

3.3.1 Specific heat and magnetocaloric effect

Specific heat measurements have been taken using microcalorimeter consisting of a sapphire plate kept in thermal isolation. A high precision resistance heater and thermometer are used to supply a known quantity of heat to a sample and measure the relaxation by the adiabatic and quasi-adiabatic relaxation techniques. The magnetocaloric effect can also be measured by the same apparatus by sweeping the magnetic field and measuring the resulting change in temperature. More information on the MCE and measurement techniques performed at HZB can be found in reference [45] and the thesis by H. Ryll [43].

3.3.1.1 Maxwell equations

The magnetocaloric effect (Θ) is defined as;

$$\Theta = \left.\frac{dT}{dB}\right|_S \tag{3.14}$$

where measurements are performed in adiabatic conditions, meaning at constant entropy S. If the heat capacity (c_m) is known then;

$$\Theta(B) = \frac{1}{c_m(B)}\frac{dQ}{dB}. \tag{3.15}$$

This quantity is interesting as through a Maxwell equation we can obtain;

$$\frac{dQ/dB}{T} = -\frac{\partial S}{\partial B} = -\left.\frac{\partial M}{\partial T}\right|_B. \tag{3.16}$$

From this relation it is possible to extract the magnetisation and the entropy . This has been performed in reference [46, 47] and is shown in section 4.3 for BPCC.

Chapter 4

The $(C_5H_{12}N)_2CuBr_{4(1-x)}Cl_{4x}$ compound series

Contents

This section details the physical and bulk magnetic properties of the $(C_5H_{12}N)_2CuBr_{4(1-x)}Cl_{4x}$ series. Included is a review of the chemistry involved in sample synthesis and the techniques needed to obtain high quality single crystals. Crystallographic refinements from neutron powder diffraction provide detailed insights into the chemical substitution and changes in crystal structure. Magnetic susceptibility measurements allow for the extraction of x depended exchange couplings.

4.1 $(C_5H_{12}N)_2CuBr_{4(1-x)}Cl_{4x}$

The two-legged $S = 1/2$ spin ladder material $(C_5H_{12}N)_2CuBr_4$, otherwise called $(Hpip)_2CuBr_4$ or BPCB is a highly studied spin ladder in the strong coupling limit

($J_l/J_r << 1$). This compound was originally synthesised by Patyal *et al.* in 1990 [18], the lattice parameters and an estimate of the magnetic exchange parameters was presented. The compounds of the $(C_5H_{12}N)_2CuBr_{4(1-x)}Cl_{4x}$ or $BPCBC_x$ family were first reported by Tajiri *et al.* in 2004 [48]. The samples analysed in this series ($x = 0, 0.5, 1$) belong to the monoclinic spacegroup $P21_c$ and were synthesised by the method described in Patyal's paper. The lattice parameters for these compounds and their references are summarised in table 4.1. The structure of BPCB is shown in figure 4.1.

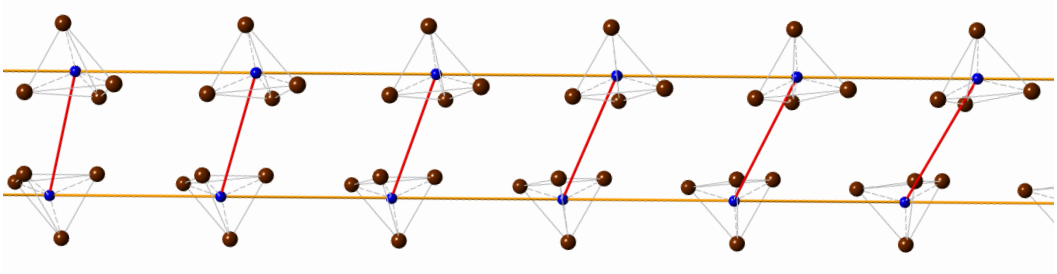

Figure 4.1: The crystal structure of $(C_5H_{12}N)_2CuBr_4$ in the ac-plane from refinements of Neutron powder diffraction data (see appendix A). The S = 1/2 magnetic moments reside on the Cu^{2+} ions shown in blue surrounded by four Br atoms. Antiferromagnetic rung exchanges shown in red form a spin dimer. Leg exchanges in orange couple these dimers to form a ladder structure. The organic molecule $C_5H_{12}N$ has been removed for clarity.

For all materials in this series a Cu^{2+} atom is surrounded by a cage of 4 halogens, creating a distorted copper-halide tetrahedron with valence 2-. Co-crystallisation with the piperidinium cations forms the metal organic molecule. Application of the symmetry elements of the $P21_c$ spacegroup replicate this structure within the unit cell. A magnetic dimer is created in the unit cell where the p shells of the halogens in the 2 tetrahedra overlap and is mediated by two copper halide bridges. These pathways combine to form the rung exchange J_r. Replicating this crystal structure allows for the dimers to be connected in a double chain fashion along the a axis. These two chains are inversion symmetric and form the leg exchange J_l. Between these ladder like exchange structures is the organic piperidinium, which stops the overlap of halogen electron shells. As such residual inter-ladder exchanges

x	**a** (Å)	**b** (Å)	**c** (Å)	$\beta(^\circ)$	$\mathbf{g_{avg}}$	**Reference**
0.0	8.487(2)	17.225(3)	12.380(2)	99.29(2)	2.13	[18, 49]
0.5	8.396	17.148	12.321	99.54	2.106	[48]
1.0	8.224	16.923	12.163	100.39	2.094	[48]

Table 4.1: Lattice parameters and average g-factor for BPCB, BPCBC and BPCC. In all cases the crystallographic spacegroup was determined to be $P21_c$ and the lattice parameters determined from room temperature x-ray diffraction performed on powder samples. In the case of BPCB the average g-factor was determined by EPR measurements and for BPCBC and BPCC ESR measurements were used. Magnetic exchanges were also determined for the above values of x and are summarised in section 4.2.1

are minimal.

The effect of the metal-halogen ligand on exchange strength can be considered in terms of the ionic character, determined by Pauling electronegativity. Copper has an electronegativity of 1.9 and Bromine 2.96. This gives the ligand a 22% ionic character, whilst Chlorine with a Pauling electronegativity of 3.16 and has 25% ionic character. The ionic character of the ligand partly determines of the magnitude of the superexchange pathway. Another crucial aspect is the halogens overlapping p orbitals, the extent of which can be considered from the point of free ionic radii. For Br^- the ionic radii is 1.96 Å and for Cl^- it is 1.81 Å [50], the reduction creating reduced overlap and reduced superexchange strength[a].

4.1.1 Sample Synthesis

High quality single crystals and powders of the pure starting compounds and $BPCBC_x$ have been produced in the department of chemistry and biochemistry, University of Berne (CH) by the group of Dr K. Krämer. Sample synthesis is performed along the lines of the method described by the original work of Patyal *et al.* [18] with slight modifications to increase crystallisation quality. For BPCB samples are formed from the evaporation of piperidinium bromide and copper bromide in an

[a] Assuming constant bond distance as taken from the case of BPCB.

ethanol solution.

$$2\,(C_5H_{10}NH_2Br) + CuBr_2 \xrightarrow{\text{Ethanol}} (C_5H_{12}N)_2CuBr_4 \qquad (C\,4.1)$$

For BPCC the starting materials have Br substituted for Cl, which are readily available and the crystal growth techniques are identical. To create pure samples 2 mole of copper bromide and one mole of piperidinium bromide are mixed with an over abundance of ethanol and a small amount of acid. For powder samples the evaporation of ethanol creates a supersaturated solution which readily forms small crystals in a few days. For single crystals the evaporation takes place in a nitrogen atmosphere and can take months for samples of 50-400 mg to form. Traditionally this takes place at room temperature, which can lead to a seasonal dependence in crystal quality. The effects of ambient temperature are not fully understood, but increasing the temperature to $\approx 25°$ produces the highest quality crystals. On extraction from the ethanol solution the samples are dried in a vacuum to remove solution from voids.

For samples where $x \neq 0$, 1, first powders are made by the method above and stoichiometric masses are used for the required Br/Cl ratio. These are dissolved in ethanol, mixed and re-crystallised to form $BPCBC_x$ samples.

$$(1-\mathrm{x})\cdot(C_5H_{12}N)_2CuBr_4 + \mathrm{x}\cdot(C_5H_{12}N)_2CuCl_4 \xrightarrow{\text{Ethanol}} (C_5H_{12}N)_2CuBr_{4(1-\mathrm{x})}Cl_{4\mathrm{x}} \qquad (C\,4.2)$$

It is assumed that the structure is fully separated into starting materials and there is no preference for crystallisation with like species. When crystallisation occurs $BPCBC_x$ is the primary product, however $(C_5H_{12}N)CuBr_3$ is also produced. This is either due to Cu(I) impurities in the starting material or excess heat, which leads to reduction in copper state, from Cu^{2+} to Cu^{1+} [51].

When growing $BPCBC_x$ stoichiometric quantities of starting material for a desired x are used, however the final sample can have a different value of x. To aid the crystal growth the solvent has to be slightly acidic, through application of HCl or HBr. In pure compounds this is irrelevant, however in substituted samples x will be affected. Also during the evaporation procedure there might be a preference for the evaporation of one halogen over the other leading to additional uncertainty. The precise determination of x is often overlooked in substituted halogen compounds

as it is difficult to measure. To determine x energy dispersive X-ray spectroscopic (EDX) analysis was used. In EDX a beam of high energy X-rays is focused onto a sample whereby an electron is emitted. The X-ray emitted when a shell electron fills this void is analysed by an energy dispersive detector. Example spectra are shown in figure 4.2.

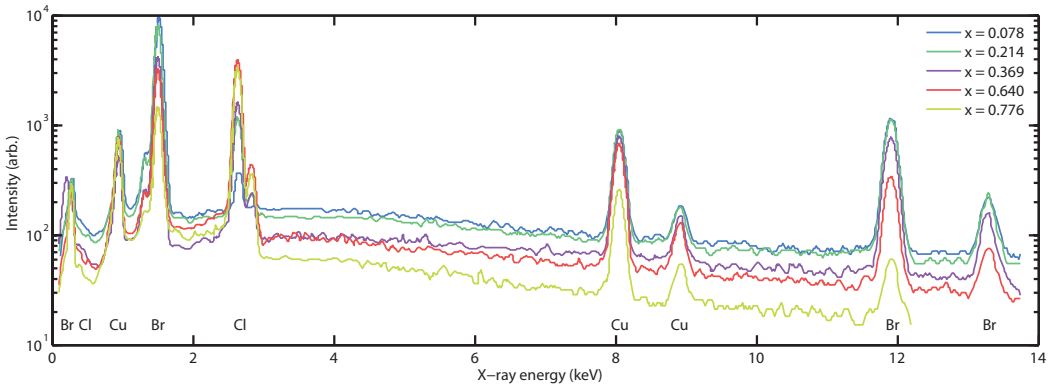

Figure 4.2: EDX spectra for various $BPCBC_x$ concentrations. The value for x given is derived from the spectra as described in the text.

The integrated intensity of each atoms excitation spectra with the relevant corrections is used to determine x by use of CsBr and CsCl reference samples. The values of x for these substitutions are shown in the figure. It is worth noting however that this method does have disadvantages; The EDX suite used is a black box and as such independent analysis can not be performed and assumes an optimum setup. Ideally samples undergoing EDX should be set in plastic with a cleaved surface. In the case of $BPCBC_x$ the samples cannot be either set in plastic or cleaved, which reduces the techniques accuracy. This has not been accounted for.

A selection of powder samples are shown in figure 4.3. I was lucky to spend a few weeks in the laboratory of K Krämer and was introduced to the sample synthesis process and made the samples shown in figure 4.3.

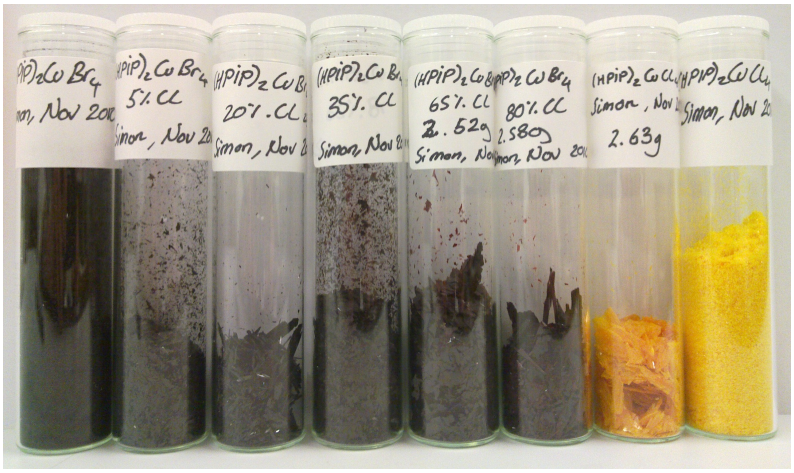

Figure 4.3: Powder samples of $BPCBC_x$ synthesised at University of Bern for various values of x. From left to right is nominal $x = 0$, 0.05, 0.2, 0.35, 0.65, 0.8, 1 (single crystal), 1 (powder). Pure $x = 0$ has a dark red colour which slowly becomes lighter, to yellow when reaching $x = 1$. Small quantities of Br ($\approx 1\%$) strongly effect the absorption spectrum.

4.1.2 Structure and bond disorder

Neutron powder diffraction experiments were performed on fully duterated powder samples of $BPCBC_x$ for nominal values of $x = 0$, 0.1, 0.5, 0.9 and 1 on the powder diffractometer HRPT (Villigen, PSI). Sample masses of approximately 2 g were measured at room (300 K) and base temperature (1.8 K) and a full diffraction pattern obtained. The diffraction patterns are sharp, distinct and can be refined. The crystallographic suite FullProf with the Rietveld refinement method was used [52]. The starting point for refinement is the well-known pure BPCB structure. It was found that a small percentage ($\approx 0.1\%$) of hydrogen was needed on the deuterium site for realistic Br/Cl ratios. In all cases the best spacegroup was that of the pure compounds, $P21_c$. Other space groups of reduced symmetry were also considered without an improvement in R-factor. No magnetic ordering of the BPCBCx compounds was observed. An example diffraction pattern and refinement is shown in figure 4.4.

The refined lattice parameters for the $BPBCB_x$ series are shown in figure 4.5. For the known case of BPCB there is agreement with lattice parameters reported

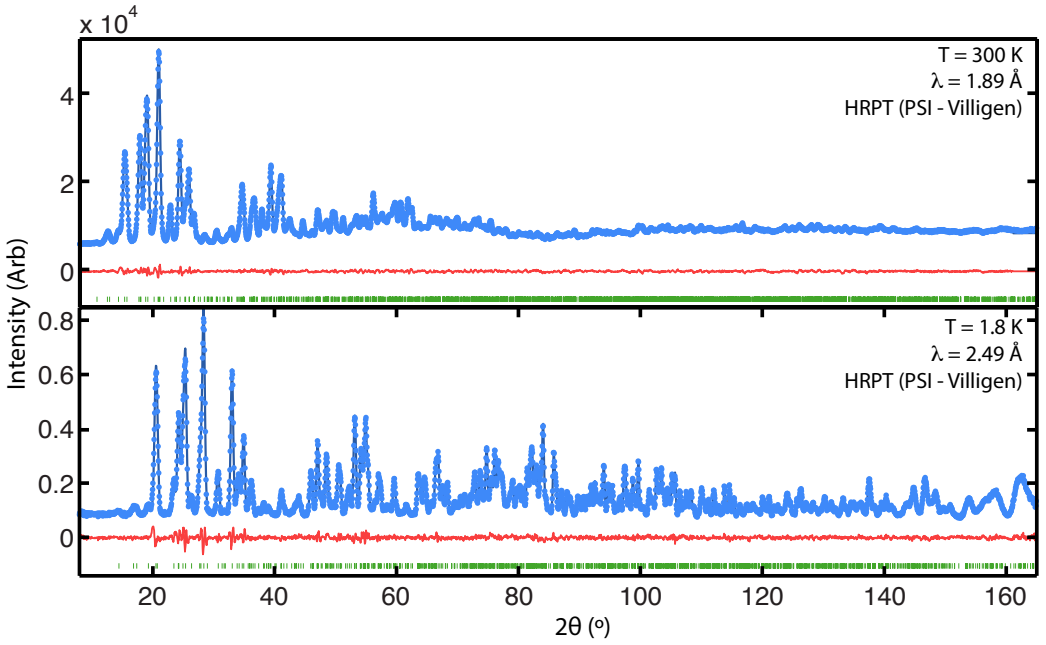

Figure 4.4: Neutron powder diffraction pattern of deuterated BPCB at 300 (Top) and 1.8 K (Bottom). Data-points are shown as light blue filled circles and refinement by the Rietveld method as described in the text is shown as a dark blue line. Below in green are the HKL reflections for the incident wavelength and the difference is shown in red.

previously and summarised in table 4.1. When plotted, lattice parameters show a clear linear relation with x as shown in the sub-figure of 4.5. The linear change of lattice parameters with alloying is common and is phenomenologically describes as Vegard's Law [53]. Whilst $BPBCB_x$ is not a metallic alloy, this model seems to describe the data.

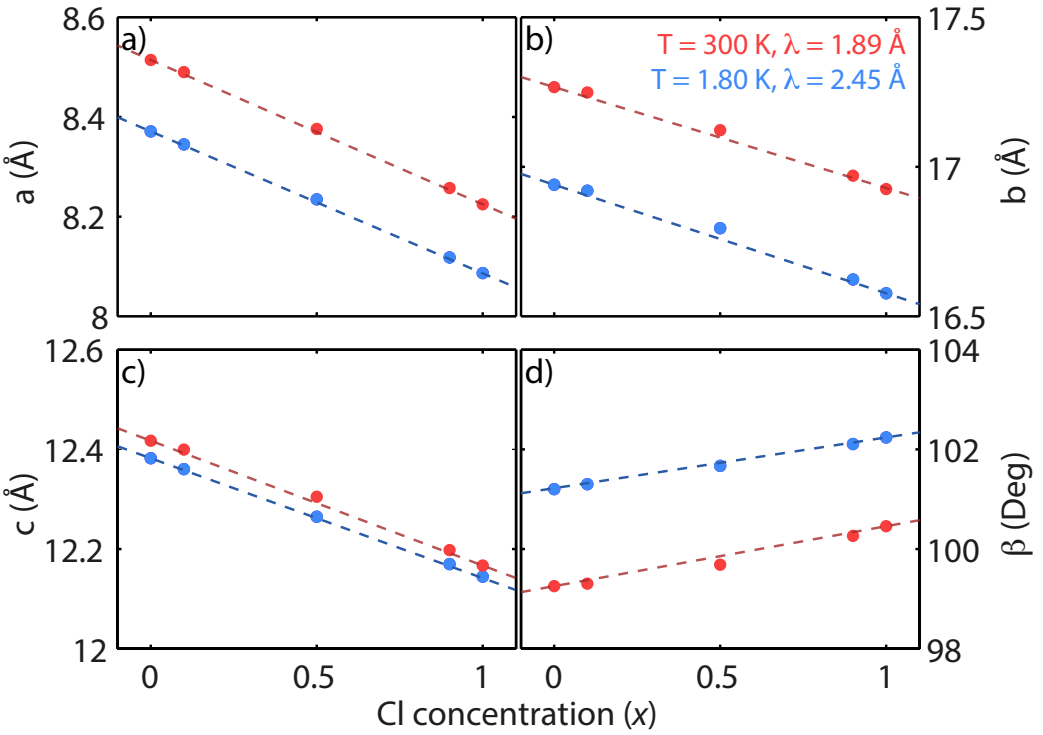

Figure 4.5: Lattice parameters of $BPCBC_x$ at 300 (red points) and 1.8K (blue points). Dashed lines correspond to linear fits to the data, suggesting that Vegard's law applies to the $BPBCB_x$ series.

Atomic positions and Br/Cl ratios have been simultaneously fitted in the refinement procedure detailed above. On considering the underlying ladder exchange structure the responsible halogen sites are obtained. An example can be found in figure 4.1. As shown in a schematic interaction map, only three of the halogen sites in the halogen tetragonal surrounding Cu^{+2} play a direct role in exchange interactions. These sites have been labelled 1, 2 and 3. The rung interaction consists of a double site 1 to site 3 exchange which is generate by the symmetry operation of the spacegroup. The leg interaction is formed from exchange across site 2 and 3.

x	**a** (Å)	**b** (Å)	**c** (Å)	β(°)
T = 300 K				
0.0	8.5145	17.2661	12.4173	99.2549
0.1	8.4900	17.2484	12.3992	99.3038
0.5	8.3758	17.1221	12.3047	99.6831
0.9	8.2573	16.9701	12.1979	100.2644
1.0	8.2245	16.9252	12.1668	100.4573
T = 1.8 K				
0.0	8.3707	16.9395	12.3818	101.1996
0.1	8.3449	16.9197	12.3600	101.3008
0.5	8.2347	16.7947	12.2645	101.6689
0.9	8.1178	16.6228	12.1697	102.1044
1.0	8.0866	16.5770	12.1446	102.2395

Table 4.2: Lattice parameters refined from neutron powder diffraction taken at HRPT (PSI - Villigen) for $BPCBC_x$ at 300 and 1.8 K. The refinement procedure is described in the text.

Importantly this suggests that site 4 does not play a role in the interaction structure and that any substitution on site 3 will effect both the rung and leg interaction.

Refinement of the Br/Cl ratios at the four halogen sites for the series are given in table 4.3 and graphically in figure 4.7. The value of x given until now is the nominal x from the stoichiometric ratios of starting materials. As previously described, the precise ratio can be affected by many factors. The site averaged chlorine concentration is given in the final column of table 4.3. At low to mid chlorine concentrations the site average is above what is expected. A possible explanation is that excess chlorine was introduced from the addition of HCl, which aids the crystallisation. At high values of x the site average ratio approaches the nominal value, which is compatible with the previous explanation.

The site concentrations also show that some sites are more favourable than others. Of interest is site 2 as it has consistently low substitution ratios and site

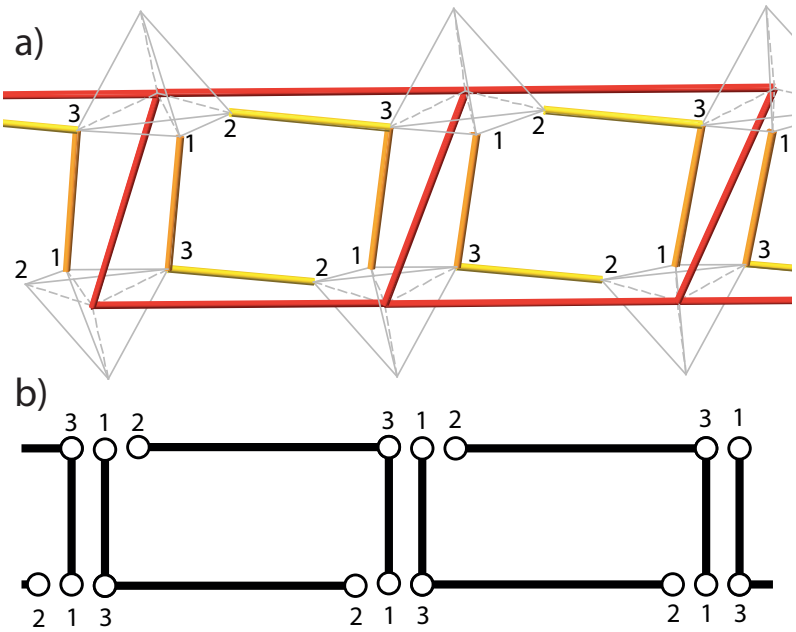

Figure 4.6: Halogen sites participating in exchange pathways of $BPCBC_x$. Top) Atomic positions in BPCB where red lines represent the ladder exchange structure. Orange lines represent rung exchanges and yellow leg exchange.Bottom) Illustration of the exchange structure when the halogen sites are labelled. Sites 1-3 form rung exchanges and sites 2-3 leg exchanges.

3 which has ratios marginally below the site average. The leg exchange across site 2 and 3 would therefore be less susceptible to the effect of substitution. Site 1 however shows the highest proclivity towards substitution, with the largest ratio. If site concentration is the only consideration to exchange strength, then the rung exchanges would show a marked decrease with substitution. Site 4 does not play a role in the exchange structure but also has a larger than expected occupancy which might add to strain and deformation of the tetragonal cage.

.

The Br/Cl ratio will affect the exchange, but does not exclusively determine the interaction strength. Bond length is a crucial factor as exchange strength decays via a power law with distance. Also it has been suggested that bond angle plays a more important role in exchange strength of metal-organic compounds [54, 55]. These parameters are shown in figure 4.8. The bond lengths for sites 1-3 and 2-

x	Site 1	Site 2	Site 3	Site 4	Average Composition
0.0	0.0000	0.0000	0.0000	0.0000	**0.0000**
0.1	0.3997	0.0353	0.1333	0.3436	**0.2280**
0.5	0.8063	0.4133	0.4310	0.5425	**0.5483**
0.9	0.9593	0.8855	0.8610	0.8489	**0.8887**
1.0	1.0000	1.0000	1.0000	1.0000	**1.0000**

Table 4.3: Observed site occupancy for a Cl atom at various sites (see figure 4.6). Data is obtained from the refinement of the crystal structure by neutron powder diffraction. For details see text.

3 show a slight x dependence, however this is small. The bond angles of the sites participating in the leg exchange show a high x dependence. There are two angles to consider, between the Cu^{2+} ion and site 3-2 and the Cu^{2+} ion and site 2-3. These are inequivalent. Turnbull *et al.* [54] performed a meta-analysis of tetrabromocuprate compounds, analysing the correlations between bond length, angle and structure and exchange strength. The sum of these inequivalent angles was studied and a correlation between bond angle and exchange strength determined. The total bond angle is limited to 360° and as bond angles approach this limit the exchange increases due to wave-function overlap [54]. For the $BPCBC_x$ series this also points to an increasing exchange with x.

.

4.1.3 Single crystal characterisation

The process described in section 4.1.1 can produce high quality single crystal samples. But samples grown by evaporation from solution can have defects that are invisible to x-ray diffraction. Voids can exist in the sample bulk containing Hpip solution. Evidence of these defects cannot be found by surface probes and as such neutron diffraction is invaluable in quantifying the single crystal quality. This section will cover the process of sample characterisation and quality determination.

It has been found by previous experience that the main factor influencing sam-

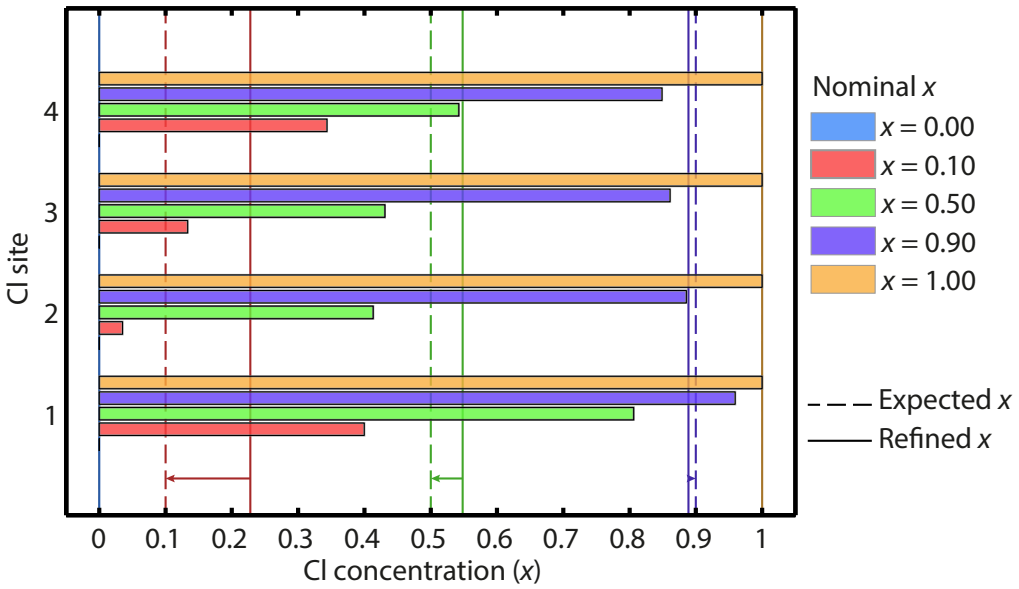

Figure 4.7: Site occupancy of halogen atoms participating in exchange pathway formation as shown in figure 4.6. Shown as horizontal coloured bars is the chlorine concentration at each site, the colour representing a nominal x value. Vertical dashed lines correspond to the nominal x value and solid lines to the site average.

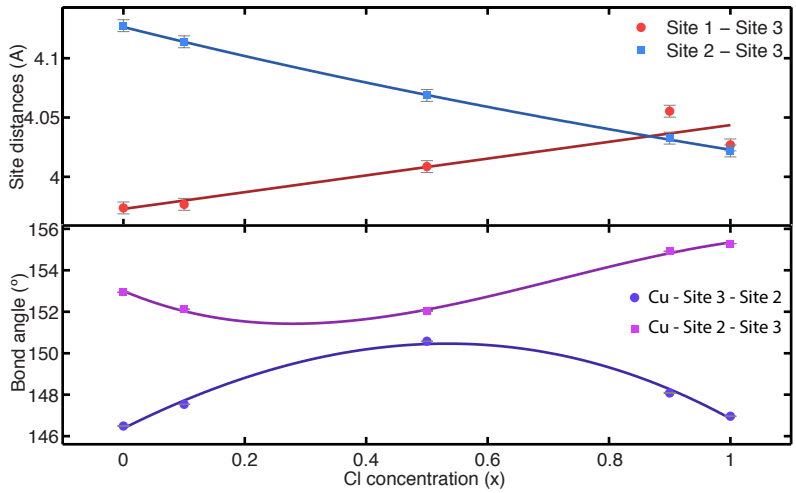

Figure 4.8: Bond lengths and bond angles as a function of composition in $BPCB_x$. Top) Bond lengths between sites 1 and 3 and sites 2 and 3. Bottom) Bond angles between the magnetic Cu^{2+} ion and the sites 3-2 and 2-3. Solid points correspond to the data and solid lines are guides to the eye.

ple quality is the sample volume. Above a sample of mass of 300 mg the rate of significant defects increases. Samples with masses above 500 mg are also available though are typically unusable for experiments due to defects.

To quantify sample quality the 4-circle neutron diffractometer Morpheus (PSI, Villigen) was used to characterise every sample. Neutron diffraction obtains the sample orientation and Bragg peak intensity. In neutron scattering experiments samples in the ac-plane are often advantageous as a magnetic field can be applied perpendicular to the ladder direction. The preferred crystal growth orientation are plates in the a-c plane $\approx$ 60 % of the time. With a unique b-axis there are 3 possible cell choices for a monoclinic structure, one unique and the other two are mirror reflections of each other. This leads to handedness and the possibility of twinning.

The Bragg allowed reflections [2 0 0] and [0 0 2] are good choices for sample characterisation due to their crystallographic orthogonality and intensity. Lattice parameters and integrated intensity per unit mass were collected and tabulated against known reference samples. The intensity ratio of these reflections points to possible twinning and integrated intensity to crystal quality. Table 4.4 shows the determination of acceptable BPCC samples. Using these methods only the best samples are selected and can then be co-aligned, e.g. for neutron spectroscopy experiments.

Co-alignment of between 6 and 14 crystals is usually performed to create a sample of approximately 1.5-2 g of total sample mass. The mount is constructed from high purity copper or aluminium depending on the experiential space and temperature requirements. Typically all samples are aligned to within 0.4° and to within 0.1° out of plane along the a-axis and 0.5° out of plane along the c-axis. The out-of-plane anisotropy is due to the limitations of the sample mount. An example mounting and resulting alignment can be found in figure 7.5.

Sample	$\mathbf{I_{[2\,0\,0]}/I_{[0\,0\,2]}}$	$\mathbf{I_{[2\,0\,0]}/mg}$	$\mathbf{I_{[0\,0\,2]}/mg}$	**Usable**
Calculated	2.287	-	-	-
Reference	2.318	2.832	1.22	-
a)	2.383	2.496	0.954	Yes
b)	6.785	1.779	0.262	Twinned
c)	-	0.915	-	Wrong morphology

Table 4.4: Calculated and reference intensities for BPCC single crystals on the 4-circle diffractometer Morpheus in high resolution mode. Samples a-c) show typical results from Bragg scans of the [2 0 0] and [0 0 2] reflections. Sample a) is of good quality as it is of the correct morphology, un-twinned and has acceptable integrated intensity per mg. Sample b) shows twinning along the a-axis and sample c) is the incorrect orientation (not in the ac-plane).

4.2 Exchange determination by magnetic susceptibility of BPCBC$_x$

In this section DC magnetic susceptibility measurements have been taken using a Quantum Design Magnetic Properties Measurement System (MPMS) at the LCN (UCL - London). The operating principle of the MPMS is descried in section 3.2.1.

Magnetic susceptibility χ is defined as;

$$\chi = \frac{M}{H}, \tag{4.1}$$

where M is the magnetisation of the sample and H is the applied static magnetic field. Magnetisation is defined as the magnetic moment per unit volume, where the magnetic moment arises from the spin of static or itinerant electrons. In the BPCBC$_x$ series the magnetic susceptibility is expected to be strongly dependent on the substitution parameter x. Magnetic susceptibility measurements can be used to suggest magnetic exchanges, such as in the frustrated 2-leg spin ladder $BiCuPO_6$ [56] where the ratio of some couplings was suggested by ab-initio methods and fits to experimental data using quantum Monte Carlo. Or in the spin chain material Sr_3CuPtO_6 [57] where the exchange interaction was determined by the Bonner-Fisher model.

Powder samples of BPCBC$_x$ were synthesised at the University of Bern (Switzerland) and the value of x determined by EDX measurements by the process described in section 4.1.1. Sample masses between 40-90 mg were measured between base temperature (1.8 K) and room temperature (300 K).

Magnetic susceptibility for the substitution series is shown in figure 4.11 for the temperature region $1.8 \leq T \leq 25$ K. In this region an exponential increase in susceptibility is expected due to the spin gap of an even leg ladder system. This feature is present in all compounds. The maximum in susceptibility corresponds to first approximation the exchange J_r. Other gapped models such, zig-zag chains [58] amongst others have a similarly shaped susceptibility curves. For analysing the data the choice of model Hamiltonian can be unclear, though in BPCBC$_x$ all previous work and the structural determination above strongly suggests that the spin ladder Hamiltonian is applicable.

4.2.1 Data analysis and interpretation

The aim of the analysis of the magnetic susceptibility data is to extract the magnetic exchanges. The total measured susceptibility χ_T is the sum of 3 components:

$$\chi(T) = \chi_D + \chi_{imp}(T) + \chi_S(T, J_r, J_l) \tag{4.2}$$

where χ_S is the simulated susceptibility from a spin model, χ_D is the diamagnetic contribution to the susceptibility. This has been calculated from the elemental components of the series[b]. Impurities consist of either vacancies or free spins are present in the sample and contribute to χ_{imp}.

$$\chi_{imp}(T) = \chi_{vac}(T) + \chi_{mag}(T) \tag{4.3}$$

$$\chi_{imp}(T) = \frac{C_{vac}}{T+\theta_c} + \frac{C_{mag}}{T} \tag{4.4}$$

Vacancies in the spin ladder structure typically arise due to crystal defects, which are common when using the evaporation from solution technique. These can be modelled by a Currie-Weiss term $\chi_{vac}(T)$ where the characteristic temperature θ_c is given by $\theta_c = (J_r + 2 \cdot J_l)/4$ [59]. Magnetic impurities from free spins arise from magnetic contaminants. $\chi_{mag}(T)$ is typically small as the leading contributions can be suppressed with proper technique and high quality starting materials.

The simulated theoretical magnetic susceptibility χ_S can be calculated through expansion techniques such as High Temperature Series Expansions (HTSE), perturbation theory, or other numerical methods such as bond operator theory [60]. Numerical methods such as Quantum Monte Carlo (QMC) and Exact Diagonalisation (ED) provide useful tools for simulating susceptibility data. For this thesis ED has been chosen to simulate the susceptibility by use of the ALPS package [61]. ED provides exact results for a given system size by diagnolising the entire spin matrix and evaluating the magnetic properties from the eigenvalues at various temperatures. The advantage of ED is that for a given exchange ratio the results are robust down to low temperatures. Figure 4.9 shows ED simulations ranging from the strong coupling limit $J_l/J_r \to 0$ (isolated dimer) and the weak coupling limit $J_l/J_r \to \infty$ (spin chain).

[b] Diamagnetic susceptibility for complex organic molecules can be radically different from the sum of elemental components. In reference [25] χ_D is estimated to be between -2.84 and $-2.64 \cdot 10^{-4}$ emu/mol from the sum of core diamagnetism and from Pascals constants.

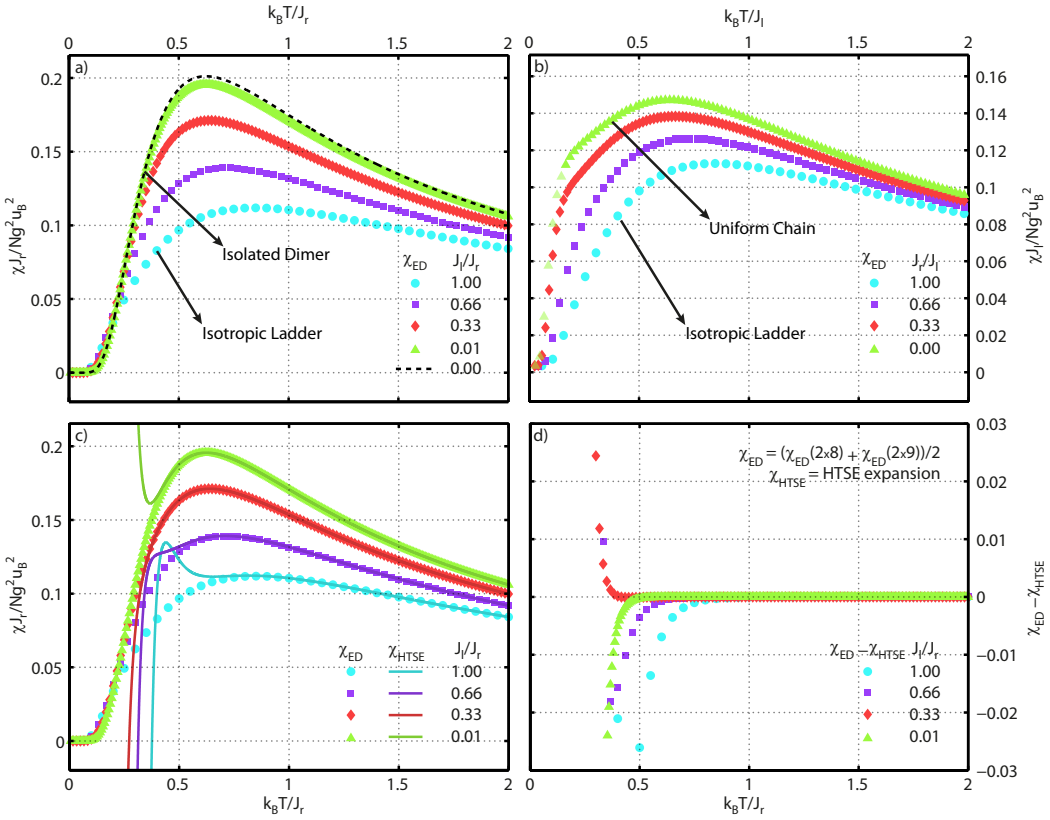

Figure 4.9: ED simulations of magnetic susceptibility for various ratios of exchange parameters. a) shows the approach to the strong coupling dimer limit where the black line is the exact solution to an isolated dimer. b) opposite limit, approaching a spin chain. For an explanation of the apparent gapped ground state see text. c-d) show susceptibility in the strong coupling limit by HTSE and the temperature where divergences occur.

In figure 4.9 a) the susceptibility for an isotropic ladder approaching an isolated dimer is shown. The black dashed line is the exact susceptibility of an isolated S = 1/2 dimer as given by [59]:

$$\chi_{dimer}(t) = \frac{1}{t\left(3 + e^{1/t}\right)}, \tag{4.5}$$

where t is the dimensionless temperature given by $t = k_BT/J$ where J is the dimer exchange. ED simulations in the strong coupling limit approach this exact solution as $J_l/J_r \to 0$ for all temperatures. In the figure the average susceptibility of simulations of 16 and 18 spins in the spin ladder model is plotted and shows excellent

agreement. The isotropic ladder to spin chain case is presented in figure 4.9b. For the ideal spin chain ($J_l/J_r = \infty$) the ground state is gapless and hence has finite susceptibility. Shown in green is $J_r/J_l = 0$ for a 18 spin chain. Below $t = 0.2$ the results for this diagonalisation are dependent on system size. A HTSE of the spin ladder model in the strong coupling limit has been proposed by [62] and is shown with ED in figure 4.9c). The HTSE diverges from the ED solution at approximately $t < J_r/J_l$ as shown in figure 4.9d).

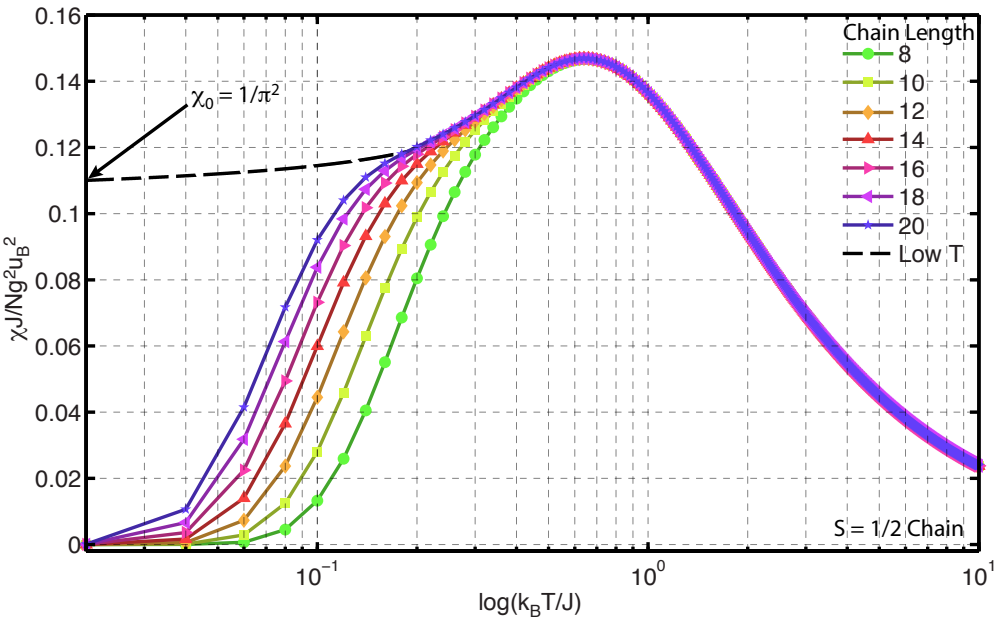

Figure 4.10: Length dependence of the low temperature magnetic susceptibility of a S = 1/2 chain by exact diagonalisation in logarithmic scale. The dashed black line is a low temperature expansion from reference [63]. On increasing system size magnetic susceptibility converges to the expected finite value $\frac{1}{\pi^2}$ at T = 0. In a finite length S = 1/2 chain extrapolations to infinite length are needed to retrieve the expected value in the thermodynamic limit.

The effect of finite size is shown in Figure 4.10. The spin chain case is studied as low temperature divergences due to finite size are more pronounced. Chain lengths (L) of 8-20 spins are shown along with a low temperature expansion from reference [63], which is accurate to 10^{-7}·J for the range shown. In the case of $L = 8$ accuracy is lost at 1·J, progressing to 0.2·J for $L = 20$. For the case of the spin

chain extrapolation to $L = \infty$ is needed to obtain $t = 0$ results.

The compounds BPCB and BPCC are in the strong coupling limit with $J_r/J_l > 1$. For the substituted BPCBC$_x$ series it is expected that this will be a valid assumption. As shown in figure 4.9a,c ED provides a more accurate solution that HTSE in the coupling ratio $J_r/J_l \geq 1$ and hence it is used for extracting the exchanges from the experimental susceptibility. A grid of simulations in the spin ladder model with exchanges $2 \leq J_r \leq 15$ K and $1 \leq J_l \leq 6$ K was performed for 16 and 18 spins. The resulting susceptibility was used as χ_S in equation 4.2.

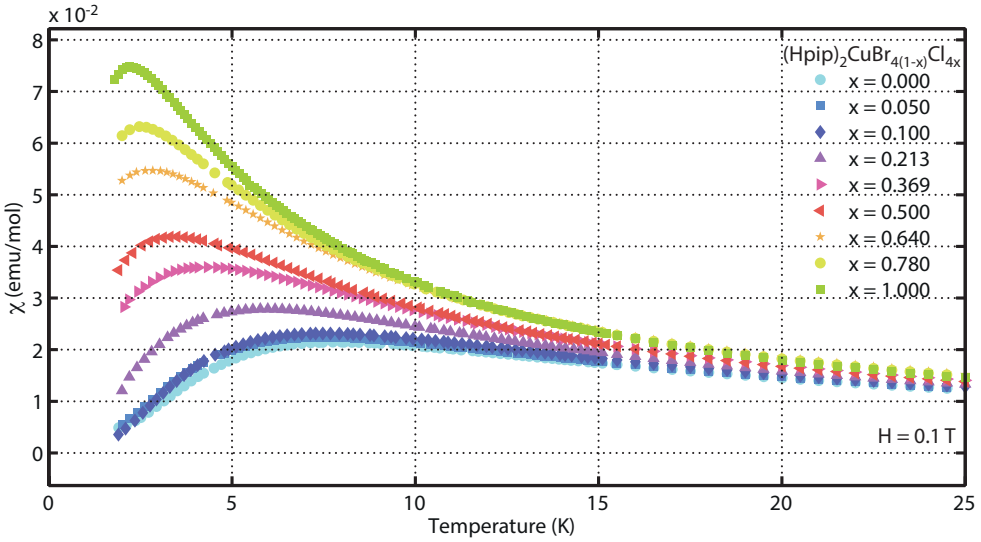

Figure 4.11: Magnetic susceptibility of the BPCBC$_x$ series measured on a Quantum Design MPMS with an applied field of 0.1 T. The susceptibility maxima shift inversely proportional to x suggesting reduced exchange. Data for BPCB is consistent with the results by Watson *et al.* in reference [25].

Susceptibility data for various x of BPCBC$_x$ is shown in figure 4.11. The maxima in susceptibility shifts inversely with x and the peak with decreases, indicating a reduction in both J_r and J_l. The paramagnetic impurities show a low temperature upturn as expected, which is most clearly illustrated for $x = 0 - 0.1$. For higher x the impurity and ladder signal overlap due to the temperature range of the data.

The necessary parameters in equation 4.2 were fitted between appropriate bounds for all χ_S. The quality of each fit (χ^2) was used to determine the best

overall set of exchange parameters and impurity concentrations. This method will be called *Method 1*. In many cases multiple solutions are found and a unique solution cannot be obtained. By fitting the goodness of fit in the J_r, J_l plane to a bivariate skewed Gaussian both accurate errors and average exchanges can be determined. This method will be called *Method 2*.

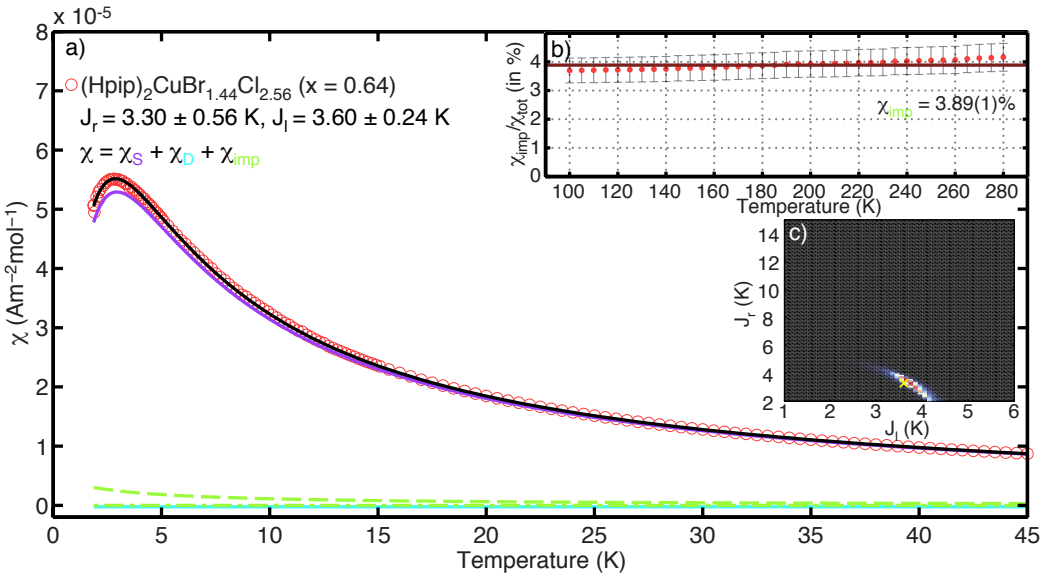

Figure 4.12: Magnetic susceptibility of BPCBC$_{0.64}$. a) Contributions to the magnetic susceptibility (black line) from a simulated spin ladder with $J_r = 3.3$ K, $J_l = 3.6$ K (purple line), diamagnetic contribution (light blue) and impurities (green line dashed for vacancies, dash-dotted for magnetic impurities). b) Impurity concentration as a function of temperature where $\chi_{imp} = 3.89(1)\%$, with a dominant contribution from vacancies. c) Goodness-of-fit map showing all possible solutions and the accepted solution (yellow cross).

An example fit is shown in figure 4.12 where the main panel shows the components of the total susceptibility. The best simulated susceptibility curve is for BPCBC$_{0.64}$ is with $J_r = 3.3$ K, $J_l = 3.6$ K and the corresponding diamagnetic and impurity contributions. The impurity contribution in the sample is 3.89(1)% and that consists of magnetic impurities and site vacancy impurities. The Impurity concentration is determined by performing a sliding fit consisting of 9 data points to a Curie law well into the paramagnetic phase ($T > 100$ K) to obtain the paramagnetic

Currie constant C_{para}. The impurity concentration defined as $(C_{vac} + C_{mag})/C_{para}$ as a function of temperature is shown in figure 4.12b and is linear. Figure 4.12c contains the goodness of fit map for all possible J_r and J_l solutions. The sweeping red curve denotes acceptable solutions and the yellow cross represents the final solution after fitting to a bivariate skewed Gaussian.

	Method 1		*Method 2*		
x	**J_r (K)**	**J_l (K)**	**J_r (K)**	**J_l (K)**	**Gap (meV)**
0.00	12.90 (5)	3.40 (5)	12.82 (21)	3.70 (60)	0.80 (4)
0.10[a]	11.60 (5)	4.80 (5)	11.78 (23)	4.32 (45)	0.71 (1)
0.21	8.70 (5)	5.20 (5)	9.21 (62)	4.68 (56)	0.52 (9)
0.37	5.10 (5)	5.20 (5)	5.67 (81)	4.96 (40)	0.35 (20)
0.50[ab]	4.20 (5)	4.30 (5)	3.81 (62)	4.55 (34)	0.29 (18)
0.64	4.10 (5)	3.40 (5)	3.69 (72)	3.48 (32)	0.22 (27)
0.78	3.30 (5)	2.70 (5)	3.41 (47)	2.64 (30)	0.23 (11)
0.90[ab]	3.80 (5)	2.50 (5)	3.42 (51)	2.66 (39)	0.24 (16)
1.00	3.60 (5)	1.20 (5)	3.51 (17)	1.36 (26)	0.22 (5)

Table 4.5: Exchange parameters and associated errors for the BPCBC$_x$ series as determined from fits to magnetic susceptibility data. Method 1 and Method 2 are described in the text.

[a] Exact compositions are not available for these samples.
[b] Mixing in the signal from ladder and impurities might make these exchanges unreliable.

The resulting exchanges values for all x are summarised in table 4.5 and figure 4.13. Both *Method 1* and *Method 2* accurately determine the exchanges of the parent compounds BPCB and BPCC, for $J_l/J_r < 1$ finite size ED is ideally suitable for exchange determination. The average rung exchange for BPCBC$_x$ decreases rapidly on increasing x, plateauing at $x \approx 0.6$. From powder diffraction data Cl has a preference for site 1 (figure 4.6), which directly affects only the rung exchange and accounts for this observation. The increase in leg exchange between $0 > x \geq 0.5$ is due to the increasing angle (ψ) between Cu^{+2} - Site 2 - Site 3. In a review of tetrabromocuperate compounds by Turnbull *et al.* [54] it was found that

the angle between the Cu^{2+} site and the super-exchange pathway strongly effects the exchange value, the exchange becoming greater as $\psi \to 180°$. At $0.5 > x \geq 1$ the angle ψ reduces, which the exchange follows. In the fitting process at $x = 0.5$ the number of acceptable solutions increases (see errors in table 4.5). This is partially due to interference between the χ_{imp} contribution and χ_S. Limiting the impurity contribution to $\chi_{imp} \leq 0.1\chi_{para}$ reduces the possible solutions. However, the many possible solutions are also due to the extracted exchanges being a statistical average of all chemical configurations whose number is maximised around $x = 0.5$. Vacancies in the ladder structure lead to correlated S = 1/2 Cu^{2+} ions that produce a field independent Curie Weiss behaviour (χ_{vac}) and uncorrelated paramagnetic impurities (χ_{mag}) follow the Curie law for paramagnetic materials. In our samples magnetic impurities account for ≈ 0-0.2% of the paramagnetic contribution which stays constant with substitution. There is a positive correlation between vacancies and substitution when x is above 0.5. Typically all impurities account for 1-4% of the samples paramagnetic contribution to the total susceptibility. In the case of $x > 0.5$ the fitted paramagnetic contribution is ≈ 18%. This is probably an artefact of the fitting procedure as described in section 4.2.1.

The dimer expansion for the spin gap by perturbation theory to 7th order has been calculated by Piekarewicz *et al.* in [64] and is valid for $J_l/J_r < 1$. Applying this to the exchange parameters in table 4.5 provides an estimate of the spin gap, which decreases rapidly as a function of x. For $x \geq 0.5$ the gap remains constant at ≈ 0.22 meV.

4.3 Thermodynamics of BPCC

Thermodynamic measurements on BPCC and the $BPCBC_x$ series have been performed as a part of the thesis of H. Ryll (HZB - Berlin). The results presented in the following section have been extracted from our joint PRB paper on the subject (reference [46]).

A single crystal of BPCC of mass 3.73(1) mg has been mounted in the bc-plane and the magnetic heat capacity c_{mag} and the magneto-caloric effect (MCE) measured using the calorimeter described in section 3.3. Temperature and magnetic

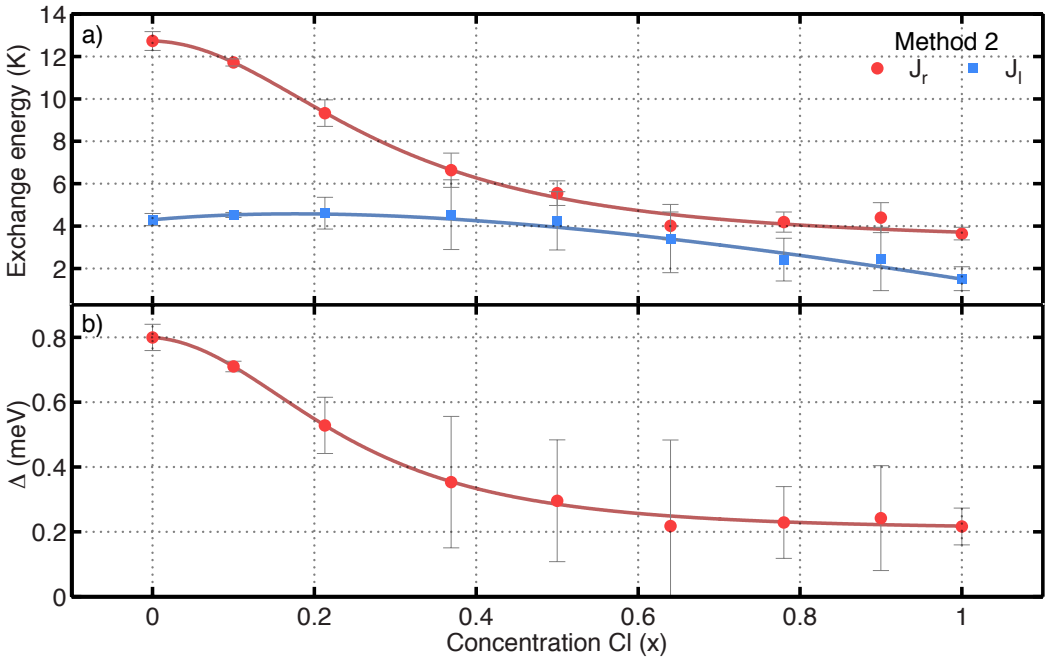

Figure 4.13: Exchange parameters J_r and J_l determined by *Method 2* as described in the text is shown (Top) where solid lines are a guide to the eye. (Bottom) Gap (Δ) in meV calculated from 7th order perturbation theory from reference [64].

field sweeps were performed between 90 mK and 30 K and 0 to 12 T with data collected by the quasi-adiabatic method.

4.3.1 Phase diagram from magnetic entropy

The magneto-caloric effect is linked to magnetic entropy via;

$$\frac{1}{T}\frac{\delta Q}{dB} = -\frac{dS}{dB} = \left.\frac{\partial M}{\partial T}\right|_B . \tag{4.6}$$

Hence it's possible to recover the entropy data by integrating MCE effect data with respect to field. This has been performed for BPCC and the magnetic entropy landscape is shown in figure 4.14.

Figure 4.14: Phase diagram of BPCC by magnetic entropy shown by a false colour map. Magnetic phases given are defined in chapter 2. Quantum critical points are shown and as red filled circles and the low temperature boundary of the Luttinger-liquid phase is found by magnetisation measurements (red crosses). Figure taken from reference [46]

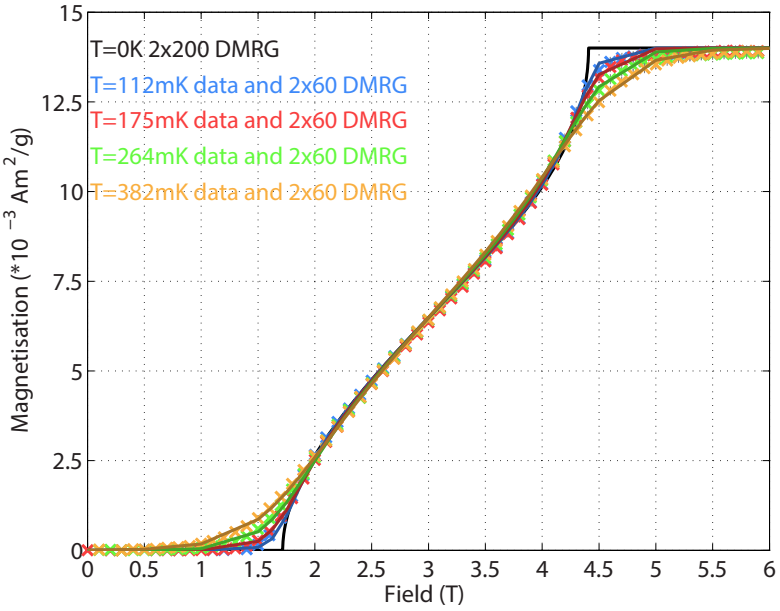

Figure 4.15: Low temperature magnetisation of BPCC. Crosses represent data taken by torque magnetometry between 112 and 382mK. Solid coloured lines are DMRG simulations using the exchange parameters given in equation 5.21. The solid black line represents zero temperature magnetisation curve, where the square root power law at the critical points is visible.

The magnetic entropy phase diagram shares many characteristics of the specific heat phase diagram shown in figure 2.6. In the quantum disordered and field polarised phase the magnetic entropy is minimal. In the quantum disordered phase this is due to all spins being in the singlet state and in the field polarised state all spins are aligned with the applied field. Approaching the quantum critical points there is a build up of entropy, signalling the onset of the spin Luttinger-liquid phase as theoretically predicted [65]. In the lower part of the figure the phase boundary of the Luttinger-liquid phase is shown and has been derived from magnetisation measurements by a torque magnetometer as described in section 3.2.2. Magnetisation scans are shown in figure 4.15, where the critical points have been extracted from square root power law fits to the data.

4.3.1.1 Scaling near quantum criticality

The magnetic Grüneisen parameter (Γ_{mag}) is a highly sensitive tool for detecting the the entropy build up at quantum critical points. The Grüneisen parameter is defined as

$$\Gamma_{mag} = \frac{\partial M/\partial T}{c_{mag}} = \frac{1}{T}\frac{\delta T}{\delta B}\bigg|_S . \tag{4.7}$$

The Grüneisen parameter is suited to the study of phase transitions at finite temperature but approaching zero temperature as it undergoes a sign change in proximity to a quantum critical point [66]. The Grüneisen parameter has been successfully measured for other low dimensional systems [67, 68].

For BPCC the heat capacity c_{mag} has been measured along with the MCE. The calculated Grüneisen parameter is shown in figure 4.16 (Left) with comparisons to numerical models. The sign change at the quantum critical point can be acquired through the differential of the parameter with respect to field.

Figure 4.16: Grüneisen parameter and critical scaling in BPCC. Left) Grüneisen parameter calculated for various temperatures form heat capacity and MCE measurements. Data is shown by points and solid lines correspond to simulations by exact diagonalisation. Dashed lines corresponding to the XXZ model and are described in reference [46]. Right) Temperature dependence of Γ_{mag} at the critical magnetic fields. Data is shown as points, DMRG solid lines and the XX chain model as a dashed line. The axes are normalised to the rung exchanges J_r. Images taken from reference [46]

The temperature dependence of the Grüneisen parameter is defined by a power

law behaviour and as such a critical scaling parameter in the vicinity of a quantum critical point exists. The temperature dependence of Γ_{mag} is shown in figure 4.16 (Right) for BPCB and BPCC. Due to the large range in energy scales for the two pure BPCBC$_x$ compounds the temperature dependence of the Grüneisen parameter can be tested for a large range of temperature values.

For a strongly dimerised spin ladder, mapping on to a XXZ chain Hamiltonian is often performed (see section 7.2). In the vicinity of the quantum critical points there are few excitations or holons and as such the Hamiltonian can be reduced to that of a XX chain at these points. The advantage of this is that the Hamiltonian for the XX chain is exactly solvable [69] and shown in figure 4.16 (Right). Also shown are DMRG results that also agree with the experimental data. By simultaneous fitting of both datasets the universal scaling parameter α has been extracted to be 1.0(1), where the theoretical asymptotic exponent is 1.

Chapter 5

Excitations in the quantum disordered phase

Contents

The quantum disordered phase as introduced in section 2.2 consists of a singlet ground state without long range order or correlations. Elementary excitations are from a singlet state to degenerate triplet states with a spin gap energy Δ. This gap exists for all finite values of the exchange interaction J_l. This spin gap and accompanying dispersion can be measured by inelastic neutron scattering and the spin ladder Hamiltonian confirmed. The spin ladder material BPCC has been extensively studied and exchange parameters identified

5.1 Elementary excitations in a model spin ladder

The Hamiltonian for a spin ladder is given below in equation 5.1. The Hamiltonian consists of three parts; coupling between spins on the ith rung with an exchange J_r, coupling between the ith spin in the jth chain with exchange J_l and the magnetic field which acts on the z component of the spin ($\mathrm{S}^z_{i,j}$).

$$\mathcal{H} = J_r \sum_{i=1}^{L} \mathbf{S}_{i,1} \cdot \mathbf{S}_{i,2} + J_l \sum_{j=1,2} \sum_{i=1}^{L-1} \mathbf{S}_{i,j} \cdot \mathbf{S}_{i+1,j} - g\mu_B h^z, \tag{5.1}$$

where h^z is the interaction between the spin and magnetic field in the z direction $\left(h^z = H^z \cdot S^z_{i,j}\right)$. Diagonalising the Hamiltonian leads to a number of states proportional to the ladder length L. The lowest energy excitations are singlets to triplets on the dimerised rungs:

$$|s\rangle = \frac{|\uparrow\downarrow\rangle - |\downarrow\uparrow\rangle}{\sqrt{2}}, \ \left|t^+\right\rangle = |\uparrow\uparrow\rangle, \ \left|t^0\right\rangle = \frac{|\uparrow\downarrow\rangle + |\downarrow\uparrow\rangle}{\sqrt{2}}, \ \left|t^-\right\rangle = |\downarrow\downarrow\rangle. \tag{5.2}$$

By application of magnetic field degeneracy of the triplet states are lifted by Zeeman splitting. The $|t^+\rangle$ and $|t^-\rangle$ states soften and gain energy $gu_B H_z$.

For non-interacting dimers the dispersion will be flat with energy J_r. For finite J_l singlet fluctuations exist which lower the gap energy. This lowering of the gap energy increases and the dispersion tends towards that of a spin chain for $\mathrm{J}_l/\mathrm{J}_r \to \infty$.

The ratio of the leg and rung exchange values is called the coupling ratio.

$$\gamma = \frac{J_l}{J_r} \tag{5.3}$$

With $\gamma \to 0$ the system can be described by weakly coupled dimers and $\gamma \to \infty$ by weakly coupled chains.

5.1.1 One magnon excitations

The dispersion as a function of J_l is shown for a selection of exchange ratios in figure 5.1.

In the strong coupling limit γ is a small parameter which can be expanded about and as such is the starting point to describe the dispersion by perturbation theory. The dispersion for a spin ladder has been calculated by Reigrotzki *et al.* [70] by

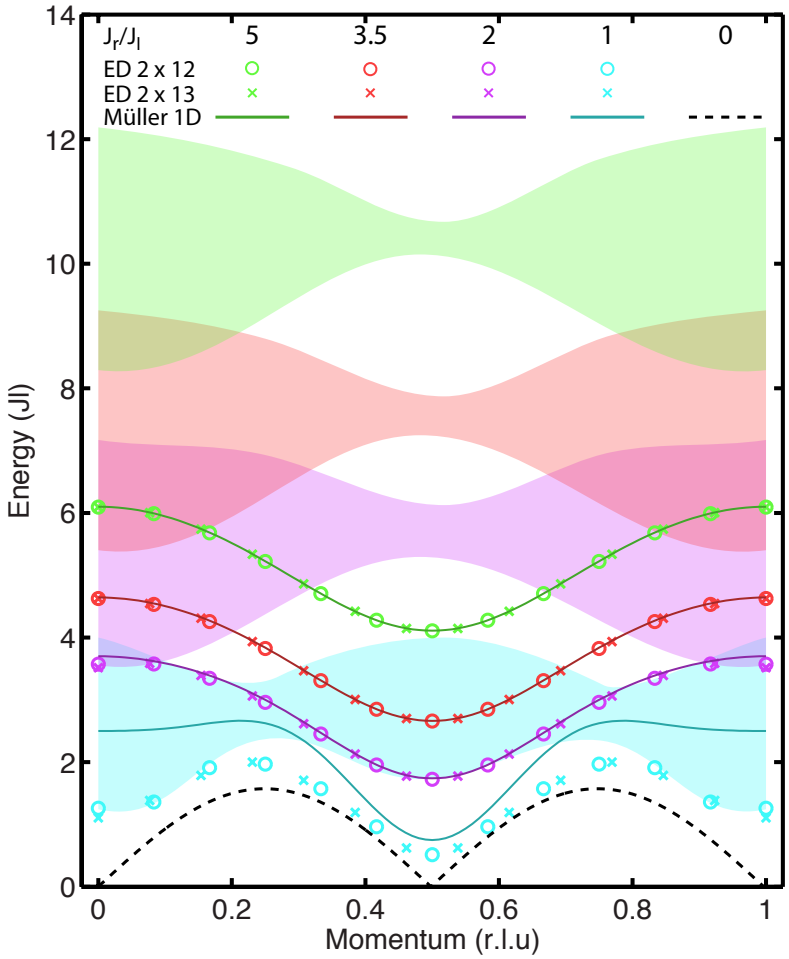

Figure 5.1: One magnon excitations as calculated by exact diagonalisation and Müller (equation 5.5).. The black dashed line represents the spin chain limit $\gamma = \infty$. Solid lines represent a finite J_r, where the gap energy increases with the decrease of J_l from equation 5.5. The shaded areas correspond to the two particle continuum, where excitations with in the triplet state exist. Also shown are the results of Lanczos diagonalisation of the Hamiltonian with 2x12 (open circles) and 2x13 (crosses) sites. The validity of which is discussed in the text.

perturbation theory to 3^{rd} order in γ. This is given in equation 5.4, where the momentum is k.

$$\begin{aligned}\frac{\omega\left(k\right)}{J_r} =& 1+\gamma\cos\left(2\pi\cdot k\right)+\frac{1}{4}\gamma^2\left(3-\cos\left(4\pi\cdot k\right)\right)\\ &-\frac{1}{8}\gamma^3\left(2\cos\left(2\pi\cdot k\right)+2\cos\left(4\pi\cdot k\right)-\cos\left(6\pi\cdot k\right)-3\right).\end{aligned} \tag{5.4}$$

A similar result has been obtained by Müller *et al.* [71]. In this case, expansion about γ was performed to third order and the case of a ladder with additional diagonal couplings J_d was considered. This diagonal coupling ratio $\gamma_d = \frac{J_d}{J_r}$ is not present in the $BPCBC_x$ series of compounds and is included for reference.

$$\begin{aligned}\frac{\omega(k)}{J_r} =& 1-\frac{1}{4}\gamma_d^2\left(1+\gamma\right)+\frac{3}{8}\left(\gamma-\frac{1}{2}\gamma_d\right)^2\left(2+\gamma-\frac{1}{2}\gamma_d\right)\\ &+\left[\gamma-\frac{1}{2}\gamma_d-\frac{1}{4}\gamma_d^2\left(1+\gamma\right)-\frac{1}{4}\left(\gamma-\frac{1}{2}\gamma_d\right)^3\right]\cos(2\pi\cdot k)\\ &-\frac{1}{4}\left(\gamma-\frac{1}{2}\gamma_d\right)^2\left(1+\gamma+\frac{1}{2}\gamma_d\right)\cos(4\pi\cdot k)\\ &+\frac{1}{8}\left(\gamma-\frac{1}{2}\gamma_d\right)^3\cos(6\pi\cdot k)\end{aligned} \tag{5.5}$$

It is important to note that the effect of J_d on the dispersion is very similar to J_l and as such may be experimentally difficult to separate. An in-depth discussion on the effect of J_d can be found in reference [49]. Also the work by Müller *et al.* includes the dispersion of 3D coupled dimers as coupled ladders. This has been included as it was successfully used to describe the dispersion in the double chain $S = 1/2$ compound $KCuCl_3$ [72]. This can be applied to BPCB to investigate the effects of inter-ladder couplings on the dispersion and obtain exchange parameters. The dispersion is given by;

$$\begin{aligned}\omega(\vec{q}) =& 1 + \delta\omega^{(1)}(\vec{q}) - \frac{1}{2}\delta\omega^{(1)^2}(\vec{q}) \\ &+ J_{(100)}\left(J_{(100)} - J'_{(100)}\right) - \frac{1}{4}J'^2_{(100)}\cos q_x \\ &+ J_{(0\frac{1}{2}\frac{1}{2})}J'_{(0\frac{1}{2}\frac{1}{2})} + J_{(1\frac{1}{2}\frac{1}{2})}J'_{(1\frac{1}{2}\frac{1}{2})} \\ &+ \frac{1}{2}\left(J^2_{(0\frac{1}{2}\frac{1}{2})} - J'^2_{(0\frac{1}{2}\frac{1}{2})}\right)\cos\frac{q_y}{2}\cos\frac{q_z}{2} \\ &+ \frac{1}{2}\left(J^2_{(1\frac{1}{2}\frac{1}{2})} - J'^2_{(1\frac{1}{2}\frac{1}{2})}\right)\cos\frac{q_y}{2}\cos\frac{2q_x+q_z}{2} \\ &- \frac{1}{4}J'^2_{(201)}\cos(2q_x + q_z),\end{aligned} \tag{5.6}$$

where

$$\begin{aligned}\delta\omega^{(1)}(\vec{q}) =& \frac{1}{2}\left(2J_{(100)} - J'_{(100)}\right)\cos q_x \\ &+ \left(J_{(0\frac{1}{2}\frac{1}{2})} - J'_{(0\frac{1}{2}\frac{1}{2})}\right)\cos\frac{q_y}{2}\cos\frac{q_z}{2} \\ &+ \left(J_{(1\frac{1}{2}\frac{1}{2})} - J'_{(1\frac{1}{2}\frac{1}{2})}\right)\cos\frac{q_y}{2}\cos\frac{2q_x+q_z}{2} \\ &- \frac{1}{2}J'_{(201)}\cos\left(2q_x + q_z\right).\end{aligned} \tag{5.7}$$

The interactions included in equation 5.6 are shown in figure 5.2.

The interactions $J_{(0\frac{1}{2}\frac{1}{2})}$ and $J_{(1\frac{1}{2}\frac{1}{2})}$ as defined in figure 5.2 have been found to express the 3D nature of BPCB, where the interaction is on the order of 50 mK [49].

Further to the work of Müller *et al.* , the expansion of γ has been extended in reference [73] to 8^{th} order. The non-zero coefficients are given in table 5.1.

Increasing the order of expansion adds corrections to the dispersion allowing for an increased validity in γ range. The validity ranges for equations 5.4, 5.5 and table 5.1 are explored in section 5.1.4.

5.1.2 Two magnon excitations

Previously we have only considered one magnon excitations, but it is also possible to create multi-magnon excitations. The two magnon continuum shown in figure 5.1 arises from applying momentum and energy conservation to two one magnon excitations. A particle in the continuum has momentum $\vec{q} = \vec{q_0} + \vec{q_1}$ and energy $\Omega = \omega(\vec{q_0}) + \omega(\vec{q_1})$.

Figure 5.2: Magnetic structure of $TlCuCl_3$ showing the 3D structure of the interactions. Exchanges labeled are used in equation 5.6. Taken from reference [71]

In materials where the one magnon and two magnon continuum overlap there is a critical point at which the one magnon dispersion terminates (k_c). At this point there is a bifurcation in the excitation spectra relating to the formation of bound pairs of magnons. These pairs are kinematically unstable at the decay threshold and decay into a pair of quasiparticles with equal momenta [74]. This has been shown for liquid Helium and the 2D quantum magnet PHCC [75]. However the crystal structure of $BPCBC_x$ has two inequivalent ladders resulting in constructive and deconstructive interference. This interference leads to a separation of one and two magnon channels (with different parities) in reciprocal space. These channels are called scattering channels, π for odd parity and 0 for even parity excitations.

(n,m)	$a_{n,m}$	(n,m)	$a_{n,m}$	(n,m)	$a_{n,m}$	(n,m)	$a_{n,m}$
(0, 0)	1.000000000	(5, 1)	$-2.031250000\cdot10^{-1}$	(3, 3)	$1.250000000\cdot10^{-1}$	(5, 5)	$5.468750000\cdot10^{-2}$
(2, 0)	$7.500000000\cdot10^{-1}$	(6, 1)	$9.375000000\cdot10^{-2}$	(4, 3)	$1.250000000\cdot10^{-1}$	(6, 5)	$7.812500000\cdot10^{-2}$
(3, 0)	$3.750000000\cdot10^{-1}$	(7, 1)	$3.293457031\cdot10^{-1}$	(5, 3)	$-9.375000000\cdot10^{-2}$	(7, 5)	$-6.042480469\cdot10^{-2}$
(4, 0)	$-2.031250000\cdot10^{-1}$	(8, 1)	$2.555847168\cdot10^{-1}$	(6, 3)	$-3.164062500\cdot10^{-1}$	(8, 5)	$-2.657165527\cdot10^{-1}$
(5, 0)	$-6.250000000\cdot10^{-1}$	(2, 2)	$-2.500000000\cdot10^{-1}$	(7, 3)	$-2.222900391\cdot10^{-1}$	(6, 6)	$-4.101562500\cdot10^{-2}$
(6, 0)	$-5.000000000\cdot10^{-1}$	(3, 2)	$-2.500000000\cdot10^{-1}$	(8, 3)	$2.752685547\cdot10^{-1}$	(7, 6)	$-6.835937500\cdot10^{-2}$
(7, 0)	$2.966308594\cdot10^{-1}$	(4, 2)	$-3.125000000\cdot10^{-2}$	(4, 4)	$-7.812500000\cdot10^{-2}$	(8, 6)	$4.957580566\cdot10^{-2}$
(8, 0)	1.120300293	(5, 2)	$2.031250000\cdot10^{-1}$	(5, 4)	$-9.375000000\cdot10^{-2}$	(7, 7)	$3.222656250\cdot10^{-2}$
(1, 1)	1.000000000	(6, 2)	$1.718750000\cdot10^{-1}$	(6, 4)	$7.128906250\cdot10^{-2}$	(8, 7)	$6.152343750\cdot10^{-2}$
(3, 1)	$-2.500000000\cdot10^{-1}$	(7, 2)	$-1.728515625\cdot10^{-1}$	(7, 4)	$2.690429688\cdot10^{-1}$	(8, 8)	$-2.618408203\cdot10^{-2}$
(4, 1)	$-3.125000000\cdot10^{-1}$	(8, 2)	$-5.047454834\cdot10^{-1}$	(8, 4)	$1.690521240\cdot10^{-1}$		

Table 5.1: Series coefficients for the dimer expansion for one magnon excitations of a two-leg spin ladder. $\omega(k) = \gamma^{-1}\sum_{n,m} a_{n,m}\gamma^n \cos(2m\pi\cdot k)$. Nonzero coefficients $a_{n,m}$ up to order $n = 8$ are listed. From reference [73].

5.1.3 Dynamical structure factor

Possible excitations for all scattering channels are summarised in table 5.2 which has been taken from reference [7]. The origin of the excitation, excitation parity and change in magnetisation is given. Also present is the scattering channel in which the excitations occur.

The structure factor for the one magnon excitation that occurs in the π sector can be approximated by the single-mode approximation [76]. Most of the spectral weight is associated to the singlet-triplet mode. Such an approximation has been used by Tennant *et al.* in the dimerised spin chain copper-nitrate [15] and has been successfully applied to BPCB [49]. The scatting from the dominant mode is given by:

$$S^{\alpha\beta}(\mathbf{Q},\hbar\omega) = S(\mathbf{Q})\,\delta(\hbar\omega - \hbar\omega(\mathbf{Q}))\,\delta_{\alpha\beta}, \tag{5.8}$$

where $S(\mathbf{Q})$ is obtained from[77],

$$\begin{aligned} S(\mathbf{Q})\,\hbar\omega = \frac{2}{3}(&J_r\,\langle \mathbf{S}_{2i}\mathbf{S}_{2i+1}\rangle\,[1-\cos(\mathbf{Q}\cdot\mathbf{r_1})] \\ &+ J_l\,(\langle \mathbf{S}_{2i}\mathbf{S}_{2i+2}\rangle + \langle \mathbf{S}_{2i}\mathbf{S}_{2i+3}\rangle)\,[1-\cos(\mathbf{Q}\cdot\mathbf{d})]). \end{aligned} \tag{5.9}$$

	S_0^z	S_π^z	S_0^+	S_π^+	S_0^-	S_π^-
$\|s\rangle$	0	$\|t^0\rangle$	0	$-\sqrt{2}\,\|t^+\rangle$	0	$\sqrt{2}\,\|t^-\rangle$
$\|t^+\rangle$	$\|t^+\rangle$	0	0	0	$\sqrt{2}\,\|t^0\rangle$	$-\sqrt{2}\,\|s\rangle$
$\|t^0\rangle$	0	$\|s\rangle$	$\sqrt{2}\,\|t^+\rangle$	0	$\sqrt{2}\,\|t^-\rangle$	0
$\|t^-\rangle$	$-\,\|t^-\rangle$	0	$\sqrt{2}\,\|t^0\rangle$	$\sqrt{2}\,\|s\rangle$	0	0
P	+1	-1	+1	-1	+1	-1
ΔM^z	0	0	+1	+1	-1	-1

Table 5.2: Possible excitations for the singlet triplet states in a spin ladder with parity separated scattering channels. The left column contains initial states and the other columns represent the final states. Excitation channels are represented by the structure factor $\mathrm{S}^{\alpha,\beta}_{Q_y}$ where Q_y is the scattering sector (0 or π). The bottom two rows concern the parity of the excitation and the magnetisation. Adapted from reference [7]

The structure factor given in equation 5.9 is a sum of the spin-spin correlations in the ladder weighted by the interaction strength, modulated by the interaction vector.

For the rung interaction, the rung vector for BPCC is given by:

$$\mathbf{r}_{1,2} = [0.3822 \ \pm 0.173 \ 0.4866] \tag{5.10}$$

With a leg vector of [0 0 1]. As a consequence, we can select the **Q** values for maximising the signal of $|s\rangle \rightarrow |t\rangle$ by choosing the channel with the structure factor maximum;

$$1 - \cos\left(\mathbf{Q}\cdot\mathbf{r}\right) = \max \tag{5.11}$$
$$2\pi\left(r(1)\cdot Q_h + r(3)\cdot Q_l\right) = (2n+1)\,\pi$$

Conversely the minimum in the one magnon structure factor corresponds to the maximum intensity of the two magnon channel. As such the Q_l value to select an excitation channel can be written as;

$$Q_l = \frac{\frac{2n+1}{2} + r(1) \cdot Q_h}{r(3)}, \qquad \begin{cases} \text{One magnon } n &= \mathbb{Z} \\ \text{Two magnon } n &= \mathbb{Z} + \frac{1}{2} \end{cases} \tag{5.12}$$

The spin-spin correlations needed for the single mode approximation (equation 5.9) can be easily found through exact diagonalisation. The correlations quickly converge as shown in figure 5.3.

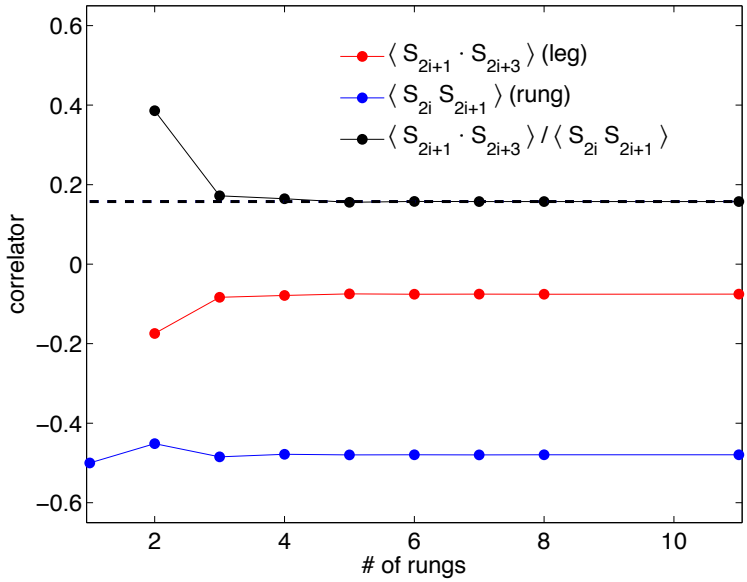

Figure 5.3: Spin-spin correlators for BPCB calculated from exact diagonalization (Lanczos technique). Correlators for the rung are shown in red and the leg in blue. The resulting ratio of 0.1574 is plotted as a black dashed line. Rapid convergence with the system size is observed. Taken from reference [49].

The structure factor of the one magnon excitation from coupled dimers can also be calculated within the Random Phase Approximation (RPA) framework. This technique was originally used on $Cs_3Cr_2Br_9$ [78, 79] and has been applied to BPCB [49]. For BPCB, the 3D representation of the structure factor was derived from the work of $KCuCl_3$ [80] and reads:

$$S_{\pm}^{\alpha,\alpha}(\mathbf{Q},\omega) = \frac{J_r}{\omega_{\pm}(\mathbf{Q})} \left(\frac{1}{2} \sin\left(\frac{\mathbf{Q}\cdot\mathbf{r}_1}{2} \right) \pm \frac{1}{2} \sin\left(\frac{\mathbf{Q}\cdot\mathbf{r}_2}{2} \right) \right)^2 \cdot \delta\left(\hbar\omega - \omega_{\pm}(\mathbf{Q})\right), \tag{5.13}$$

where by varying the sign of $J_{(0\frac{1}{2}\frac{1}{2})}$ and $J_{(1\frac{1}{2}\frac{1}{2})}$ the $\omega_{\pm}(\mathbf{Q})$ dispersion is calculated. The intensity of the two $S^{\alpha,\alpha}_{\pm}(\mathbf{Q},\omega)$ modes are unequal and occur with a π phase shift in reciprocal space.

The ground state of the spin ladder is predominantly singlets, however there is a zero field triplet population due to quantum fluctuations. The ground state triplet density is dependent on γ [81]. The consequence of this is that if there are two dimers on adjacent rungs, an effective exchange can take place lowering the total two magnon excitation energy. These bound two triplet states have an energy ω_{tB} and are generic to gapped dimer systems, though rarely observed. The dispersion of these bound states has been calculated for a spin ladder by the linked cluster series expansion method up to 3rd order in γ in reference [82] and the structure factor has been calculated in reference [83].

$$\begin{aligned}\frac{\omega_{tB}(q)}{J_r} =& 2+\frac{\gamma}{2}(-3-2\cos(\pi\cdot q))+\frac{\gamma^2}{8}(11-2\cos(q)-4\cos(2\pi\cdot q))\\ &+\frac{\gamma^3}{16}(17+9\cos(\pi\cdot q)-8\cos(2\pi\cdot q)-5\cos(3\pi\cdot q))+\mathcal{O}(\gamma^4). \end{aligned} \tag{5.14}$$

The first terms of the expansion has an inverse cosine form and the bound state only exists in an interval given by,

$$q_c < q < 2\pi - q_c \quad \text{with} \quad q_c = \frac{2\pi}{3}-\frac{5\gamma}{2\sqrt{3}}-\frac{109\gamma^2}{48\sqrt{3}}+\mathcal{O}(\gamma^3). \tag{5.15}$$

5.1.4 Comparison with exact diagonalisation

The equations 5.4, 5.5 and table 5.1 can be used to describe the one magnon dispersion, however these models are only valid for a range of γ values. All the equations above are for the strong coupling limit, where $J_r >> J_l$ and as such break down at $J_r \approx J_l$. A common analysis method is to compare these analytical dispersions with one from exact diagonalisation of the Hamiltonian.

The dispersion for a set of γ values has been calculated from the sparse diagonalisation application in the ALPS package [61]. A ladder of length 2x13 spins was diagonalised using Lanczos sparse diagonalisation, whereas reference [70] suggests that a 2x8 spin geometry is a surprisingly good approximation.

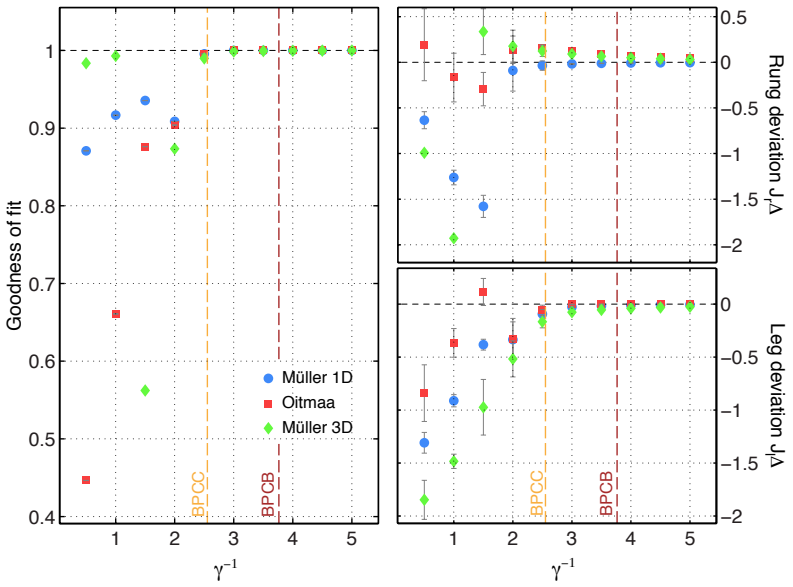

Figure 5.4: Diagonalisation of a 2x13 spin geometry for $0.5 \leq \gamma^{-1} \leq 5$. In the panels blue points show the results from equation 5.5, red points are from table 5.1 and green points are equation 5.6. Left) Goodness of fit from a least-squares fitting to the exact diagonalisation result. Right) The rung (upper) leg (lower) deviation from the values used in the simulation.

From this comparison we see that the 3^{rd} order and the 8^{th} order perturbation expansions are both valid for $\gamma^{-1} > 2$, where as for smaller values of γ^{-1} there is rapid divergence from the exact solution. The 3D dispersion for $TlCuCl_3$ has had all parameters except J_r and J_l set to zero and the resulting fit shows comparable divergence from the exact exchange values.

The spin ladder systems BPCC and BPCB have $\gamma^{-1} = 2.6$ and 3.8 respectively and as such can be described by any of the above models (dashed yellow and red lines). On closer inspection the result of the 1D perturbation treatment yields the most accurate result for the range of exchange ratios. Hence equation 5.5 will be used to describe the experimental dispersion when 3D coupling is not considered.

A comparison for BPCC and BPCB for all models are shown in figure 5.5.

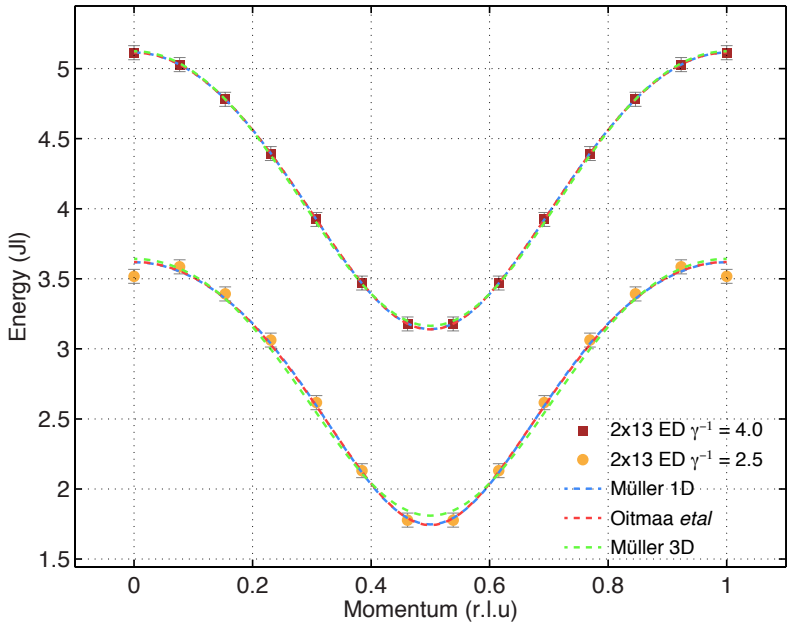

Figure 5.5: One magnon dispersion from exact diagonalisation (Lanczos technique) compared to equations given in the text for exchange ratios close to those of BPCB and BPCC. Filled shapes correspond to 2x13 site simulations and dashed lines correspond to the dispersion calculated with the same exchange parameters as the associated simulations. Where blue is equation 5.5, red is from table 5.1 and green corresponds to the 3D representation of eqaution 5.6.

5.2 Exchange determination for BPCC

The dispersion of BPCC was measured on the triple-axis spectrometer IN14 (ILL - Fr) and on the time-of-flight spectrometer LET (ISIS - UK). The IN14 spectrometer was operated in the W configuration with 60° collimation on the incident beam. Divergence was controlled by slits placed before and after the sample. Higher order scattering was reduced by the application of a cooled Be filter placed after the sample position. The final wavevector was kept constant at $k_f = 1.25$ Å^{-1} and energy scans at various momentum transfers were performed. Optimal vertical focusing of the monochromator and horizontal focusing of the analyser was used. This experiment was performed on a fully deuterated BPCC crystal stack with a total mass of approximately 1.2 g on a copper mount at a base temperature of 50 mK. For the LET experiment, data presented in this section was collected as part initial mea-

surements at zero field, before the investigation into the spin Luttinger-liquid phase. For full experimental details see the primary section in chapter 7. To summarise: the primary incident wavelength of 2.5 meV was selected, with addition incident energies of 1.6 and 4.4 meV also captured by rep rate multiplication. Chopper speeds were optimised for resolution and beam intensity. A fully deuterated sample of approximately 1.6 g on an aluminium mount at a base temperature of 60 mK was used. The experiment was performed in the custom LET 9 T vertical magnet.

5.2.1 Exchange determination by time of flight spectrometry

On LET the primary incident energy of 2.5 meV was selected with a resolution of 33 μeV as determined by chopper frequencies. Multiple data collections with rotations of the sample ω angle (Horace scans) allow for the collection of arcs of data over a range of Q and energy transfers. With $\Delta\omega$ varying between 2 and 5° a fan in Qh and Ql space can be covered. The Q range in figure 5.6a shows an integration signal between 0.19-0.43 meV and along Q_k. The colour map represents the structure factor of the singlet-triplet excitation which occurs in this energy range. The anticipated correlations, extracted from exact diagonalisation using the exchange parameters obtained from susceptibility and the Cu^{2+} rung vector from neutron diffraction in section 4 have been used in equation 5.9 to generate figure 5.6b. By applying the same integration range as the experimental data, the agreement obtained validates the SMA representation of the structure factor (equation 5.9). Both data and simulation show nodes of scattering intensity as expected, rotated by the rung vector.

The data in figure 5.6 can be cut along reciprocal lattice vectors to obtain the dispersion in all planes. Planes of interest are shown as red lines with integration bounds depicted as white lines. The two cuts as indicated by solid lines distinguish the two possible scattering channels $Q_y = 0, \pi$. The possible excitations in these channels are described in table 5.2.

From the crystal structure the primary dispersion is along Q_h. The $Q_y = \pi$ channel represents the gapped one-particle singlet-triplet excitation. The maximum intensity of this excitation is along the structure factor maximum. The Q_l value obtained from an integer n in equation 5.12 and represented as the upper line. The

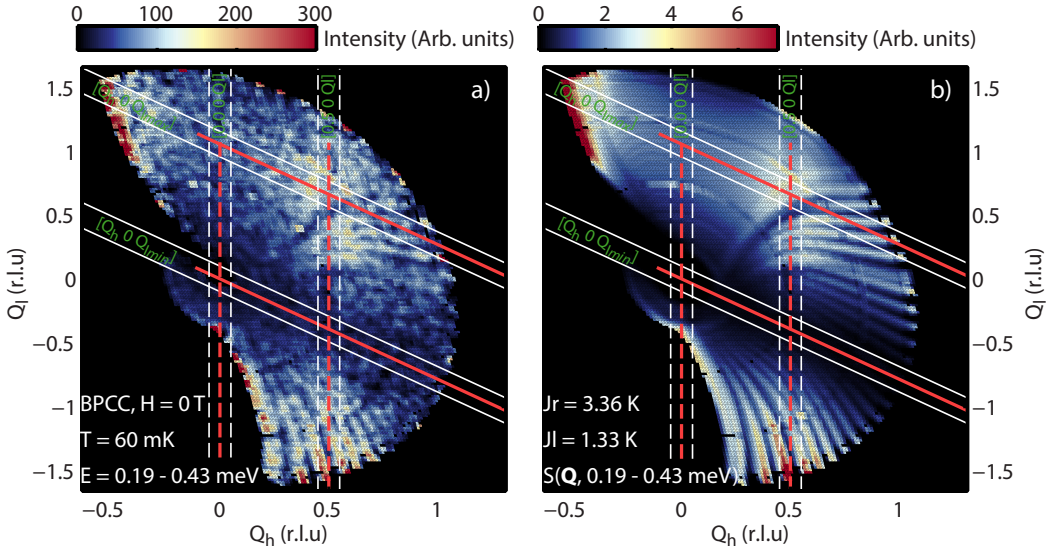

Figure 5.6: Q coverage of scans performed on LET at zero field in the energy range 0.19-0.43meV. The color map a) represents integrated intensity for the singlet-triplet excitation and b) shows a simulation of the data using equation 5.9. For the simulation, exchanges $J_r = 3.36$ K and $J_l = 1.33$ K were used. Red lines represent cuts along vectors of interest and white the corresponding integration range. Solid lines are cuts along the $Q_y = 0,\ \pi$ sectors at maximum intensity, dashed lines are cuts perpendicular to the primary dispersion direction at the band gap and the zone boundary.

$Q_y = 0$ channel of opposite parity represents two-particle excitations and occurs at half integer values of n. Vertical lines correspond to cuts perpendicular to the primary dispersion at the gap and zone boundary.

The $Q_y = \pi$ sector

Figure 5.7 (Top) shows a Q, ω map corresponding to the maximum intensity of the dimer structure factor along the ladder direction at $[Q_h\ 0\ Q_{l\,max}]$. A dispersive mode of periodicity $Q_h = 1$ and varying intensity is observed, with an excitation bandwidth of 0.24meV and gap of 0.19meV. Below the excitation is a Q-dependent contribution from the cryomagnet. Multiple scattering off internal aluminium supports alter the incident neutrons path and time to the detector, which translates

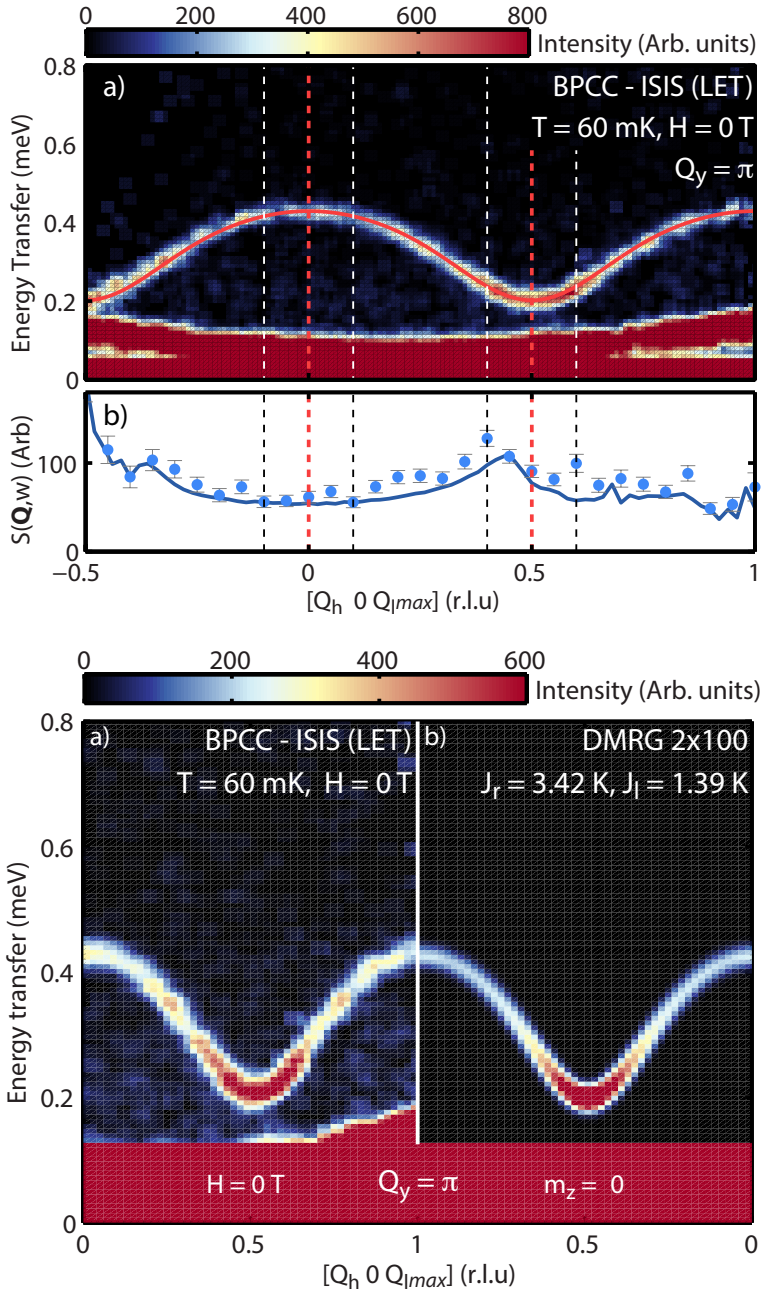

Figure 5.7: Summary of the raw data for the $Q_y = \pi$ sector. Top a) Dispersion in the $Q_y = \pi$ sector where the solid red line represents a fit to equation 5.5. Dashed lines represent cuts perpendicular to the primary dispersion at the zone boundary and spin gap shown in figure 5.9. b) Integrated intensity between 0.19-0.43 meV, the solid line is a fit to equation 5.9. Bottom a) Dispersion in the $Q_y = \pi$ sector, b) DMRG simulation of the zero field dispersion, integrated over the same range.

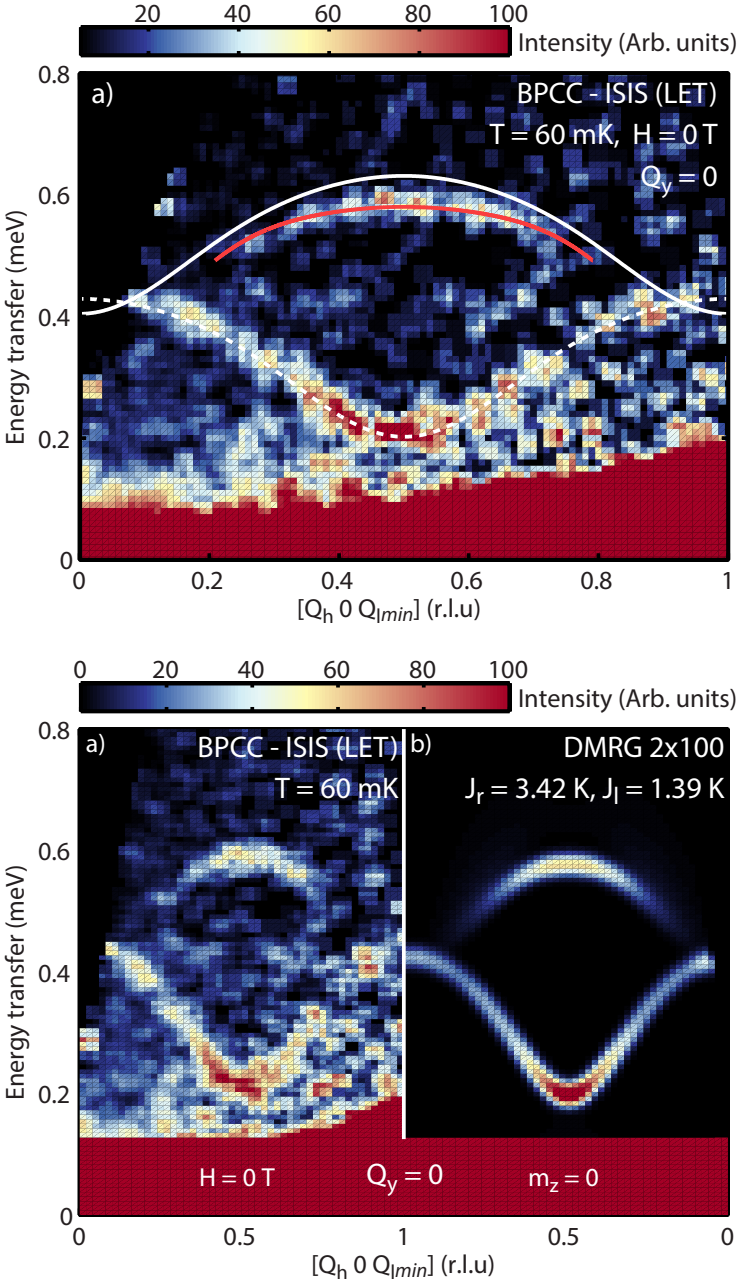

Figure 5.8: Summary of the raw data for the $Q_y = 0$ sector. Top) Dispersion in the $Q_y = 0$ sector. Dashed white line corresponds to the $Q_y = \pi$ dispersion, the remnants of which are visible due to integration width. The lower boundary of the two particle continuum is shown as a solid white line and the location of bound states from equation 5.14 is shown in red. Bottom a) Dispersion in the $Q_y = 0$ sector, b) DMRG simulation of the $Q_y = 0$ sector with the same integration range.

into a Q-dependent inelastic signal. For subtraction, the peak profile of this signal can be modelled with two Gaussian line shapes. The energy transfer of the observed spin gap is greater than that of the erroneous signal from the magnet, so removal has not been performed. The primary dispersion and excitation intensity has been determined by simultaneously fitting all available data. The dispersion by Müller *et al.* has been selected due to its validity over a wide range of exchange ratios and the structure factor is described by the SMA approximation of equation 5.9. The following set of exchange parameters accurately describe the singlet-triplet dispersion and are consistent with those found by susceptibility,

$$\mathrm{J}_r = 3.36(9)\ \mathrm{K}, \qquad \mathrm{J}_l = 1.34(1)\ \mathrm{K}. \tag{5.16}$$

Numerical stimulations of the dynamical correlations have been performed by P. Bouillot (University of Geneva) with parameters $\mathrm{J}_r = 3.42$ K, $\mathrm{J}_l = 1.39$ K. The determination of these exchange parameters is described in subsection 5.2.3, further details about the analysis technique is in section 7. The experimental data is shown for one period in figure 5.7 (Bottom - a) along with the resulting simulation b). The dynamical correlations $\mathrm{S}^{\alpha,\beta}_{Q_y}$ $(\alpha, \beta = x, y, z)$ have been summed with appropriate weight, convolved with instrumental resolution and the same cut as for the data has been performed. Scaling of the intensity to the experimental value at the band gap has been applied. The experimental data is not in absolute units. The excitation energies and intensities show remarkable agreement with the experimental data. Slight differences between the two can be attributed to non-universality of exchange parameters between different numerical techniques and resolution effects.

The $\mathbf{Q}_y = 0$ sector

The two triplet $\mathrm{Q}_y = 0$ channel contains more complex multi-triplet excitations, as summarised in table 5.2 and figure 5.8. The two distinct features are the two particle continuum and a region supporting bound triplet states. Both of these can be easily identified in the DMRG calculations in section 5.3. The data can be cut along the vector corresponding to the $\mathrm{Q}_y = 0$ channel, however any excitations are expected to be much weaker than that of the single particle sector. Using the results from Normand *et al.* [81] we can estimate that the ground state triplet population is

$\approx 5\%$ and hence scattering should scale accordingly. The approximate nature of this value is due to the limited validity of the bond operator theory for small coupling ratios (γ^{-1}). In figure 5.8 a cut along $Q_y = 0$ is presented, with an integration width in Q_l of ± 0.1 meV. The remains of the singlet triplet excitation are visible (denoted by the dashed white line), indicating that the integration range is too wide to adequately separate the two channels. Smaller integration widths lead to poor unusable statistics. The red line corresponds to the position of bound states using equation 5.14. A sharp mode of limited intensity is visible, decaying as it approaches the maximum theoretical extent. The two particle continuum, the lower boundary of which is denoted by the solid white line is not visible due to low probability of a double triplet excitations. This is demonstrated further in the comparison with the DMRG calculations. Bottom a) of figure 5.8 contains the same data as previously shown; Bottom b) the same cut is applied to the DMRG simulation. In this cut the contribution from the one-particle sector is also visible along with the bound state mode. Careful observation at $Q_h = 0.25,\ 0.75$ shows the slightest broadening in the simulation due to the strongest part of the two particle continuum. However, the low spectral weight for these Q values means that it will not be distinguishable from the background in the experimental data.

Perpendicular to the ladder direction

The singlet-triplet exchange perpendicular to the ladder direction can show evidence of inter-ladder couplings. Oscillatory deviations from a flat band are indicative of these couplings and the 3D dispersion relation for $TlCuCl_3$ (equation 5.6) can be used. The sample was mounted in the a-c scattering plane, allowing access to inter-ladder dispersion along the Q_l direction. As shown in figure 5.6 a large extent of Q_h, Q_l space is available for performing cuts.

A cut at [0.5 0 Q_l] shows the dispersion perpendicular to the band gap and is shown as figure 5.9 (Top). In panel 5.9 (Top - a) the excitation is flat at 0.19 meV, does not oscillate as a function of Q and is shown by a red horizontal line. The flat line corresponds to the mode being dispersionless within experimental error, which is approximately 6 μeV or 0.07 K. The total corresponding inter-ladder exchange energy would as such be in the mK range. The intensity of the mode strongly varies

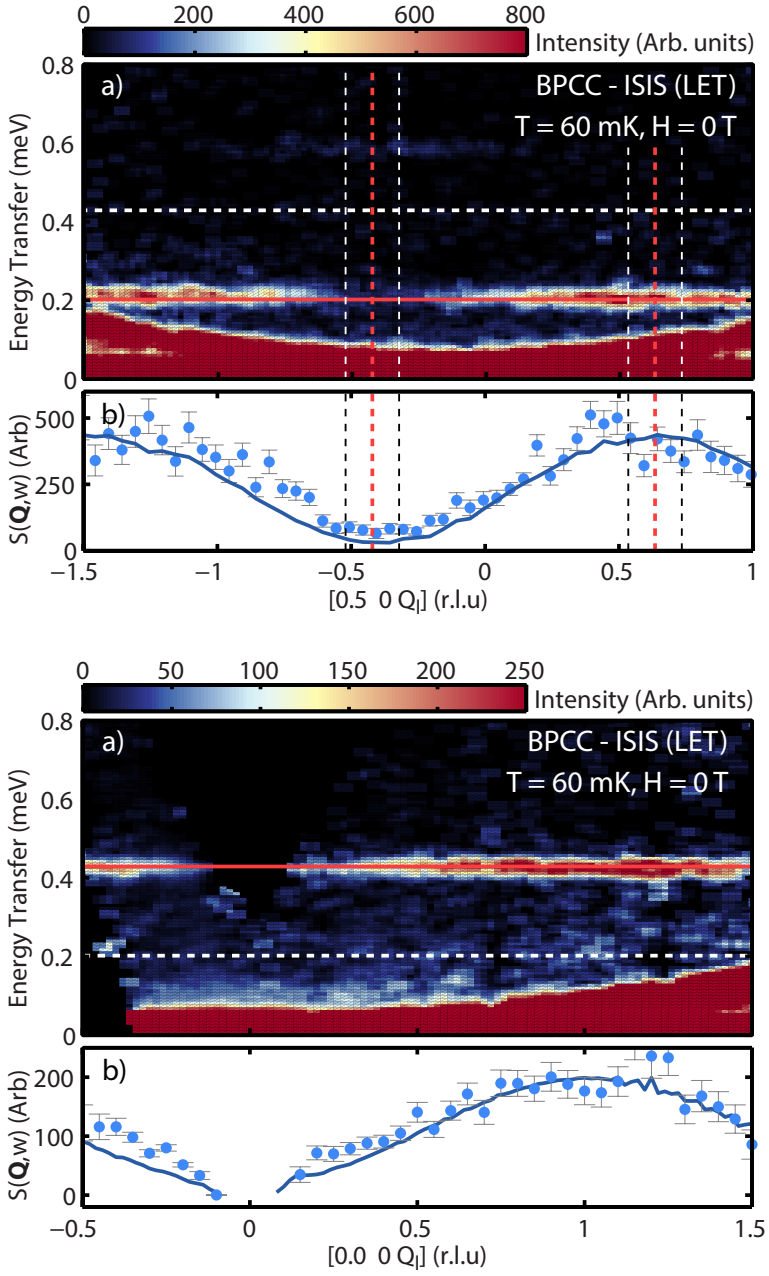

Figure 5.9: Excitation perpendicular to the ladder direction at the band gap and zone boundary. Top a) Q_l, energy map perpendicular to the ladder direction at the band gap. Bottom a) energy map perpendicular to the ladder direction at the zone boundary. Solid lines horizontal lines correspond to the non-dispersive excitation and dashed lines outlines the excitation bandwidth. b) for both panels shows the integrated intensity of the excitation.

over the inspected Q_l region, as shown in figure 5.9 (Top - b). Over plotted as dashed lines are the locations in Q_l corresponding to the different Q_y sectors at $Q_h = 0.5$. The $Q_y = 0$ sector corresponds to the minimum intensity of the singlet-triplet mode and shows the signal captured by the integration range. At 0.6 meV the weak bound state mode is visible, decaying strongly from the maximum point. The $Q_y = \pi$ is also shown, corresponding to the maximum spectral intensity. Overall the agreement with the calculated and observed magnetic structure factor is excellent. At low values of Q_l statistics limit the agreement, which is to be expected.

Cutting the data at the zone boundary [0.0 0 Q_l] allows for confirmation of the inter-ladder exchange. This cut shown in 5.9 (Bottom) also does not show any oscillatory behaviour, the excitation is non-dispersive at 0.43 meV. The data in this cut is of lower statistics than the previous [0.5 0 Q_l] cut and the excitation is missing near $Q_l = 0$ but the structure factor agreement is impressive.

In TOF spectroscopy the 4D dataset also includes out-of-scattering-plane data. The long b-axis of BPCC corresponds to a short reciprocal lattice axis, an advantage which is limited by vertical detector angle. Converting to reciprocal space the maximum coverage in Q_k was found to be $\pm 0.2 Q_k$. Poor Q_k coverage and limited statistics create experimental conditions where the dispersion in this direction can't be accurately determined. A similar behaviour to the Q_l direction is expected due to the extremely weak inter-ladder exchange across the ($C_5H_{12}N$) molecule.

5.2.2 Exchange determination by triple axis spectroscopy

The triple axis spectrometer IN14 (ILL-Grenoble) with an experimental setup detailed at the start of the chapter was used to confirm the spin ladder Hamiltonian and exchange parameters for BPCC. Energy scans between 0 and 0.8 meV and at constant Q were performed for values $0.8 < Q_h < 1.8$. For this experiment the Q_l component was set to 0 as the rung vector was unknown at the time of the experiment.

As with the data from LET, a single gapped mode of period $Q_h = 1$ is observed, with a gap of 0.20 meV and bandwidth 0.23 meV. The ladder exchange parameters have been determined by simultaneously convolving the experimental resolution ellipsoid at each scan point with the energy and intensity profile described by equa-

tions 5.5 and 5.9. Using this method and allowing for slight variation in energy we obtain the excitation energies and corresponding exchange parameters. Panel a) of figure 5.10 shows the extracted excitation energies as blue points and a solid line representing the dispersion for the extracted exchange parameters:

$$\mathrm{J}_r = 3.40(2)\ \mathrm{K},\ \ \mathrm{J}_l = 1.31(3)\ \mathrm{K} \tag{5.17}$$

The effect of experiential resolution is shown in panel a) and the energy dependence of the convolved excitation in b) for scans at $\mathrm{Q}_h = 1$, 1.25 and 1.5. The excitation width is determined by the resolution ellipsoid and the ellipsoid volume contributes to the integrated intensity. The integrated intensity in figure 5.10 panel c) has been corrected for resolution volume and shows good agreement with the 1D dimer model of equation 5.9.

The excitation energies and structure factor agree with the measurement performed on the time-of-flight spectrometer LET.

5.2.3 Alternative exchange determination

An alternative method for extracting exchange iterations is to study the field induced ferromagnetic phase. For fields above the saturation field H_s the lowest energy state is that of a fully saturated ferromagnet with spins aligned parallel to the applied field. Excitations in the ferromagnetic phase can be considered as purely classical spin waves where all quantum fluctuations have been quenched. The excitations in the ferromagnetic phase are described purely by triplets where the lowest energy state $|t^+\rangle$ transitions to the singlet and other triplet states. Excitations in the $Q_y = \pi$ sector occur from the excitation of the $|t^+\rangle$ triplet to the $|s\rangle$ singlet state. The spin gap E_{g^s} of this excitation is purely determined by the relative field above H_s and increases linearly with applied field. The same is true for the excitations involving $\left|t^0\right\rangle$ and $|t^-\rangle$. The dispersion of these modes from a mean field treatment are given by [84]:

$$\begin{aligned} w_{t^+\to s}\left(\mathbf{Q}\right) =& g\mu_B H_{rel} + J_l\left(1+\cos\left(2\pi\mathbf{Q}\right)\right) \\ w_{t^+\to t^0}\left(\mathbf{Q}\right) =& 2\cdot g\mu_B H_{rel} + J_l\left(1+\cos\left(2\pi\mathbf{Q}\right)\right) \end{aligned} \tag{5.18}$$

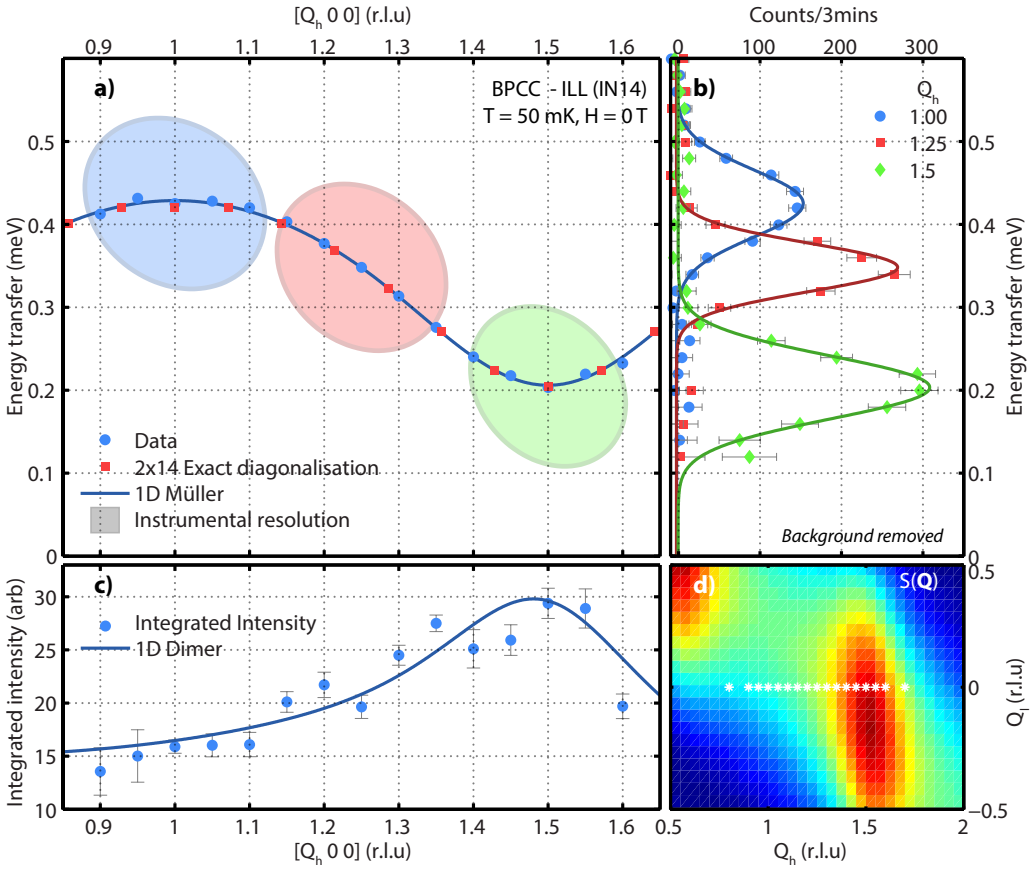

Figure 5.10: Dispersion of BPCC parallel to the ladder direction as measured on the triple axis spectrometer IN14 (ILL). a) Excitation energies after corrections for instrumental resolution (blue points) and dispersion based on the extracted exchange parameters $J_r = 3.40(2)$ K, $J_l = 1.31(3)$ K (blue line). Projections of resolution ellipsoids at various points of the dispersion are shown as shaded ovals. Points from exact diagonalisation simulation with $J_r = 3.42$ K, $J_l = 1.34$ are shown as red points. b) Energy scans at $Q_h = 1.00$, 1.25, 1.50 and the best fit to a resolution convolved Gaussian. c) Q dependence of resolution corrected integrated spectral intensity and the expected spectral intensity from equation 5.9. d) Measured points in reciprocal space and the calculated structure factor.

Where the relative field (H_{rel}) is the energy of the applied field minus the sum of exchanges needed to polarise a triplet,

$$H_{rel} = H - \frac{J_r + 2 \cdot J_l}{g\mu_B} \tag{5.19}$$

By simultaneously fitting of equations 5.18 to the $Q_y = 0$ and $Q_y = \pi$ sectors and the spin gap by 5.19 the g-factor and exchange parameters J_r and J_l can be independently determined. Since the dispersion perpendicular to the ladder is below the detection limit additional inter-ladder exchange interactions have been neglected. Since the crystal is mounted in the a-c plane and a vertical field applied, the g-factor along the b-axis is measured (g_b) rather than the rotationally averaged g. An additional check of this g-factor is possible by checking the field-dependent excitation energies in the Luttinger Liquid phase as described in section 7.2. The possibility of Dzyaloshinskii-Moriya (DM) interactions on the ladder bonds exist, however limited theoretical predictions on it's effect on the dispersion have been published (see reference [85]).

$$J_r = 3.41(1)\ \text{K}, \qquad J_l = 1.387(7)\ \text{K}, \qquad g_b = 2.256(3). \tag{5.20}$$

The exchange parameters above are consistent with those obtained in the quantum disordered phase by both Time-of-Flight and Triple-axis spectroscopy. The obtained g-factor of 2.25 is high for a Cu^{2+} magnetic ion, where values typically vary between 2 and 2.2. In BPCB it has been reported by ESR that values as high as 2.29 [22, 18] exist, which puts the $BPCBC_x$ series as an exception to the general rule. Using these values the two critical fields H_c and H_s can be deduced. From equation 5.5 the critical field is $H_c = 1.56(1)$ T and the saturation field, given by equation 5.19 is $H_s = 4.08(3)$ T.

5.3 Conclusions

Thanks to the variety of theoretical tools available, the quantum disordered phase of a strong-leg spin ladder system can be fully analysed. With complete access to the neutron scattering cross section, experiments can accurately determine the magnetic exchange parameters and correlations present in such a system. For BPCC

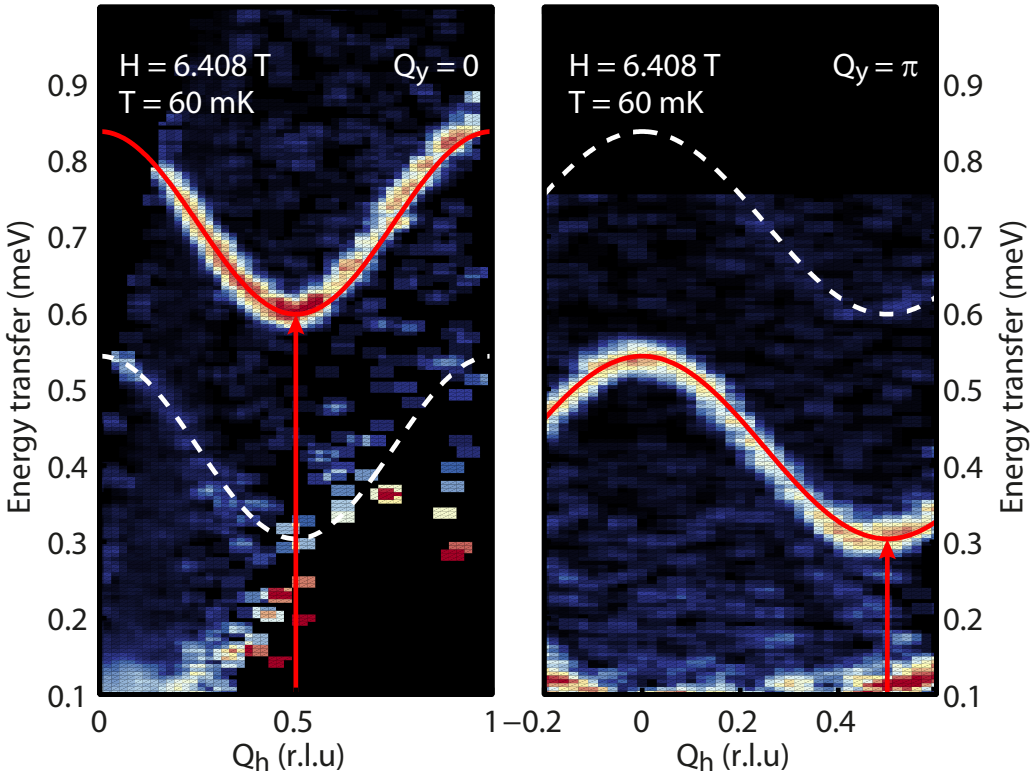

Figure 5.11: Dispersion of BPCC in the ferromagnetic phase. Fits to the dispersion in the separate Q_y sectors are given by equation 5.18 where the spin gap is purely dependent on the sum of exchange parameters and the applied field as described by equation 5.19 for $J_r = 3.41$ K, $J_l = 1.387$ K and a g-factor of 2.25.

the dispersion, both parallel and perpendicular to the ladder direction has been measured. The material is an excellent realisation of a pure ladder spin ladder Hamiltonian defined by J_r and J_l. The J_r and J_l exchange parameters as determined by three different methods are summarised in table 5.3.

	J_r (K)	J_l (K)	g_b	Reference
QD - TOF	3.36 (9)	1.34 (1)		5.16
QD - TAS	3.40 (2)	1.31 (3)		5.17
FM - TOF	3.41 (1)	1.39 (1)	2.26 (1)	5.20
χ	3.5 (2)	1.4 (3)		4.5
Mean	3.4 (2)	1.4 (3)		
Weighted mean	**3.41 (1)**	**1.39 (1)**		

Table 5.3: Summary of exchange parameters in BPCC from inelastic neutron scattering and magnetic susceptibility measurements.

The extracted exchange parameters are confirmed to be consistent within errors. Studies of the quantum disordered phase rely on the validity of equation 5.5 which has been confirmed for the extracted exchange ratio. Exchange determination by examining classical spin waves in the field-induced ferromagnetic phase provides a reliable confirmation. Here the main source of error is arguably from the uncertainty in determining the relative applied field. Due to the well known classical nature of ferromagnetic spin waves the associated exchange parameters are the most accurate estimate. Numerical simulations by DMRG validate the observed one and two particle excitation spectra, where exchange parameters $J_r = 3.42$ K, $J_l = 1.39$ K were used as the only input parameters. The direct comparison with the experimental data can be seen in figures 5.8 and 5.7 and both sectors without integration normalisation are also presented in figure 5.12. Additional inter-ladder exchange has been limited to 0.07 K and as such is orders of magnitude smaller the other dominant terms.

Using all available inelastic neutron scattering and susceptibility data results in

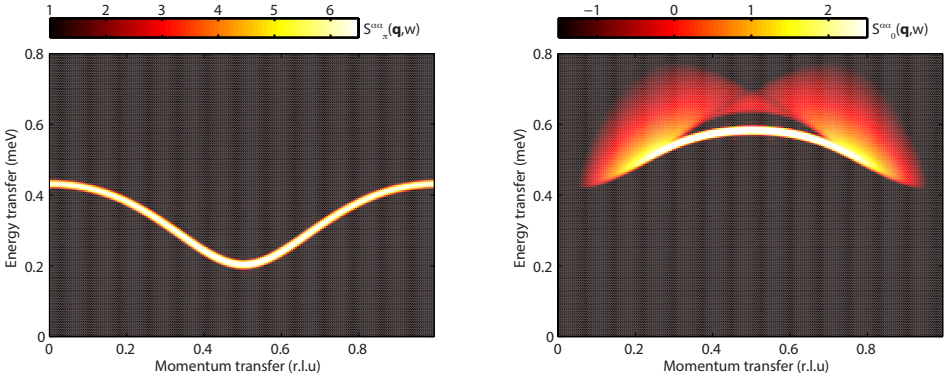

Figure 5.12: One magnon (left) and two magnon excitations in BPCC as calculated from DMRG with initial parameters described in the text. Logarithmic scaling has been used to highlight the two particle continuum.

the final set of exchange parameters for BPCC:

$$\mathrm{J}_r = 3.41\ (1)\ \mathrm{K}, \qquad \mathrm{J}_l = 1.39\ (1)\ \mathrm{K}, \qquad \mathrm{J}' \leqslant 0.07\ (1)\ \mathrm{K} \tag{5.21}$$

The exchange ratio for BPCB is 3.8 and for BPCC the calculated exchange parameters give an exchange ratio of 2.5. This corresponds to an ideal realisation of a spin ladder in the strong coupling limit. When compared to BPCB there will be a higher density of triplet excitations in the ground state [60] and hence more intensity in the two particle continuum. The exchange parameters are also lower than that of BPCB and as such, the dispersion is at a lower energy and reduced bandwidth. This corresponds to easily accessible field induced critical points, which are advantageous for neutron scattering. BPCC can be considered as a new prototypical spin ladder and excellent material to test spin Luttinger-liquid physics and other exotic phenomena of one dimensional systems.

Chapter 6

Excitations in a spin ladder with randomised exchange

Contents

One possible modification to spin ladders without effecting the spin exchange geometry is to introduce random exchange interactions. Random exchange interactions allow for the realisation of novel phases and spin dynamics, where there are scarce experimental results to compare to theoretical predictions.

There has been theoretical work on localised states in the band gap [86] and observations of inter-gap localized states in semiconductor materials [87]. Reduced magnon lifetimes [88] and spin gap instability [89, 90] have been reported in quantum magnets.

The proposed Hamiltonian of the spin ladder with random exchange is analogous to the pure case (equation 5.1) except the rung and leg exchange parameters are site dependent and their value depends on the probability distribution characterising the site disorder:

$$\mathcal{H} = \sum_{i=1}^{L} J_r\left(x\right)_i \mathbf{S}_{i,1} \cdot \mathbf{S}_{i,2} + \sum_{j=1,2} \sum_{i=1}^{L-1} J_l\left(x\right)_{(i,j)} \mathbf{S}_{i,j} \cdot, \mathbf{S}_{i+1,j} - g\mu_B h^z, \tag{6.1}$$

where for a given value of disorder x, the exchanges J_r and J_l can take a set of values which are drawn from the probability distributions $p_1(x)$ and $p_2(x)$. At $h^z = 0$ we can consider the system to be an ideal ladder where a varying random potential has been applied. To understand the general behaviour of the bond randomised ladder, we will consider the phenomenological effects of adding disorder on both the dynamics and the bulk properties of the system.

6.1 Disorder and randomisation

Disorder in low dimensional quantum magnets has been realised by magnetic impurities, temperature induced defects and chemical disorder. By reference to the local and bulk effects of these types of disorder in real systems connections to $BPCBC_{0.1}$ can be deduced.

Bulk affects of substitution

As shown in section 5.1.1, the ratio of exchange interaction in spin ladders can drastically change the shape of the one magnon dispersion. Here we will first consider what happens when the randomised sections of ladder with equal exchange parameters correlate. Coherent excitations are possible if the coherence length is greater than the spacial separation between affected rungs.

Since BPCC has exchange interactions lower in energy when compared to BPCB, it is conceivable that for mixed systems $BPCBC_x$ locally the rung and leg exchange will also be reduced. First we consider a reduction of the leg exchange whilst the rung is kept constant. This is schematically represented in figure 6.1 (Left) with the use of equation 5.5[a]. We find that the reduction in the leg exchange lowers the excitation bandwidth. They become a flat mode when $J_l = 0$. Conversely, for the case of a reduction in J_r as shown in 6.1 (Right). The dispersion is shown to evolve with a characteristic shape as γ is reduced, before reaching the chain limit.

We stay with the assumption that in the disordered system sections with uniform, unmodified exchange parameters form. If this is the case then additional broad excitations will be present in the ladder spectra. If the rung exchange is primarily

[a] The same restrictions apply as described in section 5.1.4 are present here.

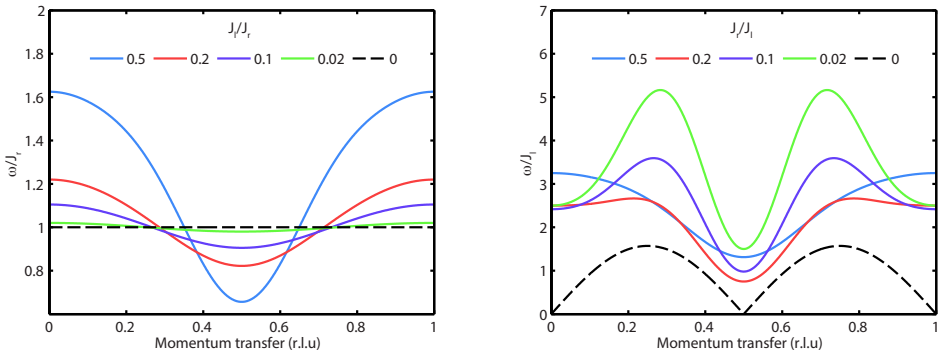

(i) (ii)

Figure 6.1: Affect of exchange ratio on the ladder dispersion. Left) Dispersion for values of γ approaching ∞ where solid coloured lines are different coupling ratios and the dashed line is the isolated dimer limit. Right) Dispersion for γ approaching 0. The dispersion remains gapless for finite values of γ (solid coloured lines) and becomes gapless at $\gamma = 0$, the spin chain limit.

affected, the signature would be an additional mode with a lower energy at the zone boundary and modified gap energy. For the leg case the new mode would be tending towards being non-dispersive. Unless the triplets are highly correlated the corresponding excitations will be broadened because of finite section length.

Local affects of substitution

First we consider a pure ladder with dilute, weak rung exchange interactions ($J_{r'} < J_r$), so that the spacial separation of these is greater than the coherence length of excitations. In the limiting case $J_{r'}/J_r = 0$ the exchange is removed and two local moments are liberated. These moments interact antiferromagnetically and screen each other [91]. The resulting singlet has an effective $J_r^{eff} < J_r$. There has been debate over the sign of J_r^{eff}, with reports of magnetic impurity doping creating an effective ferromagnetic exchange [92].

Extending this argument to finite $J_{r'}$ we can consider $J_{r'}$ to be analogous to J_r^{eff}, which holds for the case $0 \leq J_{r'}/J_r \leq 1$. The affect of random bond disorder in even-leg spin ladder systems has been discussed in reference [93] by analogy to bond energies. It is found that this interpretation is correct. The rung bond energy

is significantly reduced and the bond energies of the connecting legs increase. The case of leg disorder is also covered, whereby one reduced leg exchange increases the opposite legs bond energy and enhances the nearest rung bond energies. There are twice as many leg bonds as rung bonds in the spin ladder geometry so the affects of leg dilution are expected to be dominant. The implications from the modification of bond energies indicate that the bond operator approach introduced in reference [60] might be applicable to the bond disordered case.

The affect on the dispersion for the rung and leg disorder cases above is to introduce localisation and lower the spin gap of the system. From a modification of equation 5.9 the new set of bond energies will have the affect of modifying the excitation intensities and shifting spectral weight. The localised triplets will manifest in a broad non-dispersive excitation. The ladder component will have additional width due to the excitation having a reduced lifetime. The lifetime of the excitation is limited due to scattering off of the localised states. This has been observed in a Cl substituted quasi-2D quantum magnet PHCC [88] through the intrinsic excitation width and comparisons with the density of state (figure 6.2).

Correlation lengths

The correlation lengths of an even-leg bond disordered spin ladder system have been studied in reference [94]. It was previously stated that leg dilution will be the dominant effect on the system. The effect of which will be to locally preserve the spin gap, leading to short-range correlations. For a pure system the correlations decay exponentially due to the spin gap. For the bond diluted case it has been found through QMC simulations that the correlation length at low values of disorder stays equal to that of the pure case. The correlation length slowly increases with the concentration of diluted bonds until 22% of bonds are diluted (see figure 6.3). After this point the correlation length starts to be reduce. In the simulation units this maximum in the correlation length occurs at the length of the ladder segments. It is argued that the correlation length at low bond dilutions is determined by the competition between the correlation enhancement through rung-bond dilution and the correlation suppression due to ladder fragmentation.

Figure 6.2: Density of state for the quasi-2D quantum magnet PHCC which has been doped with 3.5 and 7.5% Br. Excitation width shown in solid points is comparable to the calculated density of states which is shown as a shaded area. This comparison implies that the finite magnon lifetime arises from scattering of magnon impurities. Taken from reference [88]

Figure 6.3: Correlation length (ξ) Vs bond randomisation (z) for even leg ladders as computed by QMC. The red simulation points correspond to a 2 leg spin ladder, where green and red are for 4 and 6 legs. In all cases the correlation length is increased until it reaches 22% bond randomisation. Taken from reference [94]

Temperature affects

When we consider local affects of substitution it has been found that the excitations linewidth increases by scattering with impurities. Another type of impurity is temperature induced states, which may act as defects and can cause asymmetric affects on the excitation line shape. There have been a few examples of this in low dimensional systems.

One example of temperature induced affective impurities is the anomalous line shape of the S = 1/2 one-dimensional bond alternating Heisenberg chain copper nitrate by Tennant *et al.* [95]. At low temperatures both one and two magnon excitations occur. On increasing temperature the two magnon continuum is reduced and the one magnon excitation acquires an anomalous line shape. This is due to the neutron-excited magnon interacting with the nearby thermally activated magnons through the potential V and scatters to a two-magnon final state via an off-shell scattering process [95]. The line shape was analysed using a Lorentzian line shape modified by a polynomial parametrising antisymmetric dampening.

Another material which exhibits an asymmetric excitation line shape is the gapped 3D antiferromagnet Rb_2MnF_4. Similarly to copper nitrate, a magnon created by the neutron scattering process and thermal magnons undergo repulsion due to a hard-core constraint. As a result the observed dispersion relation and line shape are broadened predominantly in the direction of the highest density of states. [96].

In BPCB experiments on the lifetime of one magnon excitations have been performed for the thesis of B. Thielemann [49]. It has been found that above 6 K the line shape of the one magnon excitation becomes asymmetric. The line shape of the excitation can be described by the work of reference [97] which is complimentary to the work of Tenneant *et al.* .

Work on the temperature dependence of excitation energy, lifetime and intensity have been performed on spin ladder systems. For BPCB a full analysis is in reference citeThielemann:2009th. The temperature effects on other spin ladder compounds with bond disorder have been studied, such as IPA-$Cu(Cl_{1-x}Br_x)_3$ in reference [98] and PHCC [88]. In all cases the temperature dependence has been described by a RPA approximation, which is detailed in references [99, 100, 101] along with other materials which exhibit temperature affects.

Theoretical expectations for a 2D system

Excitations in bond disordered quantum magnets are an emerging field, where few papers have been published. As far as the author is aware, there is only one paper which deals specifically with the case of the excitation spectra of bond disordered quantum magnets.

The work of Vojta in reference [102] examines the case of bond disorder on a bi-layer 2D Heisenberg quantum magnet near quantum criticality. Bond disorder was of the random-mass type and affected the interlayer coupling K. This led to two exchanges K_1 and K_2 with probabilities p and 1-p respectively. Bond operator theory and an appropriate mapping was used to solve this problem. The results for various exchange ratios (in-plane and out of plane exchanges) and bond disorder are summarised below and an example of a disordered dispersion is shown in figure 6.4.

- Low values of p
  - Spectral weight shifts to lower energies.
  - States in the band gap are formed, centring around the ordering wavevector.
  - Inter-gap states are localised.
- Intermediate values of p
  - The spectrum separates into two modes, existing throughout the Brillouin zone.

For low p the shift in spectral weight to lower energies is due to the lowering of bond energies by J_1. The low energy states at band gap correspond to triplets which have been directly effected by the exchange J_1, creating a localised mode around the spin gap. For larger values of p the excitation splits, corresponding to sections with exchange parameters J_1 and J_2. This is summarised in figure 6.4 for low p.

We can summarise that a the disordered system is still gapped, with localised states in the gap. The dispersion has become broad and away from the ordering wavevector the excitation is asymmetric to lower energies as can be seen at the (π,0) point in figure 6.4.

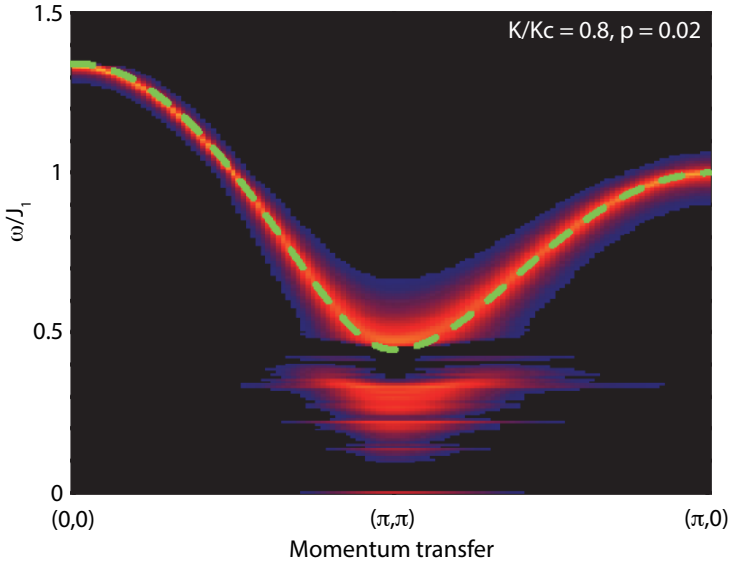

Figure 6.4: Excitation spectra of a 2D Heisenberg bi-layer with bimodal randomness on the interplane exchange. This spectra has been calculated for $K_1 = 0.88\ K_c$ and $p = 0.02$, where the clean case is shown by a dashed green line. The spectral weight has shifted to lower energies and sub-states have formed in the gap.[102]

Disorder and phase transitions

The effects of disorder are not limited to the quantum disordered phase as the consequences extend throughout the entire phase diagram. Of particular note is the effect on the 3D ordered phase. The 3D order of the lowest energy magnons has been referred to as a Bose Einstein condensate [103], sharing many of the same characteristics with the Bose gas counterpart.

A new phase is predicted to emerge when disorder is introduced, this is called the Bose glass phase [104, 105]. Disorder can take the form of random exchanges, leading to localisation of magnons which moves away from the clean dispersive limit.

In the presence of weak disorder the magnons are spatially separated and Anderson localised [106]; their repulsion and absence of overlap prevents condensation from occurring. These spins are frozen, hence the glass analogy, the influence of which decays with an Litshitz tail. For the case of strong disorder the spin states overlap and order despite the repulsive effect.

A Bose glass is characterised as a gapless compressible bosonic insulator. Apart from finite magnetisation below the quantum critical point there is a marked change in the ordering parameter, Luttinger parameters and free energy. The phenomena of the Bose glass phase is not limited to one dimension, evidence has been experimentally provided in the two dimensional material DTN [107] and theoretically in three dimensions [108], with experiments that have taken place on cold atomic gases [109].

A review of the current state of work on the Bose glass phase in quantum magnets can be found in reference [110]. For this thesis work on the Bose glass phase will not be incorporated as the story is ongoing.

6.2 Excitations in $BPCBC_{0.1}$

6.2.1 Experimental details

The excitations of the weakly bond-disordered spin ladder material $BPCBC_{0.1}$ was measured on the triple-axis spectrometer IN14 (ILL-Grenoble). A total of 14 crystals were co-aligned in the ac plane to form a sample with total mass of approximately 1.3 g. A copper sample mount and dilution insert were used in conjunction with a 15 T vertical field cryo-magnet. The instrument was operated in the W configuration with a fixed final wavevector of $k_f = 1.4$ Å^{-1}. Both monochromater and analyser were set to optimal focusing and slits were optimised for sample size and background. A Be filter was employed after the sample position to remove higher-order contributions.

Energy scans at constant momentum were performed at the anticipated structure factor maximum along the ladder direction. The structure factor for BPCB was used as an approximation for that of $BPCBC_{0.1}$ as there is only a very small shift in lattice parameters and rung vector between the two compounds. Scans were performed at regular intervals along the $\left[\mathrm{Q}_h\ 0\ \mathrm{Q}_{l_{max}}\right]$ direction and background subtracted data is shown in figure 6.5 together with corresponding data from BPCB and BPCC.

In figure 6.5 (Left) energy scans at the spin gap are presented. Both BPCB and BPCC show sharp excitations with widths limited by experimental resolution. $BPCBC_{0.1}$ shows a broad excitation with a width greater than resolution and asym-

metric line shape, with a tail extending from the peak position to higher energies. Most spectral weight is centred around 0.6 meV and extends up to 1.25 meV.

In figure 6.5 (Middle) the extracted dispersion is presented, where reference compounds are shown for comparison. The excitation has a Q_h-periodicity of 1 and is observed between 0.6 and 1.4 meV. Approaching the zone boundary the excitations energy approaches that of the pure Br compound.

In figure 6.5 (Right), energy scans at zone boundary ($Q_h = 1$) show a sharp excitation at 1.4 meV with additional spectral weight as a tail extending down to 0.8 meV. A sharp spurion at 0.5 meV has been partly removed, where the remnants are still visible at 0.7 meV and will be neglected in the future analysis.

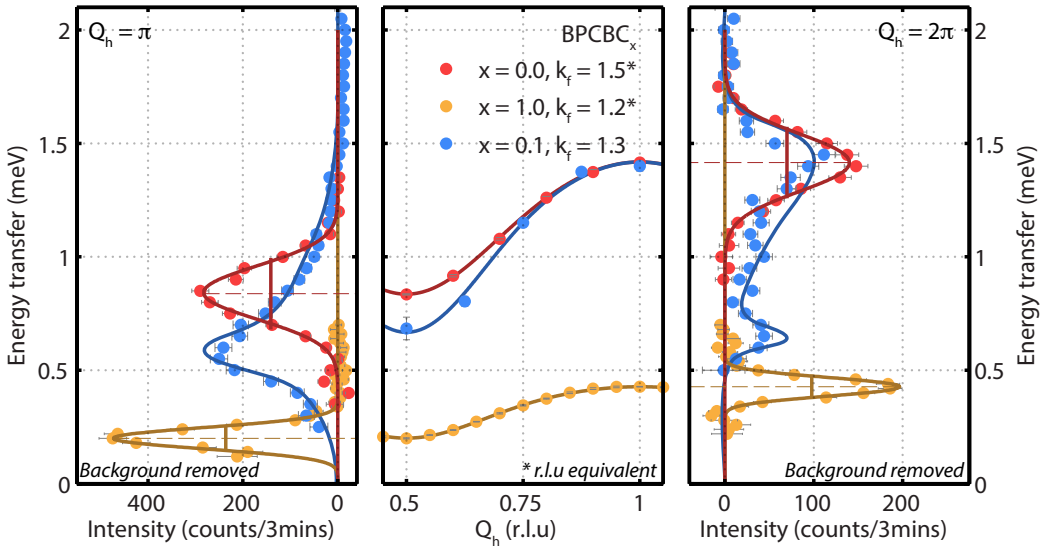

Figure 6.5: Dispersion and energy scans for BPCB, $BPCBC_{0.1}$ and BPCC. In all panels BPCB is represented by red, BPCC yellow and $BPCBC_{0.1}$ by blue points. Left) Energy scan performed at the spin gap are shown where excitation intensity has been normalised to resolution volume and sample mass. Solid lines are from a resolution convolved Gaussian for the pure cases and the technique described by the skew Gaussian model described in section 6.3. Centre) Excitation energies for half a Brillouin zone. Right) Energy scans at the zone boundary.

6.3 Modelling

The line shape of the excitations in $BPCBC_{0.1}$ deviates from the single-mode Gaussian used for both pure compounds. The skewed line shape leads to various possible analysis methods, described are possible methods which have been attempted and their benefits. Firstly, a two mode approximation will be discussed, followed by a statistical multi-mode description and lastly a variation of the single-mode Gaussian.

Two mode approximation

The two mode approximation is an attempt to parametrise the asymmetric nature of the observed excitation. In this approximation one Gaussian represents the dominant excitation where one exists and another broader Gaussian represents the additional spectral weight corresponding to the tail of the excitation. Excitation energies can be determined from the centre position of the primary excitation. However, around the antiferromagnetic zone centre the primary excitation overlaps with the broad peak making the fits less reliable.

Average exchange parameters can be derived from the double Gaussian fits where the average excitation energy is defined as the centre of spectral weight. This first moments from the numerically integrated intensities are shown in figure 6.6 where errors are represented by the full width half maximum at the first moment energies. The corresponding exchange parameters found using equation 5.5 are $J_r = 10.69(4)$ K, $J_l = 4.37(2)$ K which agree with the average exchange parameters extracted from susceptibility measurements.

$$J_r = 10.69(4)\,\text{K},\ J_l = 4.37(2)\,\text{K} \tag{6.2}$$

Statistical multi-mode description

For the $BPCBC_x$ series of compounds the exchange geometry is shown in figure 4.6. In this picture the total rung exchange is formed from two exchange pathways and the leg exchange shares one of the halogens of the leg. On chemical tuning with Br/Cl substitution, the composition of the exchange pathway determines if either

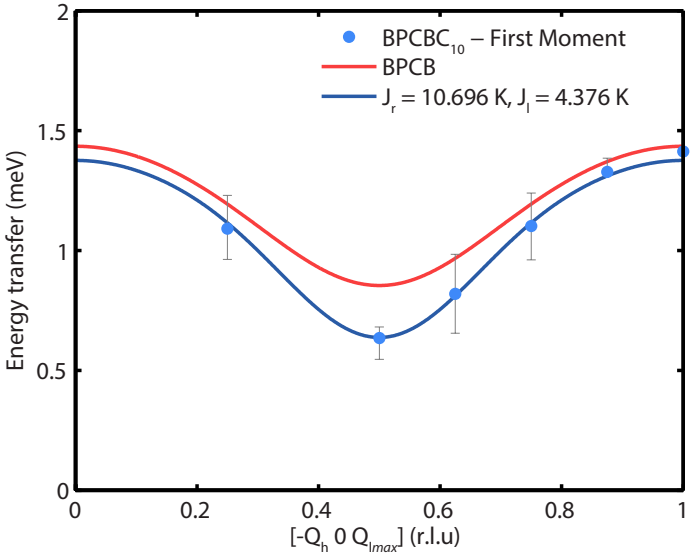

Figure 6.6: Dispersion of $BPCBC_{0.1}$ where the excitation energies have been extracted by the first moment approximation as described in the text. Exchange parameters $J_r = 10.696$ K and $J_l = 4.376$ K are obtained by fitting data points (blue points) to equation 5.5 (solid blue line). The dispersion of BPCB is shown in red for reference.

the leg, rung or both are affected by disorder. The probabilities of creating these effects as a function of composition (disorder) x is summarised in table 6.1 and plotted in figure 6.7 where it has been assumed that the occupation of each halogen site of the tetrahedra is equal.

Exchange Type	Exchange path	Exchange	Probability
$J_l(1)$	Br-Br	3.40	$(1-x)^2$
$J_l(2)$	Br-Cl	2.37	$2x \cdot (1-x)$
$J_l(3)$	Cl-Cl	1.34	x^2
$J_r(1)$	BrBr-BrBr	12.8	$(1-x)^4$
$J_r(2)$	BrBr-BrCl	10.455	$4x \cdot (1-x)^3$
$J_r(3)$	BrBr-ClCl	8.11	$2x^2 \cdot (1-x)^2$
$J_r(4)$	BrCl-BrCl	8.11	$4x^2 \cdot (1-x)^2$
$J_r(5)$	ClCl-BrCl	5.765	$4x^3 \cdot (1-x)$
$J_r(6)$	ClCl-ClCl	3.42	x^4

Table 6.1: Possible exchange configurations based on the exchange geometry introduced in figure 4.6. The dependence x of exchange configurations are given and exchange parameters for the case described in the text are given.

In table 6.1 the calculated exchange is an estimate based on the parameters determined for BPCB and BPCC, normalised to halogen species and number of pathways. These values assume that there is no chemically induced strain and the scaling of the total exchange is linear.

Figure 6.6 shows that for $x = 0.1$ the dominant exchange parameters are those of the pure system, making up $\approx 80\%$ of leg and $\approx 65\%$ of rung bonds. For the legs of the ladder the next highest probability is for an exchange mediated by one bromine and one chlorine atom, at $\approx 20\%$ and Cl-Cl exchange is negligible. For the rung the next most probable exchange is between three bromine and one chlorine at $\approx 30\%$.

Using this table, a set of 18 possible J_r and J_l combinations can be used to calculate possible dispersions based on a simple sum of coherent ladder excitations. Assuming that the scattering intensity is proportional to the probability of occur-

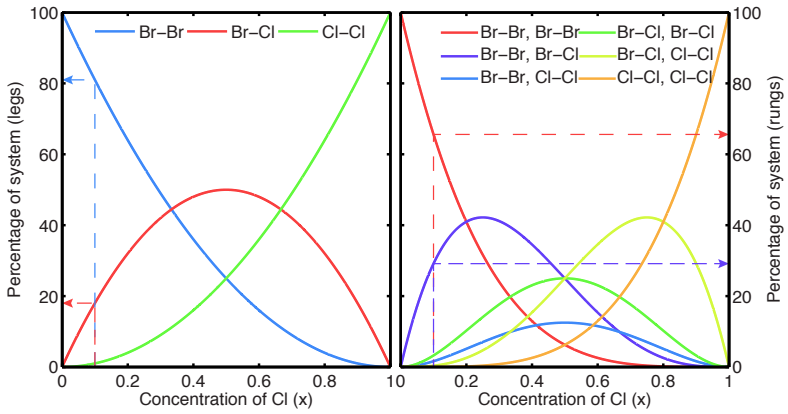

Figure 6.7: Probability of exchange configurations as a function x. Left) Probability of leg exchange interactions as a function of x as described in table 6.1 where probabilities for $x = 0.1$ have been highlighted. Right) Probability of rung exchange interactions as a function of x.

rence in the system and that the pure ladder structure factor is correct, a full dispersion can be approximated. The ladder structure factor depends on the scalar product of the exchange vector with Q (which will not change)and the spin-spin correlations. These correlations could be affected by the disorder in the system and would change from that of the pure system.

The effects of additional factors such as crystal strain are taken into account by parameters which shift the energy of each possible set of disordered exchange parameters between the pure cases. For example with $A = 0$, the rung exchanges are that of the pure Cl system and $A = 1$ is the pure Br system. For table 6.1 above, $A = 0.5$.

By sitting the internal strain and width of the excitation it is possible to describe the data. Strain was found on the rung only, with a strain value of 36%. This gives the dominant disordered exchange ($J_r(2)$) a value of

$$J_r(2) = J_r(1)/2 + 0.32 * J_r(1)/2 + 0.68 * J_r(6)/2 = 9.61\text{K}. \tag{6.3}$$

A minimal model can be formulated where only components where significant probabilities are included. Applying this model with the aforementioned strain parameters, an overall scaling parameter and instrumental resolution captures the

observed spectral shape and excitation energies of the experimental data as shown in figure 6.8.

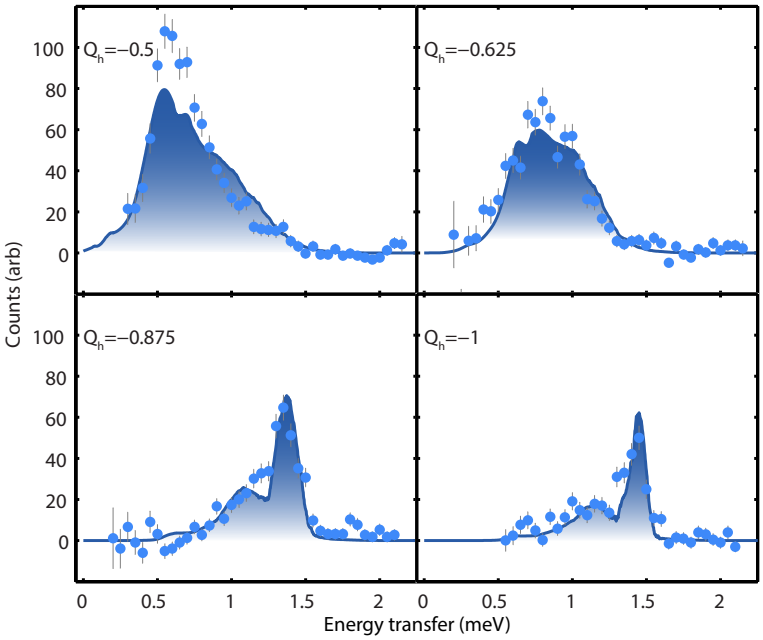

Figure 6.8: Energy scans at Q_h points across half the Brillouin zone for $BPCBC_{0.1}$ (blue points) and the multi-mode statistical dispersion (shaded area). Shaded areas correspond to the statistical model described in the text. The model has intrinsic excitation widths and has been scaled by a universal scaling parameter.

A similar method has been used for doped Mn_xMg_{1-x} chains to explore chain length, magnetic clusters and the impurity fractions [111]. A similar treatment for random bonds is unknown to the author. The validity of this method intrinsically implies that the coherence length of the excitations is greater than the spacial distance between rung types and those triplets of different energies are non-interacting. The spacial separation between rungs of the same energy in $BPCBC_{0.1}$ is 21.3 Å, where the coherence length is on the order of 10-20 Åfor the pure system.

Skew Gaussian approximation

The asymmetric line shape of the excitation spectra of $BPCBC_{0.1}$ follows a platykurtic distribution at the band gap and leptokurtic at the zone boundary as defined by their kurtosis. This is a measure of the statistical distribution of intensity above

and below the mean value. In a physical sense this measures the distribution of excitation energy about a central value. A similar statistical description is skewness, which can be extended to the skew normal distribution which can be used for data analysis [112]:

$$f(x) = \frac{1}{\omega\pi} e^{-\frac{(x-\xi)^2}{2\omega^2}} \int_{-\infty}^{\alpha\left(\frac{x-\xi}{\omega}\right)} e^{-\frac{t^2}{2}}\ dt, \tag{6.4}$$

where the real location of the excitation is given by ξ with a width given by ω and the distributions shape parameter is α. To calculate the distribution the identity of the second integral is given by the error function,

$$\Phi(x) = \int_{-\infty}^{x} \phi(t)\ dt = \frac{1}{2}\left[1 + \mathrm{erf}\left(\frac{x}{\sqrt{2}}\right)\right]. \tag{6.5}$$

To compare the distributions shape, conversion from α to skewness (γ_1) is performed,

$$\gamma_1 = \frac{4-\pi}{2} \frac{\left(\delta\sqrt{2/\pi}\right)^3}{\left(1 - 2\delta^2/\pi\right)^{3/2}}, \tag{6.6}$$

where δ is given by

$$\delta = \frac{\alpha}{\sqrt{1+\alpha^2}}. \tag{6.7}$$

Using this definition of a skewed normal distribution the line shape of the excitations of $BPCBC_{0.1}$ can be classified and nominal excitation energies extracted. The resulting fits to the data are shown in figure 6.9. This interpretation of the data gives the following set of exchange parameters;

$$\mathrm{J}_r = 11.1(7)\ \mathrm{K},\ \ \mathrm{J}_l = 4.4(7)\ \mathrm{K} \tag{6.8}$$

Comparisons can immediately be drawn to the first moment approximation described above. It is found that the leg exchange is equal within error and the rung exchange is larger, but still within error. This result is unsurprising as the first moment approximation is the mean of spectral weight and as such is dependent on line shape. In the skew approximation the definition of skewness is based on the

ratio of cumulants for the distribution. The energy derived from the cumulants is therefore more suited to a description of a main mode with lower energy sub-states.

As shown in the bottom right panel of figure 6.9 the extracted line shape describes the skewness of the data and tends to positive energy gain at the spin gap and to lower energies at the zone boundary.

To completely describe the scattering in the spectra, a second non-dispersing mode at the spin gap has been applied. The significance of this mode at the spin gap suggests that there are isolated dimers which are formed on rungs with an energy of ≈ 0.6 meV. Assuming the exchange parameters in table 6.1 are approximately valid, this mode corresponds to an isolated rung formed from an exchange consisting of two Br and two Cl atoms. From the exchange structure, this means that it is probable that there is an imbalance in the two leg exchanges which leads to localisation.

6.4 Exact diagonalisation of the bond-randomised ladder Hamiltonian

The Hamiltonian for a disordered spin ladder (equation 6.1) can be solved using exact diagonalisation. Diagonalisation of this Hamiltonian has been performed by S. Furuya (Uni. Geneva) and is explained below [113].

The bond-randomised spin ladder Hamiltonian given in 6.1 can be mapped to the simpler problem of a chain of spinless Fermions. To start, the pseudo spin transformation $\hat{\mathbf{S}}_j$ consisting of operators

$$S^{\pm}_{l,k} = \frac{(-1)^k}{\sqrt{2}}\hat{S}^{\pm}_l,\ S^z_{l,k} = \frac{1}{4}(1+2\hat{S}^z_l) \tag{6.9}$$

are applied to the Hamiltonian, which transforms it into

$$\mathcal{H} \simeq \sum_j \frac{J_{l_{j,1}} + J_{l_{j,2}}}{2}\left(S^x_j S^x_{j+1} S^y_j S^y_{j+1} + \frac{1}{2}S^z_j S^z_{j+1}\right) - \sum_j \left(g\mu_B H - J_{r_j} - \frac{J_{l_{j,1}} + J_{l_{j,2}}}{2}\right) S^z_j. \tag{6.10}$$

Applying the Jordan Wigner transformation $\hat{S}_l = c^\dagger_l \exp\left(i\pi \sum_{m<l} c^\dagger_m c_m\right)$ and $\hat{S}^z_l = c^\dagger_l c_l - 1/2$ results in the Hamiltonian for a chain of spinless Fermions where quadratic multi-magnon modes have been ignored:

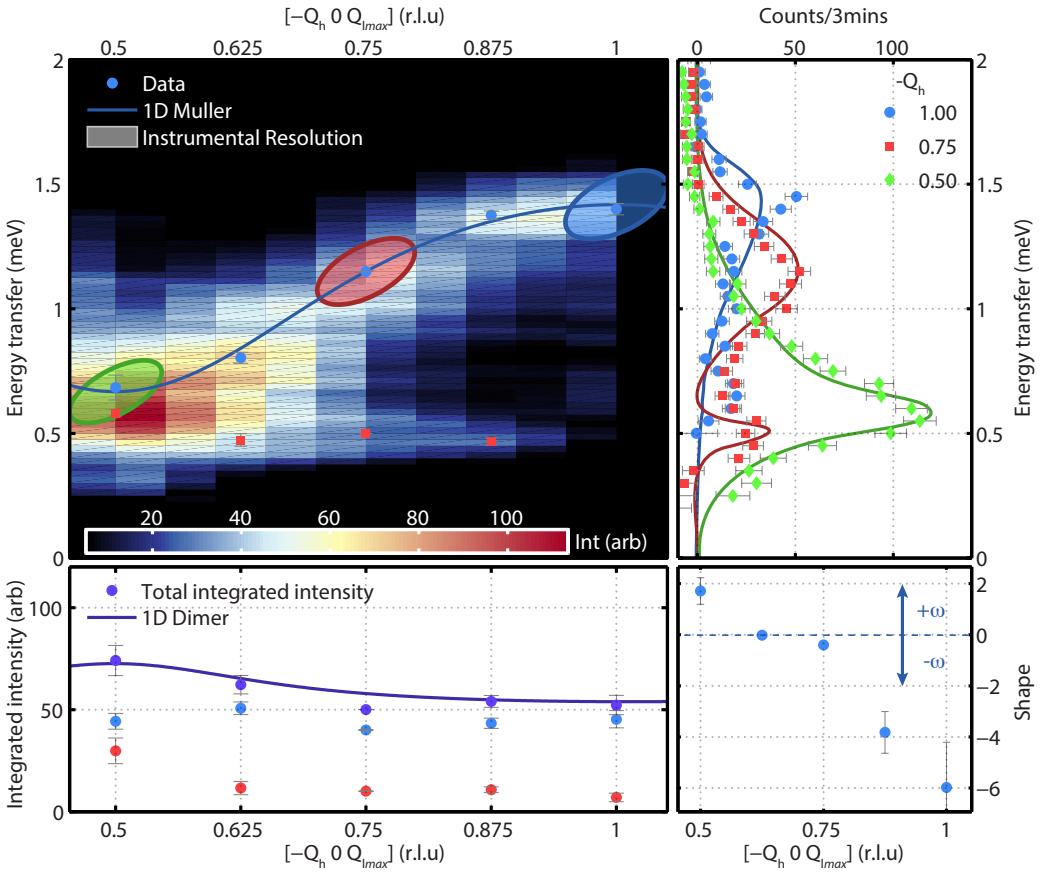

Figure 6.9: Dispersion of $BPCBC_x$ along the one magnon structure factor maximum measured on the triple axis spectrometer IN14 (ILL). a) Excitation energies from the skew Gaussian approximation corrected for instrumental resolution (blue points) and the non-dispersing mode (red points). The dispersion based on the extracted exchange parameters $J_r = 11.1(7)$ K, $J_l = 4.4(7)$ K are shown as a blue line. Projections of resolution ellipsoids at various points of the dispersion are shown as shaded ovals. b) Energy scans at $-Q_h = 1.00, 0.75, 0.50$ and the best fit to resolution convolved skew Gaussian. c) Q dependence of resolution corrected integrated spectral intensity and a fit to equation 5.9. d) Shape parameter from the skew Gaussian fit. Spectral weight extends to higher energies at the gap (positive skew) and lower energies at the zone boundary.

$$\mathcal{H} \simeq \frac{1}{2}\sum_{j}\frac{J_{l_{j,1}}+J_{l_{j,2}}}{2}\left(c_j^{\dagger}c_{j+1}+\text{H.c.}\right)-\sum_{j}\left(g\mu_B H-J_{r_j}\right)c_j^{\dagger}c_j, \tag{6.11}$$

which for $x = 0$ gives a dispersion which is analogous to that of Müller *et al.* (equation 5.5) except without the higher order corrections.

$$\omega\left(\mathbf{Q}\right) = J_r + J_l\cos\left(\mathbf{Q}\right) - g\mu_B\mathrm{H}. \tag{6.12}$$

The dynamical structure factor can be expressed by a sum of delta functions,

$$S^{xx}\left(\mathbf{Q},\omega\right) = \frac{1}{N}\sum_{n=0}^{\infty}\frac{1}{2^3}\left\langle\psi_n\right|c_q^{\dagger}\left|\psi_0\right\rangle^2\delta\left(\omega-E_n+E_0\right). \tag{6.13}$$

This is the structure factor for a possible disordered configuration. By performing this for many disordered realisations, it is possible to average $(\overline{\mathcal{O}})$ the contribution to remove artefacts.

$$S^{xx}\left(\mathbf{Q},\omega\right) = \frac{1}{N}\sum_{n=0}^{\infty}\frac{1}{2^3}\overline{\left\langle\psi_n\right|c_q^{\dagger}\left|\psi_0\right\rangle^2\delta\left(\omega-E_n+E_0\right)} \tag{6.14}$$

The results for $x = 0$, 0.05, 0.10 with the probability distribution and exchange parameters introduced in table 6.1 are shown in figure 6.11. For the pure case a single sharp excitation is observed at energies corresponding to equation 6.12 described by J_r = 12.8 K, J_l = 3.4 K. On application of randomisation the excitation becomes broader and a pocket of intensity below the pure dispersion emerges. At $x = 0.05$ this pocket shows a dispersionless structure which decays moving away from the antiferromagnetic zone centre. Increasing the disorder to $x = 0.1$ leads to depopulation of states corresponding to the pure system around the gap and the appearance of a clear second mode at lower energies. The Q range of this mode has increased from the $x = 0.05$ case and a cosine dependence is visible. Below this mode is a non-dispersive mode around 0.6 meV which extends over the entire zone. At the zone boundary there is a slight softening of the pure mode by 0.02 meV.

For the exact diagonalisation finite size effects have been investigated and it has been found that for $n = 100$ and averaging over 200 samples the results are in the infinite system size limit. The occurrence of the dispersing mode at energies below

the gap can be explained by the disorder in J_r, lowering the local gap. The dominant randomisation at $x = 0.1$ is for one Br to be exchanged for a Cl on a rung, which is enforced by our choice of $J_r(p)$. Analogously the choice of $J_l(p)$ leads to little observable effects on the shape despite contributing to 20% of the system.

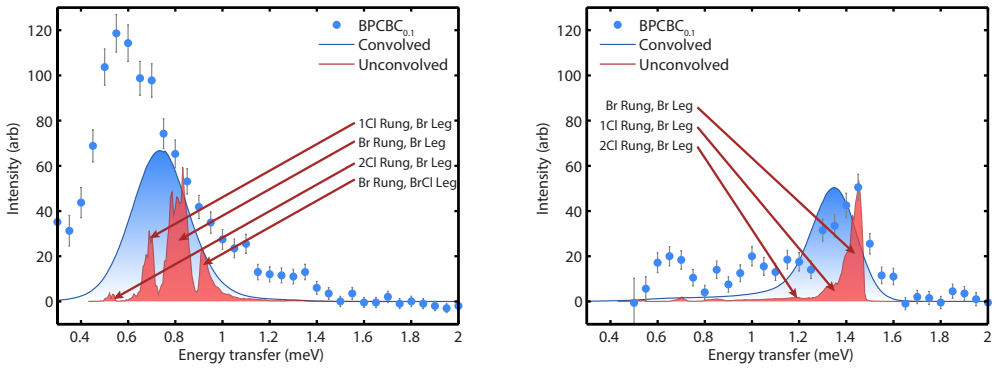

(i) $Q_h = -0.5$ (ii) $Q_h = -1.0$

Figure 6.10: Energy scans for $BPCBC_{0.1}$ at the gap (Left) and zone boundary (Right) and the corresponding simulation for a disordered spin ladder. Unconvolved simulations are shown in red, where the inter-gap sub-states are visible. When convolved with instrumental resolution (blue area) the sub-state cannot be resolved.

The simulations have been convolved with the instrumental resolution and comparisons with the data are shown in figure 6.10 (Left) for the gap and zone boundary 6.10 (Right). The unconvolved simulations are shown and are scaled to the experimental data. At the gap the three modes are visible with energies that are compatible with the experimental data. The convolved simulation is also shown and scaled to the data. The effect of instrumental resolution is to push the spectral weight to lower energies and to smooth out the three modes. The intensity of the convolved simulation peaks at 0.7 meV and is dominated by the pure contribution, where the other two modes provide asymmetry and width. At the zone boundary the simulation accurately predicts the energy of the pure mode at 1.4 meV and lower energy contributions.

The simulations of a disordered ladder with $x = 0.1$ have lead to predictions which quantitatively agree with experimental data. In the simulations spectral

weight is predominantly concentrated around modes corresponding to the pure system whilst in the data the pure mode is mostly suppressed around the band gap. The transfer of spectral weight to lower energy excitations is dependent of the value of x. From powder diffraction data we see that precise control of the chlorine content is difficult with a tendency towards higher concentrations for low values of x. Simulations for $x > 0.1$ are currently being prepared by the University of Geneva. The probability functions for rung and leg randomisation are determined by the ideal case, however some site dependence to chlorine placement has been observed, which can be included and would add a preference to rung disorder. Lastly the exchange energies for a partially substituted bond can be modified. The BrBr-BrCl exchange is the most dominant disordered bond and will be the starting point for simulation optimisation.

6.5 Conclusions

The random bond spin ladder $BPCBC_{0.1}$ has been measured on the triple-axis spectrometer IN14 and the excitation spectra obtained. The spectrum shows a broad excitation above resolution with an anomalous line shape. This has been modelled by a skewed Gaussian line shape and an additional non-dispersive mode as summarised in figure 6.9.

The mode has a characteristic line shape which can be described by a skew parameter which accounts for a tail to high energies at the antiferromagnetic zone centre and towards low energies at the zone boundary. The average exchange parameters determined by this method are J_r = 11.1 (7) K, J_l = 4.4(5) K with an additional localised mode at 0.6 meV. The average exchange parameters from this analysis are consistent with those found by magnetic susceptibility measurements summarised in table 4.5.

By reference to the numerical study by Vojta [102] and to the results from exact diagonalisation presented in section 6.4 the origin of this line shape can be described. We find that primarily the decreased rung exchange has the effect of lowering the overall excitation energy and to split the one magnon excitation into multiple modes. These modes originate from areas of the ladder which have coherent excitations

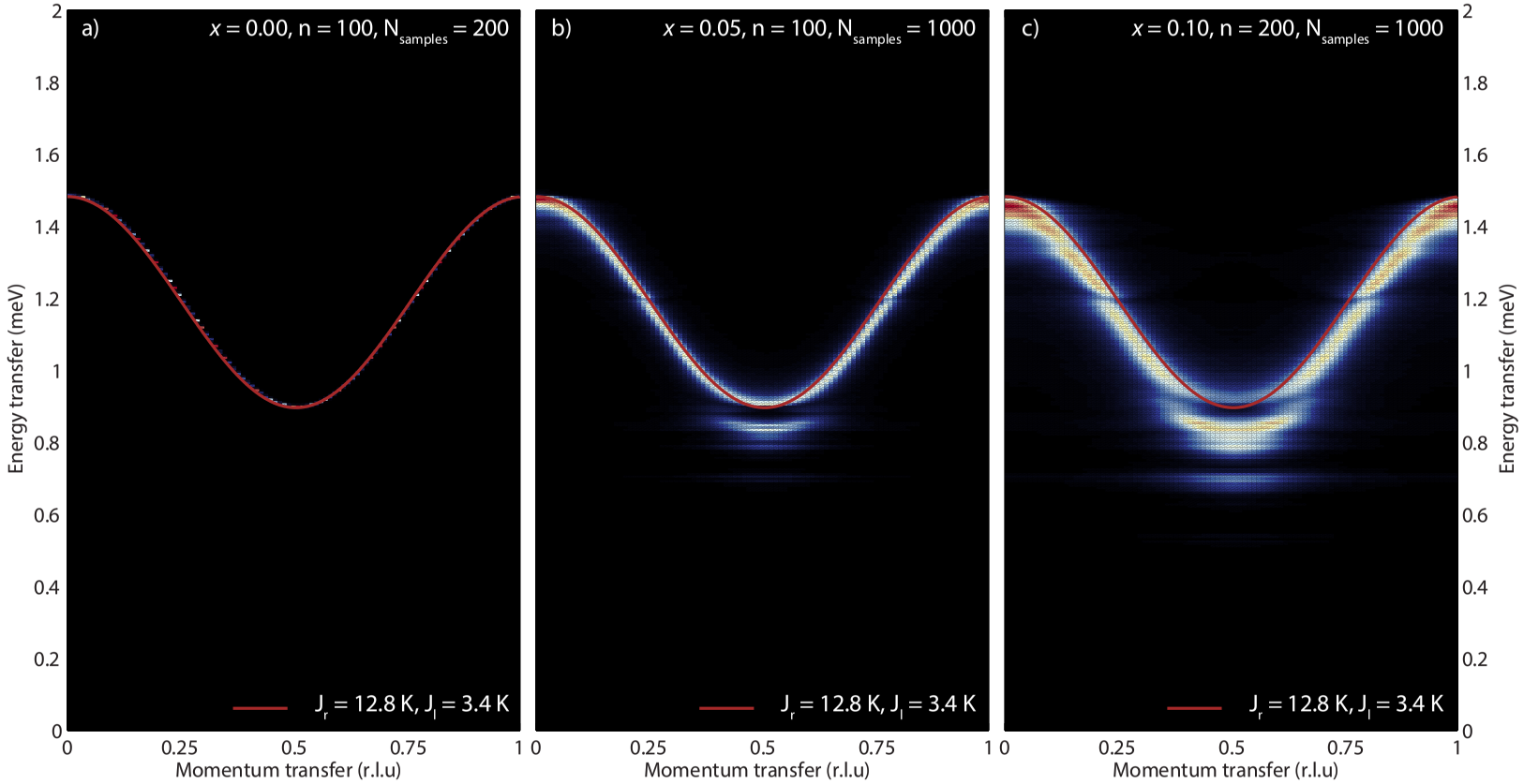

Figure 6.11: Q Vs. Energy map for simulations on a bond disordered ladder for $x = 0$, 0.05 and 0.1. The solid line represents the pure case of BPCB with chain mapping and overlaps with the simulated excitation spectrum (Left). As x is increased (Middle) a non-dispersive pocket of inter-gap states opens and the spectral weight shifts to lower energies. At $x = 0.1$ (Right) the dispersion shows signs of splitting into two.

from reduced exchange parameters. The modes and their origin are shown in figure 6.10. When the dispersion calculated by exact diagonalisation is convolved with the instrumental resolution we observe that the asymmetric line shape is reproduced in the simulations. In comparison with the experimental data we find remarkably good agreement.

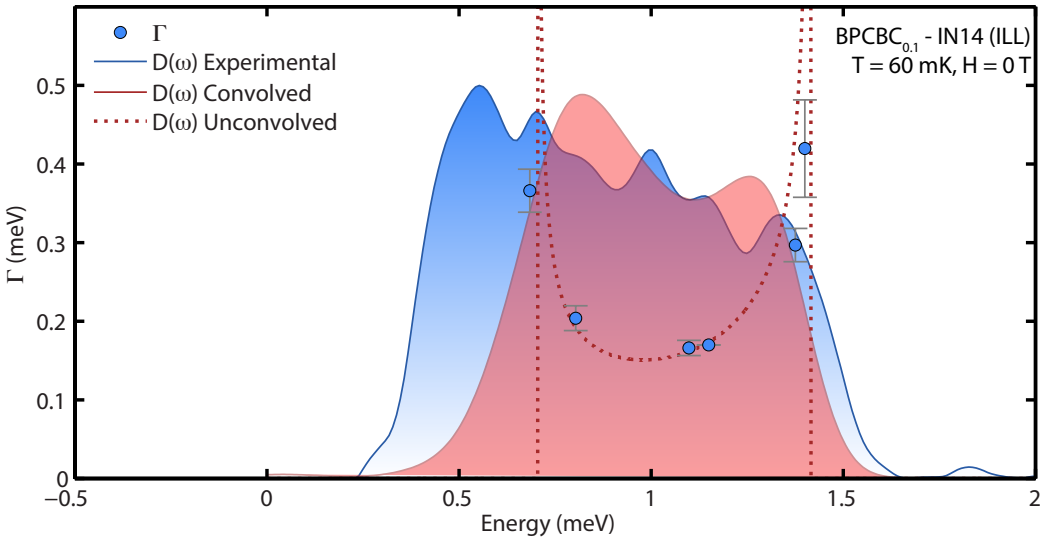

Figure 6.12: Intrinsic magnon line widths for $BPCBC_{0.1}$ as measured on IN14 (blue symbols). Dashed lines correspond to the scaled densities of magnon states as calculated from the exchange parameters $J_r = 11.1$ K, $J_l = 4.4$ K. Solid areas correspond to the resolution convoluted density of state (red) and the observed density of state (blue).

It was discussed in section 6.1 that the finite magnon lifetime observed in reference [88] is due to scattering of magnon impurities. For the data obtained for $BPCBC_{0.1}$ we find that there is a general agreement with the excitation widths and density of states as shown in figure 6.12. However the observed density of state differs from the calculated value for the exchange parameters given above, with lower energy states below the gap corresponding to magnon localisation. Excitation widths however follow the unconvolved density of state which implies that the magnon lifetimes are affected by magnon impurities.

Chapter 7

Excitations in the Luttinger-liquid phase

Contents

The Luttinger-liquid phase is a state which is unique and characteristic to one dimensional models. Arising from the collective nature of excitations and strong interactions, the low energy physics is controlled by two parameters u and K. Luttinger-liquid theory can be applied to spin ladder systems, such as the model materials BPCC and BPCB. The complex excitation spectrum of the Luttinger-liquid phase has been studied using neutron scattering and modelled by DMRG, showing excellent agreement between theory and experiment. The case of spin incoherence in the Lutinger-liquid phase has also been examined.

7.1 Introduction to spin Luttinger-liquid physics

Luttinger-liquid theory descries one dimensional models with strong interactions and collective bosonic excitations with a linear spectrum. The properties of the Luttinger-liquid can be contrasted to those of Landau-Fermi-liquid theory which is valid in higher dimensions. The Hamiltonian depends on two material-specific parameters u and K, the excitation propagation velocity and Luttinger parameter. The key features of a Luttinger-liquid are collective excitations, a gapless dispersion which is linear around the Fermi level and spin and charge separation. At T = 0 both the spin and charge are coherent in the spectral function. At higher temperatures the spin degree of freedom becomes incoherent. The effect of temperature is examined in section 7.3.

7.1.1 Generalities of a Luttinger liquid

In dimensions greater than two where Fermi physics dominates, Landau Fermi liquid theory adequately describes complex weak interactions by describing the system as a free electron gas. In such a system at T = 0 a number of particles with quantised momentum are added to the system, filling the lowest well-defined energy states. When all particles are added, the system is filled up to a level which is called the Fermi level, where the sharp discontinuity in the density of occupied states creates a Fermi surface. Elementary excitations are from the Fermi sea to a higher level, creating quantised excitations which have infinite lifetime, well defined momentum and energy. A hole quasiparticle with the same energy and opposite momentum is left behind.

The effect of temperature is to take states from within the Fermi-sea and populate higher energy states, removing the discontinuity and introducing a gradient in the density of states over a range of energy, described by a Boltzmann distribution.

When interactions are included the free electron gas picture holds except the dynamical properties (for example mass) are renormalised. This comes from the influence of other particles. The excitations acquire a finite lifetime.

This brief and simple explanation does not do justice to Landau Fermi liquid theory but covers the main features and is a starting point for contrasting the differences

with Luttinger-liquid theory and the peculiarities of one dimensional physics. Further in-depth descriptions can be found in the work of Landau, references [114, 115] and any good condensed matter text book such as Kittel [116].

In Landau Fermi liquid theory when an excitation is formed a particle with momentum k is excited to a level above the Fermi-surface with momentum $k + q$ and a hole is left with momentum k. When the q dependence is considered for $k < 2k_f$ there is a continuum for all k due to the ability to create excitations with energy arbitrarily close to the Fermi energy for all q. These excitations are created by the elevation of a single particle to a higher energy state.

In one dimension Landau Fermi liquid theory is no longer adequate. The strong interactions and the low dimensionality break the free electron gas analogy which relies on weak interactions and thus enforce collective excitations. For an arbitrary dispersion relation constrains are placed on the lower energy and momentum of the excitation. These cusps in the dispersion have a finite slope which is related to the quasiparticle velocity and Luttinger parameter.

The above properties are the basis for Luttinger-liquid theory (LL). The long lived bosonic quasiparticles are highly interacting because of the dimensionality and can only propagate through collective movement, which is linked to the quasiparticle density. Solving the density operator leads to a description which is dependent only on the bosonic fields $\psi(x)$ and $\theta(x)$, representing the longitudinal and transverse components of spin, with the differentials being the spin fluctuations. A technique called bosonization allows us to write the most simplistic Hamiltonian for the low energy properties, which is named the Luttinger-liquid Hamiltonian,

$$\mathcal{H}_{LL} = \frac{1}{2\pi} \int dx \left\{ uK \left[\partial_x \theta(r)\right]^2 + \frac{u}{K} \left[\partial_x \phi(r))\right]^2 \right\}. \tag{7.1}$$

A full explanation can be found in reference [69]. Of particular note is that the Hamiltonian is that of a massless system. The pre-factors of the bosonic fields u and K characterise all of the low energy properties regardless of the geometry of the one dimensional system. K is the Luttinger parameter which defines the powerlaw decay of the correlation functions and u is the velocity at which the bosonic excitations propagate.

Since all properties are dependent on these parameters, all Luttinger-liquids have enforced commonality. As described earlier, the excitation spectrum is gapless with

two nodes on the Fermi surface. The energy spectrum is linear at low energy due to the creation and annihilation of quasi-particles around the Fermi level. The quasi-particle and hole have different velocities and as such there is a separation of spin and charge.

The Luttinger-liquid behaviour is a peculiarity of one dimension and can be found in many systems. These include one dimensional wires [117] and carbon nano-tubes [118], spin chains [119] and spin ladders [20, 120]. Real model materials such as pure BPCB or BPCC compounds, with known exchange parameters and minimal DMI and other anisotropies, lend themselves to the study of Luttinger-liquid physics.

Of particular interest to us is when Luttinger-liquid physics occurs in spin ladders. This happens when the energy of the lowest energy triplet state is below that of the singlet, i.e. when there is a finite density of magnons. The magnetic field acts as a control parameter, or chemical potential. In the Fermionic picture, the chemical potential controls the depth of the $|s\rangle$ and $|t^+\rangle$ Fermi sea. The resulting excitations from and within this sea can be split into low energy and high energy classes. Figure 7.1 shows that for low energy excitations the dispersion is linear at the filling level (orange arrows).

The following sections will detail the high and low energy sectors and present work obtained on BPCC for the Luttinger-liquid phase.

7.1.2 Low energy excitations

In the spin LL phase the spectrum is gapless due to the softening of the $|t^+\rangle$ excitation. Driven by the Zeeman effect, the lowest energy states are the singlet $|s\rangle$ and $|t^+\rangle$ triplet. In the Fermionic picture, the magnetic field acts as a chemical potential, controlling the magnetisation. The points where the spectra are gapless are determined by this magnetisation.

The minima in the dispersion for the singlet mode are given by πm^z, $\pi\left(2-m^z\right)$ and $\pi\left(1-m^z\right)$, $\pi\left(1+m^z\right)$ for the triplet excitations (see figure 7.1), where m^z is the chemical potential. Using this notation, the minimum points for all possible continua can be calculated [7].

In the low energy sector, excitations between the $|s\rangle$ and $|t^+\rangle$ states lead to

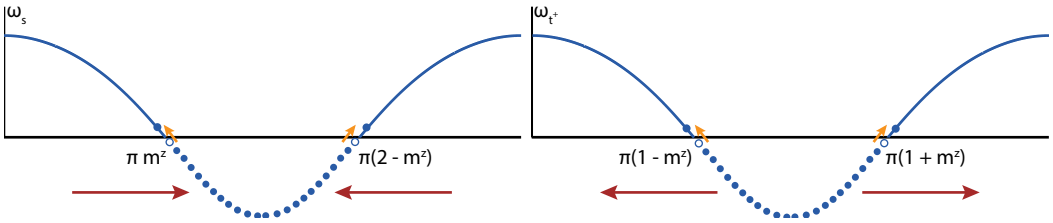

Figure 7.1: Fermion representation of the filling of the singlet and lowest energy triplet band.Orange arows show an excitation and the linearity of the low energy cusps.

a continuum, which at half magnetisation is reminiscent of the excitations of a $S = 1/2$ spin chain. This continuum has been studied in reference [19] for BPCB and $KCuF_3$ [121]. This can be understood as the two lowest energy states are effectively $S = 0$ and $S = 1$, with the magnetic field controlling the density of rung triplets which varies between 0 and 1. Projecting out the higher energy states, the low energy simplification is called Bosonization. Bosonization can be applied to many theoretical problems such as quantum wires [122], quantum hall edge states [123] and the Kondo lattice [124] as well as problems in one dimension. The book by T. Giamarchi [125] and the course from reference [126] are excellent starting points to learn Bosonization and the tutorial by Schonhammer [127] explains the application of Bosonization with respect to the spin LL.

The Hamiltonian for an XXZ spin chain is:

$$\mathcal{H}_{XXZ} = \sum_i \mathrm{J}_l \left(\hat{S}_i^x \hat{S}_{i+1}^x + \hat{S}_i^y \hat{S}_{i+1}^y + \delta \hat{S}_i^z \hat{S}_{i+1}^z \right) - \left(2h_s \frac{H - (H_c + H_s)/2}{H_s - H_c} \right) \hat{S}_i^z, \tag{7.2}$$

which can have the ladder Hamiltonian (5.1) mapped onto it. The XXZ Hamiltonian (equation 7.2) can be solved by mapping onto the spin LL Hamiltonian given in equation 7.1. This case that can be solved by the use of appropriate spin $\frac{1}{2}$ operators; $\left[S_{l,k}^x, S_{l,k}^y\right] = iS_{l,k}^z$ and $S_{l,k}^{\pm} = S_{l,k}^x \pm iS_{l,k}^y$. By application of Boglibov transformations mapping to the LL Hamiltonian is complete [125].

The spin LL Hamiltonian (equation 7.1)can be used to describe the low energy collaborative excitations of both the spin ladder and chain.

For $m = 0.75$ the depth of the Fermi sea for $|s\rangle$ and $|t^+\rangle$ are unequal and such that the excitations deviate from that of the spin chain at zero field. Symmetry

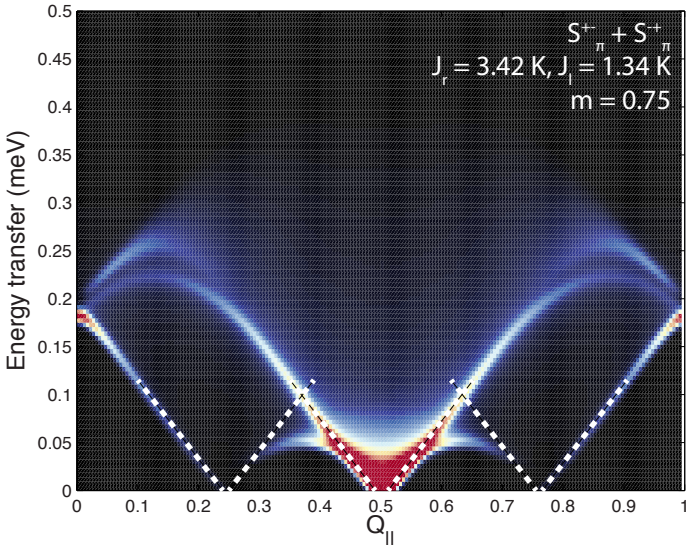

Figure 7.2: Low energy spinon continuum for exchange parameters corresponding to BPCC at $m = 0.75$ for the $S^{\pm}_{\pi}$ and $S^{\mp}_{\pi}$ channels in the π sector by DMRG. Dashed lines represent the cusps of the excitation spectra, showing the linear behaviour of a spin LL and the zero energy crossing points.

about the half magnetisation point means that the excitation spectra are identical to $m = 0.25$. The spectrum for the $Q_y = \pi$ sector is shown in figure 7.2. White dashed lines show the linear edges and the corresponding zero energy crossing points. In the π sector the minima are at 0.25, 0.5 and 0.75, agreeing with the formula as a function of m^z given above. The slope of these excitations corresponds to the spinon velocity, which depends on the exchange.

Equation 7.2 has also been solved exactly in reference [128] via the algebraic Bethe ansatz, obtaining the correlation functions for an arbitrary magnetisation.

7.1.3 High energy excitations

At higher energies there are two sources of excitations, $|s\rangle \rightarrow \left|t^0\right\rangle$, $|t^-\rangle$ and $|t^+\rangle \rightarrow \left|t^0\right\rangle, |t^-\rangle$ which are gapped and for which an example is shown in figure 7.3. As shown in table 5.2, these have different parities and hence are separate in momentum space. By tuning the magnetisation the dispersion gaps can be driven

to incommensurate momentum values. These minima are given by $\pi(1-m^z)$ and $\pi(1+m^z)$. Unlike in the quantum disordered regime ($H < H_c$), the excitations are not sharp, but form a continuum.

The Fermionic representation can also be used for the high energy sector. Surprisingly the Hamiltonian can be mapped onto an effective t-J model Hamiltonian (equation 7.3) [7]. The three lowest energy states are mapped to the t-J model by the pseudo-spins $|s\rangle = \left|\tilde{\downarrow}\right\rangle$ and $|t^+\rangle = \left|\tilde{\uparrow}\right\rangle$ and in this picture the excitation $\left|t^0\right\rangle = |0\rangle$ is a single hole excitation.

$$\mathcal{H}_{\text{t-J}} = \mathcal{H}_{\text{XXZ}} + \mathcal{H}_{\text{t}} + \mathcal{H}_{\text{s-h}} + \varepsilon \tag{7.3}$$

where $\varepsilon = (J_r + h^z)/2$ is an energy shift, $\mathcal{H}_{\text{XXZ}}$ is the XXZ $S = 1/2$ chain Hamiltonian (equation 7.2) and $\mathcal{H}_{\text{t}} = J_l/2 \sum_{l,\sigma}(c^\dagger_{l,\sigma} c_{l+1,\sigma} + h.c.)$ is the hopping term[129]. In this representation $c^\dagger_{l,\sigma}$ ($c_{l,\sigma}$) is the creation (annihilation) operator of a Fermion with pseudo spin $\sigma = \tilde{\uparrow}, \tilde{\downarrow}$ at the site l.

One powerful method of solving the Hamiltonians presented here is the Density Matrix Renormalisation Group (DMRG) technique. The PhD thesis of our collaborator P. Bouillot (University of Geneva - CH) [7] is an extensive and definitive work on the application of DMRG to ladder systems and provides an in-depth explanation of DMRG. Using DMRG it's possible to access both static and dynamic correlations at zero temperature and finite temperatures. All numerical simulations presented here have been calculated at University of Geneva with the code developed by P. Bouillot for his thesis unless stated otherwise.

Figure 7.3: High energy excitations exchange parameters corresponding to BPCC at half magnetisation by DMRG. Left) S^{zz}_{π} excitation channel corresponding to $|s\rangle \rightarrow \left|t^0\right\rangle$ and $S^{\pm}_0$ corresponding to $|t^+\rangle \rightarrow \left|t^0\right\rangle$. The incommensurate minima is shown by solid white arrows.

As an example, the high energy spectrum for the S^{π}_{zz} ($|s\rangle \rightarrow \left|t^0\right\rangle$) and S^0_{+-} ($|t^+\rangle \rightarrow \left|t^0\right\rangle$) channels is shown for half magnetisation in figure 7.3. The incommensurate minima of the spectra are at $Q_h = 0.25$ for both sectors. A continuum structure is also visible, deriving from the excitations of the Fermi-sea. The in-

creased energy at $\mathrm{Q}_h = 0$ in the S^0_{+-} channel is due to the triplet-triplet repulsion energy, term $H_{\text{s-h}}$ in the Hamiltonian (equation 7.3):

$$\mathcal{H}_{\text{s-h}} = -\frac{J_l}{4}\sum_l \left[n_{l,h}n_{l+1,\tilde{\uparrow}} + n_{l,\tilde{\uparrow}}n_{l+1,h}\right], \tag{7.4}$$

where $n_{l,h}$ is the density operator for holes at site l, which is field dependent.

The material parameters J_r and J_l for BPCC have been derived in section 5.3 and can be used in the t-J Hamiltonian. The excitations occur from the correlations given by:

$$S^{\alpha\beta}_{Q_y}(q,\omega) = \frac{2\pi}{L}\sum_\lambda \left|\langle\lambda|S^\beta_{Q_y}|0\rangle\right|^2 \delta\left(\omega + E_0 - E_\lambda\right). \tag{7.5}$$

For neutron scattering measurements the scattering cross section, which is a combination of all correlations where the excitation sectors are separated by parity. The total structure factor is given by:

$$\begin{aligned}\frac{d^2\sigma}{d\Omega dE'} = \frac{q'}{q}|F(\mathbf{Q})|^2 \Bigg\{ & 4\left(1-\frac{Q^{z2}}{Q^2}\right)\left[c(\mathbf{Q})\cdot S_0^{zz} + s(\mathbf{Q})\cdot S_\pi^{zz}\right] \\ & + \left(1+\frac{Q^{z2}}{Q^2}\right)\left[c(\mathbf{Q})\cdot\left(S_0^{+-}+S_0^{-+}\right) + s(\mathbf{Q})\cdot\left(S_\pi^{+-}+S_\pi^{-+}\right)\right]\Bigg\},\end{aligned} \tag{7.6}$$

where $s(\mathbf{Q}) = \sum_{i=1,2}\sin^2(\mathbf{Q}\cdot\mathbf{r_i}/2)$ and $c(\mathbf{Q}) = \sum_{i=1,2}\cos^2(\mathbf{Q}\cdot\mathbf{r_i}/2)$ with the rung vectors $\mathbf{r_i}$. The magnetic form factor $F(\mathbf{Q})$ is the standard form factor for a bare Cu^{2+} ion and q'/q is a k_f/k_i correction. Q^z represents the momentum transfer component parallel to the field. The full spectrum for$m = 0.5$ is presented in figure 7.4 (Top) and m = 0.75 (Bottom) and have been separated into excitation sectors.

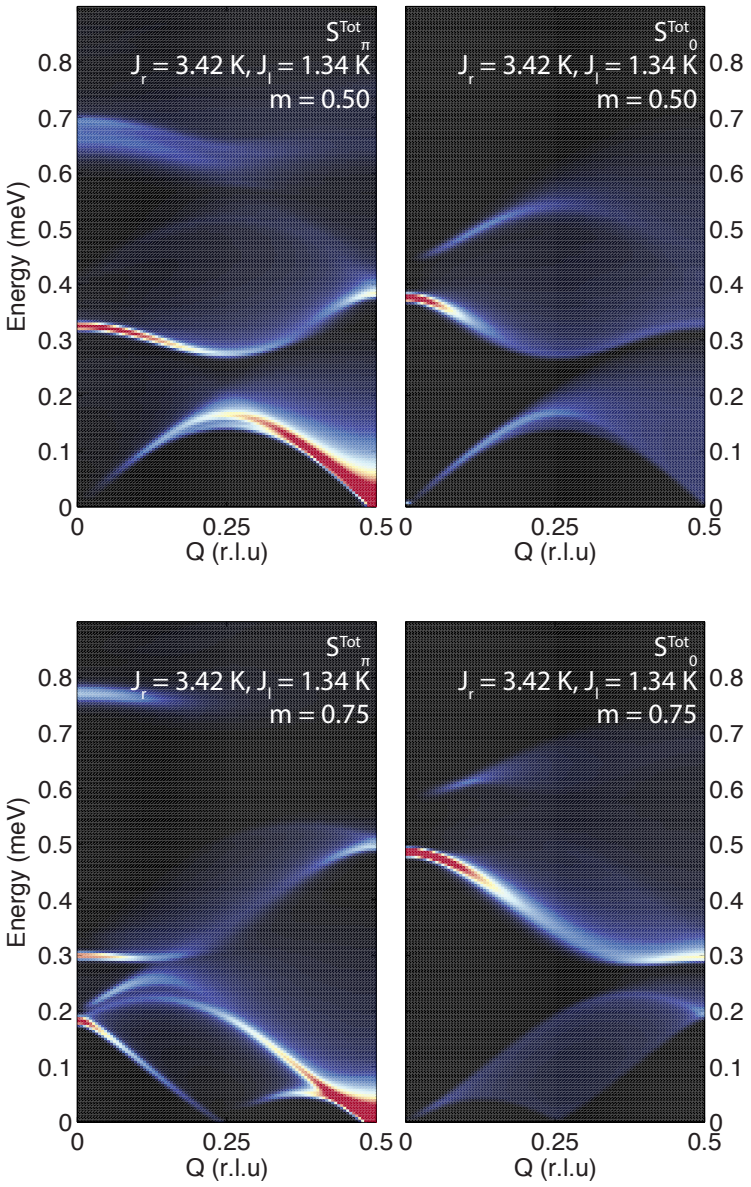

Figure 7.4: Simulated excitation spectra for BPCC at half (Top) and three quarters (Bottom) magnetisation. Left panels show the total contribution to the spectrum in the π sector and the right panel the 0 sector.

7.2 BPCC - Investigations in the spin Luttinger liquid phase

The spin ladder material BPCC has exchange parameters $J_r = 3.42$ K and $J_l = 1.34$ K, which correspond to critical points at $H_c = 1.57$ T and $H_s = 4.02$ T. These magnetic fields are experimentally accessible with modern cryomagnets and as such excitations in the entirety of the Luttinger liquid phase can be studied.

The low-energy time-of-flight (ToF) spectrometer LET at ISIS is one of the new generation ToF spectrometers, with unprecedented energy and momentum resolution over a large volume of momentum and energy space. With a maximum magnetic field of 9 T it is the ideal choice of instrument to measure the excitation spectra of BPCC. The following experiment was designed to measure excitations in the LL phase, unequivocally confirm the spin ladder Hamiltonian at zero field and find the exchange parameters in the field-induced ferromagnetic phase. The results for the zero and high-field phases are presented in chapter 5.

7.2.1 Experimental setup

High quality single crystals of BPCC were produced by the evaporative technique descried in section 4.1.1 by Karl Krämers group (University of Bern - CH). 19 single crystals were available and the best 11 were selected based on the criteria in section 4.1.3. A total sample mass of 1.8 g was co-aligned using the 4 circle diffractometer Morpheus (PSI - CH) on a custom made aluminium mount as shown in figure 7.5

A dilution insert was used in conjunction with a 9 T cryomagnet to reach a base temperature of 60 mK. To cover the intended momentum and energy range a primary E_i of 2.5 meV was selected with frame overlap and resolution choppers spinning at 120 Hz. This setup allows for an energy resolution of 44.8 μeV and a secondary E_i of 1.16 meV. The use of these choppers is discussed in section3.1.2.

By rotating the sample and measuring, it is possible to build up a 4-dimensional dataset covering the required volume in energy and momentum. For BPCC, parity separates the π and 0 sectors. To cover both sectors, two sets of rotations have been used. The final coverage for $E_i = 2.5$ meV in inverse angstroms is shown in figure 7.6.

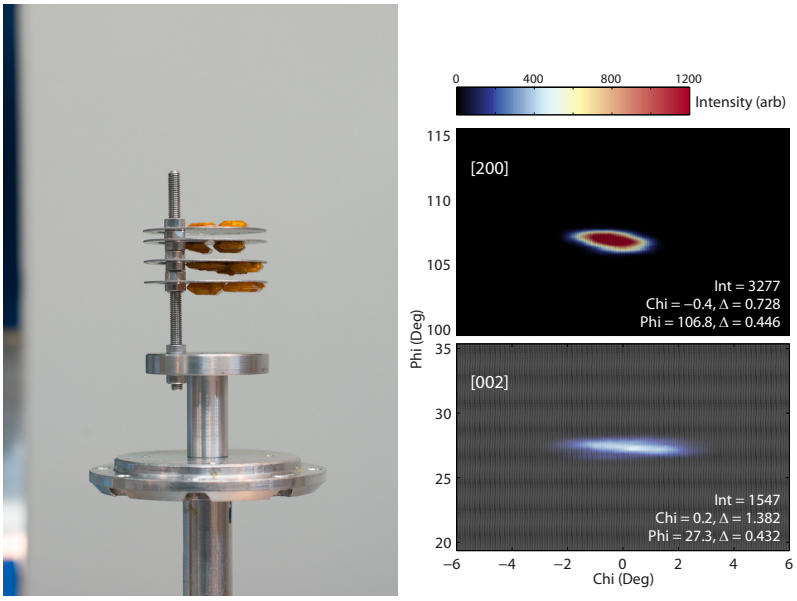

Figure 7.5: 11 co-aligned single crystals of BPCC (Left) and the final alignment (Right). Alignment was checked on the [2 0 0] (Right top) and [0 0 2] (Right bottom) reflections by the process described in section 4.1.3.

7.2.2 Results and analysis

Horace scans[a] covering the momentum energy volume shown in figure 7.6 where performed at H= 3.154 T and H = 4.067 T. With a g factor of 2.06, these fields correspond to nominal magnetisation values $m = 0.5, 0.75$. This g factor was derived from thermodynamic measurements since there are no published ESR results for BPCC at this time. The magnetic field was applied along the b-axis and perpendicular to the ladder direction (a-axis), in the thermodynamic measurements field was applied along the ladder direction. The change in orientation means that $g_b \neq g$ and as such, new magnetisation values need to be calculated.

7.2.2.1 Determination of magnetisation

The effective magnetisation where neutron spectroscopy measurements were done can be determined by three different methods, which are summarised below:

Determination by excitation minima

[a] Rotations of the sample about the ψ angle

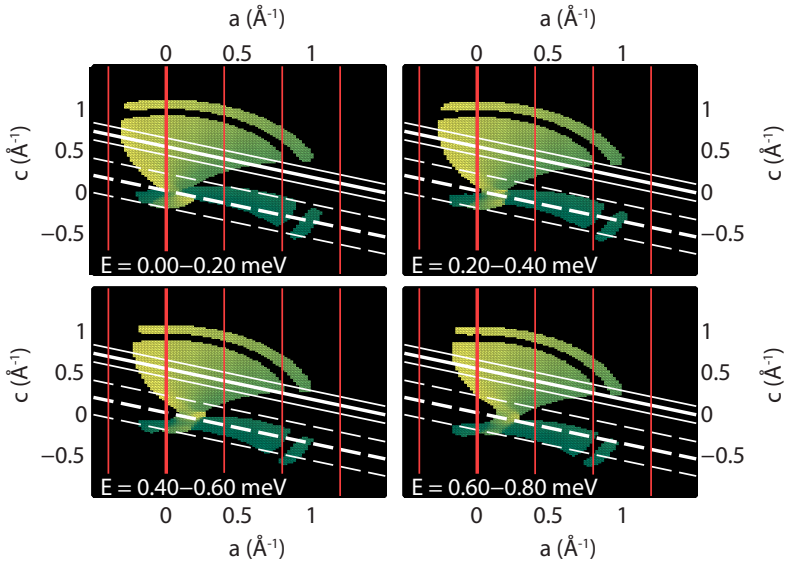

Figure 7.6: Momentum coverage for a selection of energy transfers on the LET. Coverage is shown as a coloured regions, where the two sets of sweeps cover the π and 0 sectors, solid and dashed thick white lines respectively. Thin white lines correspond to proposed integration ranges. Vertical red lines correspond to half Brillouin zones in Q_h, with the thick representing the gamma point.

As described previously, the incommensurate points on both the high and low energy excitations move with magnetisation. The positions of these minima can be used to determine the magnetisation value. In the π sector these points are at $\pi\,(1 - m^z)$, $\pi\,(1 + m^z)$ and in the 0 sector at πm^z, $\pi\,(2 - m^z)$. Determination of these points in the low energy sector is impossible due to the incoherent elastic scattering from the sample. The accuracy of the minima in the high energy sector is purely determined by experimental resolution.

Determination from the ferromagnetic phase

The determination of the exchanges and the g factor for this orientation was discussed in section 5.2.3. By simultaneously fitting the ferromagnetic dispersion at a known field, it is possible to determine the relative field above H_c and as such the g-factor.

Comparison with DMRG results

The exchange parameters in BPCC are well known due to the multiple experiments performed on the material. DMRG calculations are performed for specific magnetisation values, independent of applied field. As such, by comparisons of sets of simulations to experimental data it is possible to estimate the magnetisation and the g required. Particularly useful are the high energy excitations at momentum Q_h=0 in the π sector of the $S^{\pm}$ correlation and $Q_h = \pi$ in the 0 sector of the S^{zz} correlation as the excitation energy at these points is mostly controlled by the Zeeman effect and is linear with field.

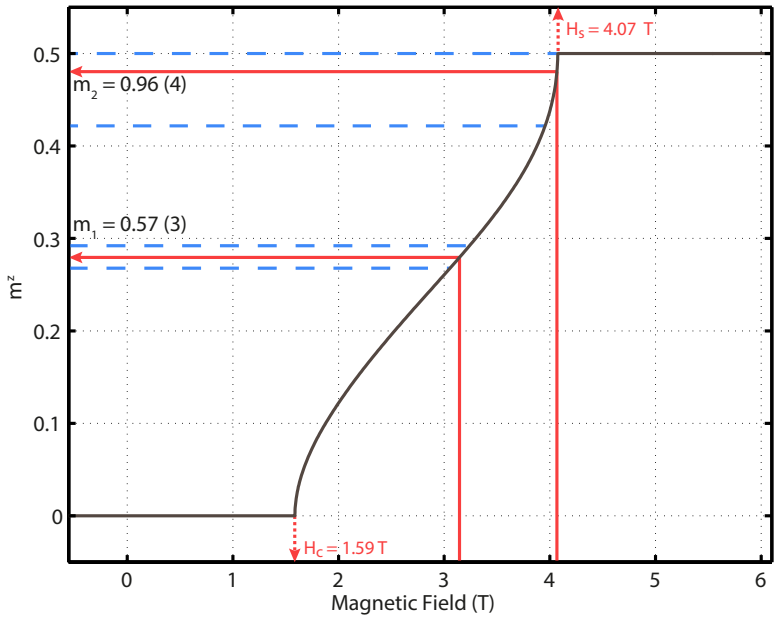

Figure 7.7: Zero temperature magnetisation curve for BPCC with the magnetic field along the b-axis. Red lines correspond to field values and the corresponding magnetisation and critical points as summarised in table 7.1. Errors on the magnetisation for H_1 and H_2 are shown as dotted blue lines. The derivation of these lines is described in the text.

As shown in section 5.3, by simultaneously fitting the dispersion in the field-induced ferromagnetic phase we obtained a g-factor of $g = 2.16$. The experimental magnetisation curve for BPCC was measured and presented in section 4.3 and a corresponding magnetisation curve from DMRG simulations is obtained. Since the g-factor acts as scaling the field, it is possible to rescale the DMRG curve. I.e. from

the g-factor of 2.06 along the a-axis to the appropriate value along b-axis. The scaled magnetisation curve for $T = 0$ is shown in figure 7.7.

By considering errors from the exchange and g-factor determination, the magnetisation values at which the spectrum was measured are given in table 7.1.

Field (T)	Magnetisation value	Alias
0	0	ZF
1.59	0	H_c
3.154	0.57 (3)	H_1
4.067	0.96 (4)	H_2
4.07	1	H_s

Table 7.1: [Magnetic field values for applied magnetic fields in BPCC]Magnetic field and corresponding magnetisation values in BPCC. Values given have been found through the process described in the text.

At the point H_1 the gradient of magnetisation is the smallest. At the critical points the magnetisation behaves like a square-root power law, and as such rapidly changes with field [130]. At H_2 the uncertainty in magnetisation is maximised and as such the precise magnetisation is more difficult to determine.

The excitation spectra are calculated at the magnetisation values given in table 7.1 and in the following section excitation energies will be compared with the experiential data to confirm the measured magnetisation values.

7.2.2.2 Integration and cuts of experimental and numerical data

When pixel and energy binned data from the instrument are converted into reciprocal lattice units and energy transfer it is possible to use equation 7.6 and DMRG simulations to calculate a theoretical intensity at each measured point. The simulation has a coverage which is identical to the experiential data. The simulated dataset can be treated in exactly the same way as the experimental data. An obvious advantage of working with the detector pixel information is that simulated intensities when integrated will be directly comparable to those measured in the experiment.

The $BPCBC_x$ series shares a monoclinic spacegroup and ToF codes such as Horace which project onto orthogonal axes need to be carefully used. In the experimental geometry with the ac-plane horizontal out-of-plane scattering corresponds to the b^*-axis, is non-dispersive and intensity can be integrated along the length of the detector tubes. The data can be cut in the ac-plane, separating the π and 0 sectors. Selecting a sector is achieved by equation 5.12 and an integration range in Q_l which results in sector selection and improved signal to noise.

7.2.2.3 Excitation spectra at H_1 and H_2

The excitations spectra for BPCC measured at magnetic field values H_1 and H_2 in the spin Luttinger-liquid phase are shown in figures 7.8 and 7.9. The excitation spectra will be explained along with reference to the theoretical results from DMRG.

To extract the excitations in the π and 0 sectors, cuts to the data along the paths shown in figure 7.6 have been performed with an integration width of ± 0.15 and ± 0.4 reciprocal lattice units in Q_l. These integration ranges have been chosen as they result in the optimum signal/noise ratio.

In the figures 7.8 and 7.9 the region dominated by the elastic scattering is shown as dark red. Additional scattering from elastic events within the magnet cause an inelastic $|\mathbf{Q}|$ dependant tail which is also present and covered in most cases. Removing this contamination by standard fitting methods leads to over-subtraction of the elastic line, affecting the excitations in the gapless regime and also the high energy excitations. For these reasons un-substituted data is presented.

Data taken at H_1 which corresponds to $m = 0.56$ is shown in figure 7.8 for both sectors. On the left is a full excitation period and a crop view of a half period is shown on the right. In all figures experiential data is shown in the left panel and the accompanying DMRG simulations are on the right. Simulations are reflected about the central axis.

π sector

Low energy excitations

The low energy continuum excitations from $S_{\pi}^{\pm\mp}$ are mostly covered by the elastic line, only visible at $Q_h \approx 0.25$ (shown by arrow 3) which is where they extend is highest in energy with most intensity. The cusps in the gapless excitations which are characteristic of the LL phase can not be resolved.

High energy excitations

Between 0.25 and 0.6 meV are excitations $|s\rangle \rightarrow |t^0\rangle$ from S^{zz} corresponding to an energy of approximately h^z (shown by arrow 2). The majority of spectral weight is concentrated around the 2π point with an energy of 0.32 meV. The excitation is incommensurate at approximately $Q_h = -0.28$, which is in

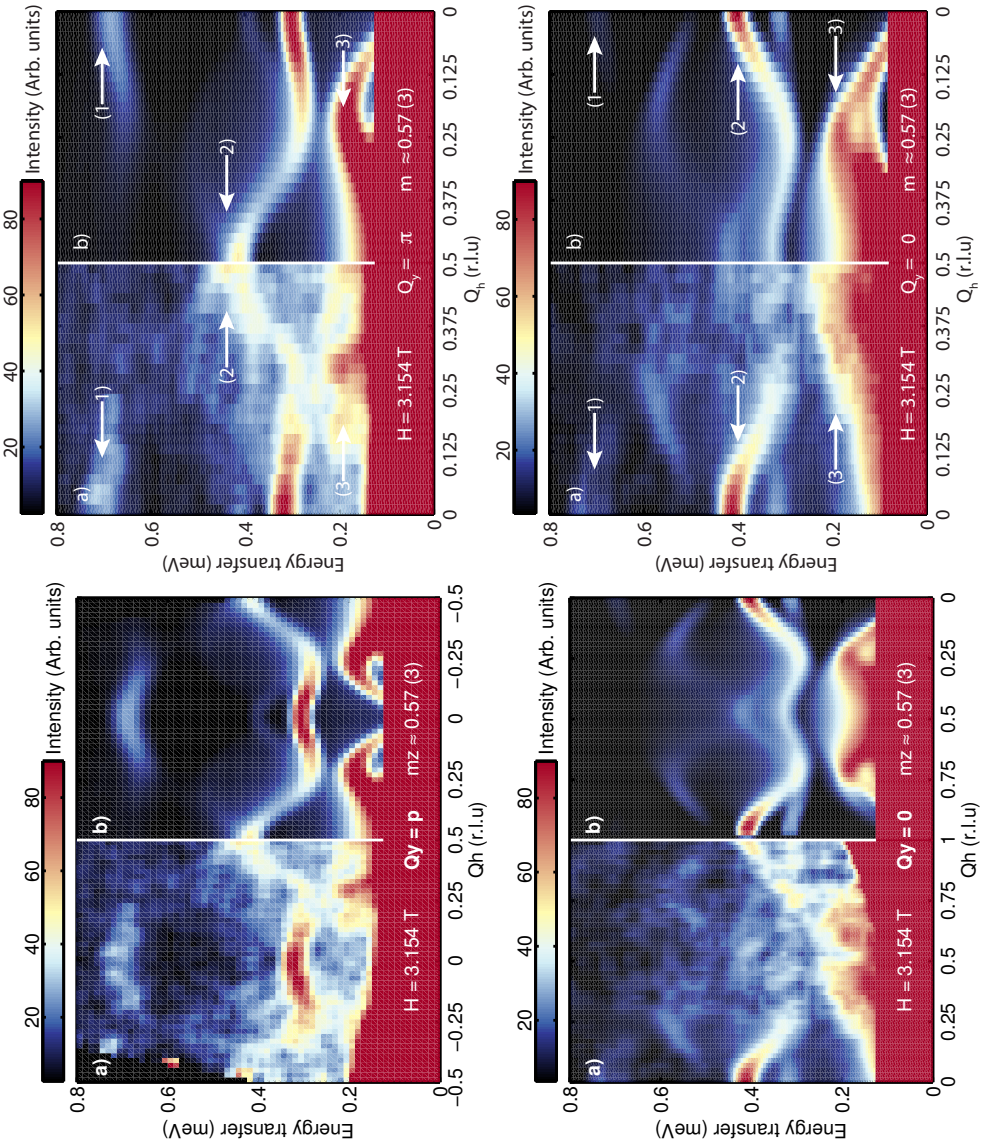

Figure 7.8: Excitations in the Luttinger-liquid phase of BPCC at $m = 0.57$. Top panels show data in the π sector, bottom panels show data in the 0 sector. Experimental data is presented in sub panels a) and simulations by DMRG are presented in panel b) with the main points labelled with arrows and described in the text. Data extraction methods and information about simulations are also described in the text.

agreement with the expected value of 0.29 from a magnetisation of 0.57. A clear continuum is visible in the spectrum, where the lower and upper edges can be approximated from the t-J model. At $Q_h = 0$ and 0.4 meV slight contamination from the 0 sector is visible. At 0.7 meV the excitations $|s\rangle \rightarrow |t^-\rangle$ from $S^{\pm}$ are visible, with spectral weight concentrated at the Brillouin zone boundary (shown by arrow 1).

0 **sector**

Low energy excitations

For the entire period shown in figure 7.8 (Bottom) signal to noise rapidly decreases with Q_h. This is predominantly due to a lack of angular coverage in Horace scans, resulting in a wider spacing in Q and hence smaller pixel density. The low-energy excitations suffer from the same limitations by the elastic line as in the π sector, but the low energy S^{zz} excitation is visible at $Q_h = 0.5$, terminating at 0.2 meV (shown by arrow 3).

High energy excitations

The high energy excitations $|t^+\rangle \rightarrow |t^0\rangle$ in the $S^{\pm}$ channel have spectral weight concentrated at the Brillouin zone boundary with an energy of $\approx h^z$. At the zone boundary this is 0.4 meV, and shows the effect of H_{s-h}, the triplet repulsion energy. Due to the larger integration width in momentum the contributions from S^{zz}_{π} and $S^{\pm}_{\pi}$ are more visible. This is especially noticeable for the high energy $S^{\pm}_{\pi}$ channel. In the 0 sector inter-triplet excitations such as $\frac{1}{\sqrt{2}}\left(|t^0\rangle |t^+\rangle - |t^+\rangle |t^0\rangle\right)$ at energy h^z (shown by arrow 2) and $\frac{1}{\sqrt{2}}\left(|t^+\rangle |t^-\rangle - |t^-\rangle |t^+\rangle\right)$ at $2h^z$ (shown by arrow 1) etc. can occur. The spectral weight of these excitations decreases rapidly away from the antiferromagnetic zone centre and cannot be seen. As in the π sector the gapped incommensurate excitation minima is consistent with a magnetisation of $m = 0.57$.

Similarly figure 7.9 shows the same cuts at $m = 0.96$. The spectrum has evolved to that of a ferromagnetic spin-wave dispersion. In the π sector, figure 7.9 (Top) spectral weight of high energy excitations is drastically reduced due to low singlet density. Low energy excitations corresponding to excitations for $S^{\pm}$, particu-

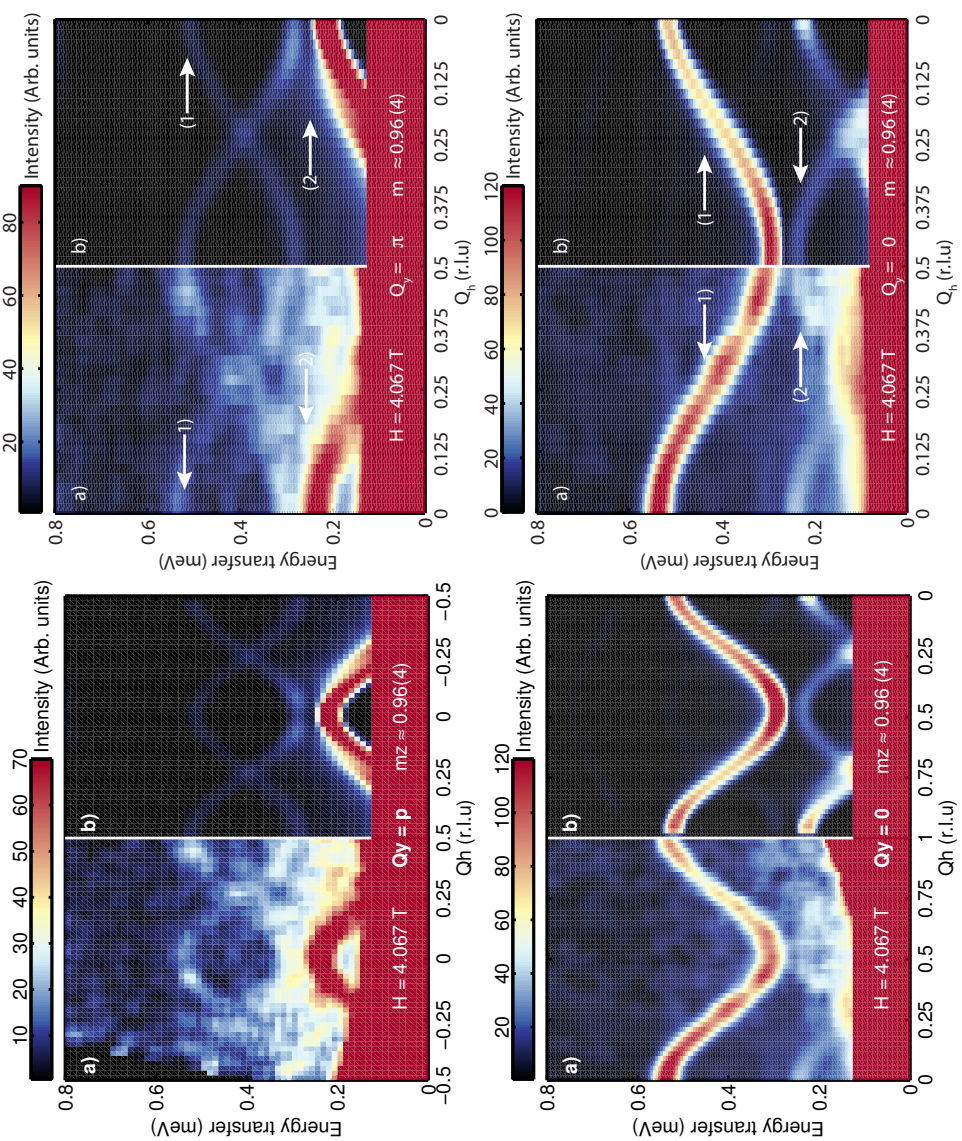

Figure 7.9: Excitations in the Luttinger-liquid phase of BPCC at $m = 0.96$. Top panels show data in the π sector, bottom panels show data in the 0 sector. Experimental data is presented in sub panels a) and simulations by DMRG are presented in panel b) with the main points labeled with arrows and described in the text. Data extraction methods and information about simulations are also described in the text.

larly $|t^+\rangle \rightarrow |s\rangle$ dominate and are clearly visible, extending from the elastic line to 0.22 meV (shown by arrow 1).

In the 0 sector the spectral weight is much greater due to high triplet density. The low-energy excitations are dominated by excitations within the $|t^+\rangle$ state. High-energy excitations are from $|t^+\rangle \rightarrow |t^0\rangle$ (shown by arrow 2). Higher energy excitations are above 0.8 meV and are not shown.

Due to the overwhelming spectral weight of the $S^{\pm}_{\pi}$ and $S^{\pm}_{0}$ excitations extracting the sectors using the same integration range in momentum shows contributions from the other parity states. However this is accurately captured in the simulations.

7.2.3 Conclusions

The excitation spectra of BPCC has been measured at magnetic fields corresponding to magnetisations of $m = 0.57$ and $m = 0.96$. The collective excitations of the Luttinger-liquid phase are visible in two excitation sectors, corresponding to odd and even parity excitations. Excitations at low energy have been partially obscured by the incoherent elastic scattering from the sample. At high energy clean excitation spectra are observed in figures 7.8-7.9.

High energy excitations from in the LL can be described by a t-J Hamiltonian, equation 7.3. Spin charge separation leads to an excitation continuum which has been observed in precise detail. The minima in observed scattering are incommensurate about points corresponding to the magnetisation value. At higher energies excitations from the singlet to t^- triplet states are also visible. These features are shown in figure 7.8.

At magnetisations approaching saturation the excitation spectra begin to form well defined bands as shown figure 7.9 and show a spin wave dispersion as described in section 5.2.3. The magnetisation and exchange parameters determined using the ferromagnetic phase have been used for numerical calculations.

DMRG has been used with exchange parameters given section 5.3 to calculate the full excitation spectra for $m = 0.57$ and $m = 0.96$. These simulations have been put into an experimental context as shown in figures 7.8-7.9. There is excellent quantitative agreement between the experimental and numerical simulations. All observed experimental features have been reproduced including spectral intensities.

We have found that BPCC is an ideal quantum simulator for spin Luttinger-liquid physics as described in reference [131]. The ability to access all correlation functions and the unique Luttinger-liquid parameter allowing for the study of exotic one dimensional physics.

7.3 BPCB - Spin incoherence in the Luttinger-liquid phase

Spin Luttinger-liquids (LL) are a peculiarity of one-dimensional interacting systems and are not unique to spin ladder compounds. Carbon nano-tubes [132, 118] and quantum wires [133] have been shown to exhibit Luttinger-liquid phases and have been studied in detail.

The collective excitations in the spin LL are spinons and holons as described in the $t-J$ model introduced in section 7.1.3. These carry spin and charge degrees of freedom respectively, each travelling at their own velocity. For low thermal energies the Hamiltonian is that of the spin Luttiger-liquid of equation 7.1. This can be re-written with the respective quasiparticle velocities (ν_s, ν_c), bosonic fields (θ_s, θ_c) and Luttinger-parameters (K_s, K_c). Hence the Hamiltonian is split into two parts,

$$\mathcal{H} = \mathcal{H}_c + \mathcal{H}_s. \tag{7.7}$$

Where $\mathcal{H}_c$ and $\mathcal{H}_s$ represent the charge and spin Hamiltonians;

$$\mathcal{H}_c = \hbar\nu_c \int \frac{dx}{2\pi} \left(\frac{1}{K_c} \left[\partial_x \theta_c(x)\right]^2 + K_c \left[\partial_x \phi_c(x)\right]^2 \right), \tag{7.8}$$

$$\mathcal{H}_s = \hbar\nu_s \int \frac{dx}{2\pi} \left(\frac{1}{K_s} \left[\partial_x \theta_s(x)\right]^2 + K_s \left[\partial_x \phi_s(x)\right]^2 \right). \tag{7.9}$$

We have shown in equation 7.3 that the high energy excitations in the spin Luttinger-liquid phase can be modelled by the $t-J$ Hamiltonian. For simplicity we will only consider the reduced Hamiltonian, neglecting triplet-triplet repulsion and energy offset term.

$$\mathcal{H}_{t-J} = -t \sum_{i=1,\sigma}^{L} \left(c_{i\sigma}^{\dagger} c_{i+1\sigma} + \text{H.c.} \right) + J \sum_{i=1}^{L} \left(\vec{S}_i \cdot \vec{S}_{i+1} - \frac{1}{4} n_i n_{i+1} \right). \tag{7.10}$$

There are two energy scales in the $t-J$ Hamiltonian. If we consider the $t = 0$ limit, the spins are governed by the Heisenberg interaction. For the limit $J = 0$ all spin states are degenerate and the dispersion, expressed by a simple cosine form $\omega(k) = -2t\cos(k)$., is that of a non-interacting band [134].

For finite values of J the degeneracy is lifted. This allows for spin effects to enter the dispersion by producing continuum scattering as shown in figure 7.3.

It is clear that spin and charge degrees of freedom are separate at all energies. This is justified by the single-particle Green's function for a Luttinger liquid,

$$G_{\sigma}^{LL}(x,\tau) \sim \frac{1/\sqrt{\nu_s\tau - ix}}{(x^2+\nu_c^2\tau^2)^{\gamma K_c}} \frac{e^{ik_F x}}{\sqrt{\nu_c\tau - ix}} + \text{c.c} \ . \tag{7.11}$$

Here x is the displacement of Fermions, τ is imaginary time and k_F is the Fermi velocity. Both the spin and charge degrees of freedom have coherent poles corresponding to spin and charge propagation.

Now we consider the energy scales in the Luttinger-liquid, those of spin (E_s) and charge (E_c) and the effect of temperature. It is common that E_s is small as particle exchanges are rare. This is due to the fact that particles must tunnel through each other when the interactions are strong [135]. When the temperature is such that $E_s << k_BT << E_c$, we have the interesting case of the suppression of the spin degree of freedom. Using the uncertainty principle we find that the coherence time for the spin exchange is less than that of the spin coherence time ($t_{coh} << t_{exch}$). The suppression of this degree of freedom is shown in the single-particle Green's function,

$$G_{\sigma}^{SILL}(x,\tau) \sim \frac{e^{-2k_F|x|(ln2/\pi)}}{(x^2+\nu_c^2\tau^2)^{\Delta K_c}} \frac{e^{i\left(2k_Fx+\psi_{K_c}^{+}\right)}}{\nu_c\tau - ix} + \text{c.c.} \tag{7.12}$$

The spinon velocity ν_s drops out of the Green's function and the resulting correlation functions do not depend on the behaviour of the spins. Since there is no non-trivial observable related to the spin in this regime, it is called spin incoherent.

Now the Green's function only depends on the holons. This leads to a reformation of a cosine-like band with periodicity $2k_F$ and implies a higher degree of universality than the Luttinger liquid.

In summary, the effect of temperature in the range $E_s << k_BT << E_c$ on the Luttinger liquid is to remove the spin degree of freedom, and introduce spin incoherence. In this regime the system is in a spin incoherent Luttinger-liquid (SILL) state which is more universal than that of the Luttinger-liquid.

The $t-J$ Hamiltonian (equation 7.3) can be solved by techniques such as DMRG which was used for the investigation of the LL phase in BPCC. The LL spectra of

BPCC have been calculated at $T = 0$, but for finite temperatures the calculation is challenging. One possible solution is to use Quantum Monte Carlo (QMC) simulations which are applicable at the temperatures needed, however the results are a statistical sampling. A new numerical method, time-dependent DMRG (tDMRG) addresses the limitations of DMRG and solves the Greens function in imaginary time at finite temperatures. The tDMRG technique is explained in references [136, 137]. Simulations presented in the following sections have been calculated by A. Feiguin (Northeastern University - Boston) in collaboration with F. Casola (ETH Zürich and Harvard).

7.3.1 Experimental setup

The triple-axis spectrometer IN14 (ILL - Grenoble) was used at $k_f = 1.3$ Å^{-1} in an optimised configuration and with a Be filter before the analyser. A 15 T cryomagnet with a dilution insert was used to reach base temperatures of 50 mK. The sample consisted of 6 co-aligned high quality deuterated BPCB crystals with a total mass of 1.4g . Instrumental slits were adjusted to optimise signal-to-noise ratio. In all cases energy scans were performed at the structure factor maximum in the π sector (S_π^{tot}, see figure 7.8). Due to the inability to distinguish the excitation channels, all excitations from S_π^{zz} and $S_\pi^{\pm\mp}$ were present. In the t-J model excitations corresponding to the S_π^{zz} channel for a spin ladder can be calculated. Excitations from the $S_\pi^{\pm\mp}$ channels have been subtracted through a process described below.

Base temperature and three other temperatures were chosen to observe the SILL, T = $J_l/3$, $2J_l/3$ and J_l. For BPCB the leg exchange is approximately 3.4-3.6 K, meaning data was taken at T = 60 mK, 1.2 K, 2.4 K, 3.6 K. Measurements were performed whilst still in dilution mode thanks to the implementation of a weak thermal link.

7.3.2 Analysis and theoretical comparisons

At base temperature the excitation spectrum for S_π^{tot} at half magnetisation in BPCB resemble that of BPCC shown in figure 7.8. Temperature effects on the low energy excitations of $S_\pi^{\pm\mp}$ have similar effects as described in work on critical scaling in KCuCl3 [138], where the spinon continuum becomes highly diffuse. The scattering

arising from the low energy $S_{\pi}^{\pm\mp}$ excitations has been subtracted from the experiential data by applying a temperature dependent scaling and broadening function to the exact spinon dispersion given by J. S. Caux *et al.* in [139]. The high energy $|s\rangle \rightarrow |t^{-}\rangle$ excitations in $S_{\pi}^{\pm}$ are at approximately 1.8 meV and the effect of temperature on these excitations is unknown. They were subtracted by a broad Gaussian function. All simulations are scaled to the experimental data by a universal factor. This factor is derived from the mean of all individually refined multiplication factors taken from the $Q_h = 1$ point.

After background subtraction the resulting data are shown in the colour maps of figure 7.10. In all panels data consisting of 5 equally spaced energy scans are shown in the left panel and the corresponding tDMRG simulation which has been convolved with the experiential resolution and interpolated to the same level as the data is shown in the right panels.

At base temperature, figure 7.10 (Left top) the S_{π}^{zz} excitation is that of a classical LL as described in section 7.2. The dispersion occurs at higher energy above the gap, with the majority of intensity occurring between 1.1 and 1.4 meV and with an incommensurate minimum at approximately $Q_h = 0.75$. As described previously, this confirms half magnetisation within experimental accuracy. The detailed structure of the excitation from the spin degree of freedom can be seen above this. The simulation at T = 0 captures the detailed structure of the excitation and the continuum shape. Intensity around $Q_h = 0.625$ differs from the experimental data. Convolution with the experimental resolution is the most probable cause for this discrepancy as the calculated resolution ellipsoid may differ from that of the experiment. Convolution of the simulations is performed in Q_h and ω, whereas experimentally all 4 dimensions are convolved. Intensity around this point is expected to be miss calculated at all simulation temperatures.

On increasing the temperature to $J_l/3$, the intensity at $Q_h = 0.5$ is beginning to be redistributed and the excitation is becoming broader due to thermal effects. The condition $T << J_l$ is still true and as such the spin degree of freedom is still present, as shown by the excitation still being incommensurate and with substructure of the continuum. The comparison with the theoretical results in the right panel of figure 7.10 (Right top) shows that these features are indeed predicted and reproduced by

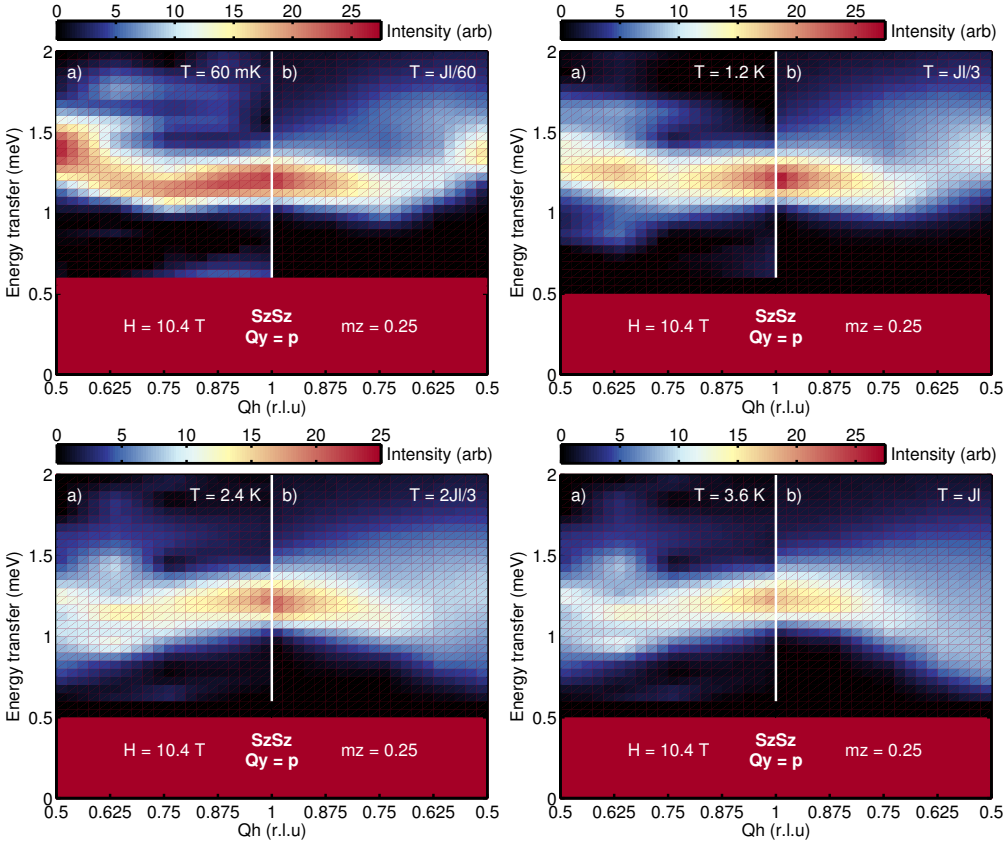

Figure 7.10: Temperature effects in the Luttinger-lquid phase of BPCB as measured by neutron scattering on IN14. For each panel a) corresponds to experimental measurements of the S^{zz}_{π} channel as described in the text and b) numerical simulations performed by tDMRG. Top left) base temperature spectrum with features as described in section 7.1.3. Top right) Excitation spectrum for T = $J_l/3$, (Bottom left) T = $2J_l/3$ and T = J_l (Bottom right). Spin incoherence is observed by a shift of the incommensurate point and the reformation of a cosine band at high temperatures.

tDMRG. The simulated intensity around $Q_h = 0.5$ is anomalous as expected.

At $T = 2J_l/3$ the incommensurate minimum is moved to $Q_h = 0.625$ and is beginning to shift to $Q_h = 0.5$. At $Q_h = 0.5$ the excitation has softened to 1.1 meV and the main intensity is nearly energy independent. The temperature is comparable with the characteristic spin energy E_s and as such the features of the base temperature LL excitation have been diminished and the cosine band of the charge excitation is becoming prevalent. The characteristic spectra is becoming broader and is loosing the defined substructure as shown in figure 7.10 (Left bottom).

Shown in figure 7.10 (Right bottom) is S^{zz}_{π} where the temperature equals the characteristic spin energy. The excitation has become fully commensurate with a lower boundary which resembles a cosine band. The excitation has some structure above the lower boundary, implying that the spin degree of freedom has yet to be fully excluded. At $Q_h = 0.5$, 0.75 and 1 the excitation widths are compatible to the simulation and are further investigated in figure 7.11

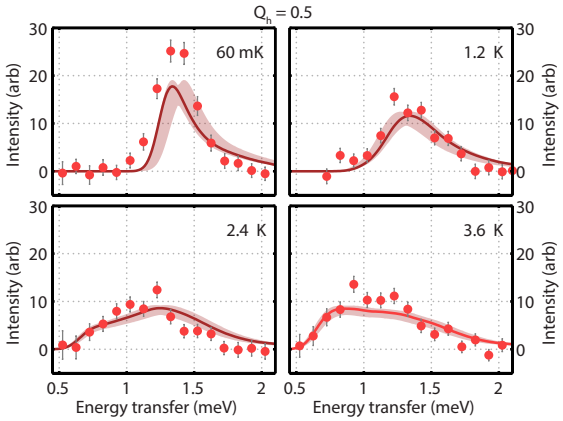

(i)

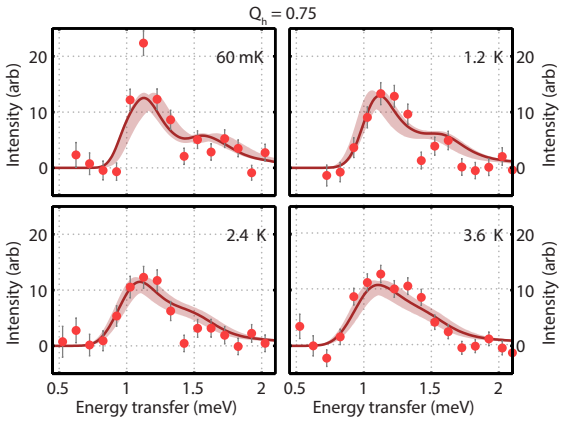

(ii)

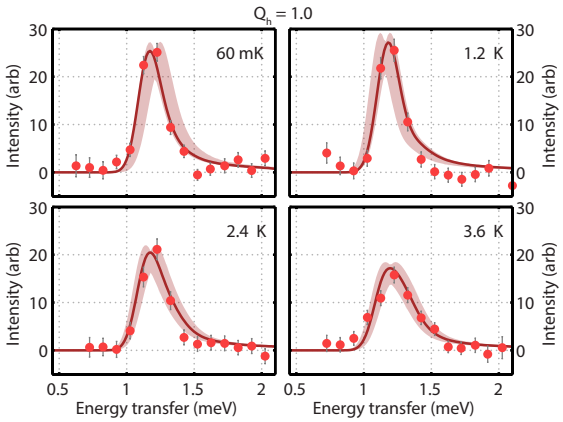

(iii)

Figure 7.11: Individual scans at $Q_h = 0.5$, 0.75 and 1 for all temperatures. Data points are shown as red filled circles and the dark red line the scaled simulation. Uncertainties in J_l, magnetisation and simulation scaling factor are combined in the light red region, highlighting a region of confidence for the simulation.

In figure 7.11 (Top) $Q_h = 0.5$ scans are shown, where the change in the excitation is the most pronounced. At base temperature the excitation is sharp at 1.4 meV. With increased temperature this softens to 0.7 meV with structure extending to 1.8 meV. The scattering line shape is accurately captured in the simulation and for the highest temperature, where deviations between theory and experiment are very small. Similar results are present for $Q_h = 0.75$ and at $Q_h = 1.0$ there is exceptional agreement.

7.3.3 Conclusions

The spin ladder material BPCB has been shown to exhibit spin incoherent Luttinger-liquid behaviour at half magnetisation. The base temperature spectrum for an ideal Luttinger-liquid is shown for BPCC in section 7.1.3 and for BPCB in figure 7.10 (Top left). In both cases an incommensurate excitation with a detailed continuum is observed.

At finite temperatures the spin component of the Hamiltonian given in equation 7.10 becomes incoherent. The spin incoherence in a Luttinger-liquid has a profound effect on the excitation spectrum, as the spin degree of freedom is suppressed and the charge degree of freedom becomes dominant.

The effect of finite temperatures on the Luttinger-liquid phase is described in panels of figure 7.10. As temperature is increased spectral weight is redistributed and the incommensurate minima shifts to the π point. The behaviour is in excellent agreement with the theoretical predictions introduced in section 7.3. The effect of temperature on the Luttinger-liquid spectrum have been studied by our collaborator A. Feiguin by the tDMRG technique in reference [134].

Simulations by tDMRG using the Hamiltonian given in equation 7.10 and exchange parameters from the zero field experiential data have been used to calculate the spectrum for the S^{zz}_{π} channel. Direct comparisons to the data are shown in figure 7.11 using the data analysis technique detailed in section 7.3.2. An exceptional agreement is obtained between theory and experiment, where the simulations range of validity encompass most data points.

We conclude that the spin ladder material BPCB exhibits spin incoherent Luttinger-liquid features which are consistent with theoretical predictions. With

the absence of the spin degree of freedom, the SILL phase is a lower universality class than the Luttinger-liquid.

Chapter 8

Conclusions and outlook

In this thesis the following objectives and questions were posed; Finding new model compounds which exhibit the spin ladder structure with exchange ratios which bridge the gap between the strong and weak coupling limit. The effects of bond disorder on a model spin ladder compound and the measurement and analysis of collective excitations in the spin coherent and incoherent Luttinger-liquid phase. The answers to these questions are addressed below.

The discovery of new spin ladder material with exotic properties.

For this thesis high quality single crystals of BPCC have been synthesised. Measurements by thermodynamics (section 4.3), magnetic susceptibility (section 4.2.1) and neutron scattering (section 5.2) have confirmed the spin Hamiltonian and associated exchange parameters. The exchange parameters have been found to be $J_r = 3.41(1)$ K and $J_l = 1.39(1)$ K with negligible inter-ladder coupling. The exchange ratio in BPCC is 2.45, which is closer to the goal of $\gamma = 1$. It has been found that the one magnon excitation can be accurately described by perturbation theory with a structure factor which can be described by the single mode approximation.

The analysis of magnetic susceptibility measurements has provided a procedure to detect and determine the exchanges in spin ladder compounds. This procedure has been used for other spin ladder candidate compounds . In the outlook below we demonstrate this with a pyrazine compound, which are excellent candidate materials for $\gamma \to 1$.

The effect of bond disorder on a model spin ladder system.

Bond disorder has been studied in $BPCBC_x$ compounds by magnetic susceptibility and neutron scattering. The crystal structure for the series has been

determined and it has been found that there are no phase transitions and the spin ladder magnetic structure is retained.

The average magnetic exchanges for the series have been determined (table 4.5) and show a smooth transition between the limiting pure cases. In $BPCBC_{0.1}$ the excitation spectrum has been studied and a one magnon excitation with an anomalous line-shape observed. The anomalous line-shape can be interpreted as coherent excitations from disordered sections of ladder with different exchange parameters. Evidence for a localised in-gap mode is also present. The analysis of the anomalous line-shape has led to the development of a random exchange spin ladder model which has been solved by exact diagonalisation and compares favourably with the data. Optimisations of this description are ongoing.

Excitations in the spin Luttinger-liquid phase and the effect of temperature.

The spin Luttinger-liquid phase of the spin ladder has been investigated in BPCC by neutron scattering. The complex high energy excitations in this phase have been measured and the fractionalization of the elementary quasiparticle excitations observed. The characteristic excitation continua have been explained by effective spin-chain and t-J models and DMRG calculations using the aforementioned exchange parameters. We observe remarkable quantitative agreement between the data and simulation. Temperature effects on this phase have also been investigated and it has been found that spin incoherent Luttinger-liquid physics is present and the universality class is raised.

These points have been addressed in references [131] and [46] with a further 3 papers in preparation. These will cover results pertaining to the Hamiltonian of BPCC, covering the dispersion and exchange parameters to be presented in PRB. Excitations and disorder effects in a random bond spin ladder material for PRL and a complete study of the spin Luttinger-liquid phase of an ideal ladder and spin incoherence on increased temperatures.

8.1 Further investigations on BPCC

The spin ladder compound BPCC is an exceptional model spin ladder material and as such is a playground for investigating low-dimensional quantum magnetism. The following sections detail additional work which has interesting open questions that can be studied by this exceptional material.

8.1.1 Universal scaling through quantum criticality

Universal scaling has been studied in BPCC at the quantum critical points H_c and H_s in thermodynamic measurements. The nature of interactions at the quantum critical points are of immense interest and are technically challenging to explore.

Theory predicts that in spin ladder systems there is universal scaling in the spin Luttinger-liquid phase, particularly around the antiferromagnetic zone center (AFZC). The low energy excitations in the $S^{\pm\mp}_{\pi}$ sector at half magnetisation exhibit universal scaling as described by S. Sachdev *et al.* in reference [140]. The intensity of the $S^{+-}(k,\omega)$ excitation is ultimately described by the imaginary part of the Green's function G^R_L which in the Luttinger Liquid regime depends on the scaling function $A_L\left(\bar{\omega},\bar{k}\right)$. For the energies below the depth of the Fermi-sea:

$$A_L\left(\imath\bar{\omega},\bar{k}\right) = \frac{\pi^{\eta-1}\,\Gamma\left(1-\frac{\eta}{2}\right)\,\Gamma\left(\frac{\eta}{4}+\frac{|\bar{\omega}|+\imath\bar{k}}{4\pi}\right)\,\Gamma\left(\frac{\eta}{4}+\frac{|\bar{\omega}|-\imath\bar{k}}{4\pi}\right)}{2^{2-\eta}\,\Gamma\left(\frac{\eta}{2}\right)\,\Gamma\left(1-\frac{\eta}{4}+\frac{|\bar{\omega}|+\imath\bar{k}}{4\pi}\right)\,\Gamma\left(1-\frac{\eta}{4}+\frac{|\bar{\omega}|-\imath\bar{k}}{4\pi}\right)}, \tag{8.1}$$

where $\bar{w} = \frac{\hbar\omega}{k_B T}$ and $\bar{k} = \frac{\hbar c k}{k_B T}$. This is valid across the LL regime ($\eta = 1/2$) where the magnetisation determines the spinon velocity c. Similar work on the spin chain compound $KCuF_3$ has been performed by B. Lake *et al.* which corresponds to spin ladders at half effective magnetisation [138]. Recently critical scaling in the LL regime has been investigated on the spin ladder material DIMPY at low magnetisation [141]. BPCC has the advantage over DIMPY that the full phase diagram is available, so scaling can be tested for multiple spinon velocities, however the energy scales at which scaling occurs are experimentally difficult to achieve for BPCC.

For BPCC the temperature evolution of the spinon excitations are shown in figure 8.2 for T = 0, $J_l/2$, J_l based on equation 8.1.

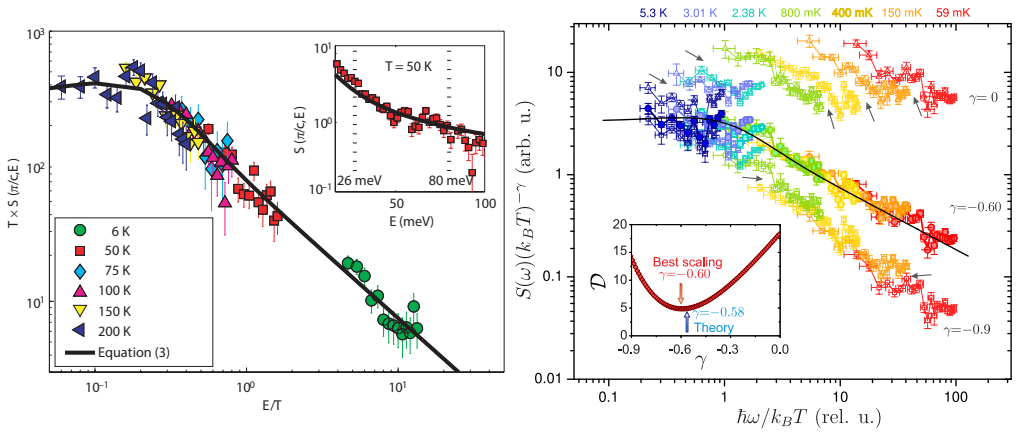

(i) (ii)

Figure 8.1: Universal scaling for the spin ladder DIMPY and spin chain compound $KCuF_3$ and the applicability of finction 8.1 . Left) Data taken at various temperatures showing scaling around the AFZC in the spin chain compound $KCuF_3$ taken from reference [138]. Right) Data taken on the strong leg spin ladder material DIMPY showing scaling and the determination of the scaling parameter. Taken from reference [141].

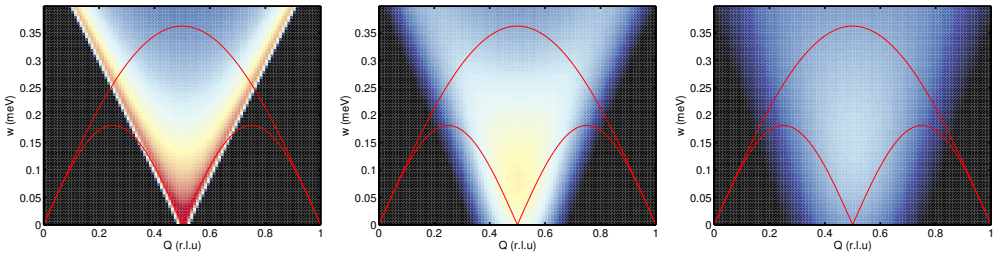

Figure 8.2: Scaling predictions for BPCC in the spin Luttinger-liquid phase base on equation 8.1. The colour maps show the intensity of the $S^{\pm\mp}_{Qy}$ secors at half magnetisation. Panels from left to right show temperatures T = 0, T = $J_l/2$ and T = J_l.

8.1.2 Spin incoherence in the Luttinger Liquid phase

Here we propose to redo the experiment introduced in section 7.3.2 on the high-resolution, low-energy transfer spectrometer LET. The result on the excitations in the spin Luttinger-liquid phase of BPCC in section 7.2 demonstrated that com-

plex spectra can be accurately captured on high-resolution chopper spectrometers. Spectra collected on BPCB for each temperature at half magnetisation using IN14 consisted of 5 q values, but do not have the exceptional details of the work in section 7.2.

The limitations in maximum magnetic field for LET require using BPCC instead of BPCB as the critical fields of the former are attainable in the custom 9T cryomagnet. This means that the entire phase diagram will be open to exploration in exceptional detail and both the π and 0 sectors will be accessible for analysis.

8.1.3 Completing the Luttinger-liquid phase

Excitations in the spin Luttinger phase have been measured at m = 0.56 and m = 0.96 in section 7.2. The low energy excitation spectra of a spin ladder at m = 0.75 and 0.25 are equally interesting with a shift in spectral weight from the π to the 0 sector and a field-induced continuous change of the spinon continua. Further a measurement at m = 0.75 for both high and low energy excitation allows for verification of the magnetisation determination presented in section 7.2 and for a complete verification of the evolution of the excitation dynamics with field.

8.2 Exchange determination in complex spin systems

BPCB and BPCC are both characterised as spin ladders in the strong coupling limit where J_r is greater than J_l . There is great interest in finding ladder materials where the coupling ratio approaches unity ($J_r/J_l \approx 1$) or even goes to the weak coupling limit. In this limit the physics of the system can neither be described as weakly coupled dimers or weakly coupled chains. The spin gap Δ which is present for a finite rung exchange was first expected to uniformly decrease to zero as J_r is decreased [76]. However, it has been observed that power law decay of the spin correlations lead the spin chain ($J_r = 0$) to be in a critical state [142]. Hence small perturbations lead to drastic changes in the physics of spin ladders [143].

The search for compounds which exhibit a spin ladder structure often leads to the discovery of non-ideal systems. To find low energy spin ladder materials with negligible inter-ladder exchange and without other interactions such as the

Dzyaloshinskii-Moriya interaction and a specific coupling ratio is very rare. The search for ideal spin ladder compounds with low coupling ratios is an interesting examination of the breakdown of the strong coupling limit. The search for compounds with a low coupling ratio is currently being performed by Ch. Fiolka (University of Bern). A couple of possible spin ladder candidates have already been found and susceptibility measurements taken. One of these compounds is $(Cu(H_2O)(Cl\text{-}dipic))_2pyz$, the structure of which is shown in figure 8.3. Pyrazine based compounds have been shown to be excellent starting materials for low dimensional physics[144] as anions and cations can be readily replaced, modifying exchange pathways and changing dimensionality. The exact diagonalisation technique described in chapter has been used to extract the exchange interactions with the best fit shown in figure 8.3.

The fitted exchange interactions in this material are $J_r = 6.8 \pm 0.05$ K, $J_l = 2 \pm 0.05$ K. Hence the coupling ratio of 3.4 is obtained. This is close to the ratio of BPCB (≈ 3.5). The dynamical flexibility allows that the structure of this material can be modified so that the coupling ratio can be reduced.

When this fitting technique was applied to other possible spin ladder compounds evidence of non-ideal behaviour was found. The typical χ^2 distribution for an ideal ladder (in J_r and J_l parameter space) is well described by a Gaussian-skew distribution. Other compounds measured showed a broad distribution of χ^2 in J_r and J_l space, suggesting an incorrect spin model. Motivated by this result and observations of the crystal structure it is postulated that one of these new materials is a zig-zag ladder, combining the interesting effects of low dimensionality with spin frustration.

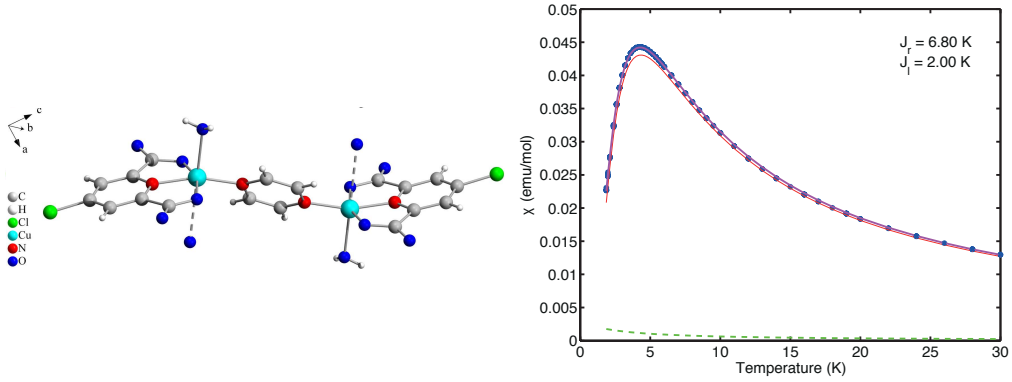

Figure 8.3: A new spin ladder compound and exchange parameter determination. The crystal structure of $(Cu(H_2O)(Cl\text{-}dipic))_2pyz$ is shown (Left) where the unit shown is repeated along the c-axis. Magnetic susceptibility data is shown (Right) where the blue points represent data with the diamagnetic contribution removed, the red line is the best simulation data and the green dashed line is the Curie-Weiss contribution. The purple line is the total best fit. Extracted exchange parameters are $J_r = 6.8 \pm 0.05$ K, $J_l = 2 \pm 0.05$ K

Appendices

Appendix A

Refined crystal structure of the $(C_5D_{12}N)_2CuBr_{4(1-x)}Cl_{4x}$ series

Table A.1: Fullprof refinement of atomic positions $(C_5D_{12}N)_2CuBr_4$ for data acquired at 1.8 K. Unit cell parameters are a = 8.37071Å, b = 16.93945Å, c = 12.38182Å, $\alpha = 90°$, $\beta = 101.19960°$, $\gamma = 90°$, Spacegroup = P21/c

Atom	**x**	**y**	**z**	**Occupation**
Cu	0.69551	0.08125	0.24050	1.000
Br1	0.70608	-0.04151	0.14963	1.000
Br2	0.94496	0.13533	0.20130	1.000
Br3	0.42066	0.11708	0.15897	1.000
Br4	0.70183	0.12696	0.42451	1.000
N11	0.28485	-0.07099	0.07111	1.000
D111	0.26260	-0.05629	-0.01173	1.000
D112	0.38025	-0.03731	0.09903	1.000
C12	0.14263	-0.04801	0.11837	1.000
D121	0.04059	-0.08675	0.07759	1.000
D122	0.11725	0.01498	0.10239	1.000
C13	0.18023	-0.07148	0.24024	1.000
D131	0.07763	-0.05314	0.27222	1.000
D132	0.26960	-0.03110	0.27929	1.000
C14	0.22905	-0.15489	0.26412	1.000
D141	0.26141	-0.16677	0.35293	1.000
D142	0.12541	-0.19336	0.22866	1.000
C15	0.37497	-0.17714	0.20714	1.000

Table A.1: (continued)

Atom	x	y	z	Occupation
D151	0.40251	-0.23945	0.22142	1.000
D152	0.47776	-0.14149	0.24895	1.000
C16	0.33779	-0.15420	0.08579	1.000
D161	0.23841	-0.19358	0.04502	1.000
D162	0.44111	-0.16232	0.04667	1.000
N21	0.28928	0.14594	0.39870	1.000
D211	0.18607	0.12945	0.33770	1.000
D212	0.39251	0.13704	0.36586	1.000
C22	0.27602	0.22726	0.43384	1.000
D221	0.27769	0.26442	0.36272	1.000
D222	0.38520	0.24070	0.48829	1.000
C23	0.13024	0.23995	0.48740	1.000
D231	0.13529	0.30030	0.51351	1.000
D232	0.01796	0.22831	0.42614	1.000
C24	0.12849	0.18153	0.58077	1.000
D241	0.23253	0.19524	0.64997	1.000
D242	0.02369	0.18862	0.61601	1.000
C25	0.14584	0.09836	0.54223	1.000
D251	0.15158	0.05482	0.60711	1.000
D252	0.03865	0.08219	0.48446	1.000
C26	0.29714	0.08538	0.49012	1.000
D261	0.40430	0.09887	0.54836	1.000
D262	0.30447	0.02645	0.46023	1.000

Table A.2: Fullprof refinement of atomic positions $(C_5D_{12}N)_2CuBr_{3.6}Cl_{0.4}$ for data acquired at 1.8 K. Unit cell parameters are a = 8.34491Å, b = 16.91968Å, c = 12.35999Å, $\alpha = 90°$, $\beta = 101.30080°$, $\gamma = 90°$, Spacegroup = P21/c

Atom	**x**	**y**	**z**	**Occupation**
Cu	0.69328	0.08103	0.24088	1.000
Br1	0.70284	-0.03843	0.14825	0.600
Cl1	-	-	-	0.400
Br2	0.94284	0.13575	0.20012	0.946
Cl2	-	-	-	0.035
Br3	0.41942	0.11562	0.16089	0.867
Cl3	-	-	-	0.133
Br4	0.70320	0.12751	0.42496	0.656
Cl4	-	-	-	0.344
N11	0.28830	-0.06951	0.07255	1.000
D111	0.25847	-0.05439	-0.00899	0.981
H111	-	-	-	0.019
D112	0.38177	-0.03391	0.10223	0.981
H112	-	-	-	0.019
C12	0.13619	-0.04858	0.11679	1.000
D121	0.03723	-0.08717	0.07772	0.981
H121	-	-	-	0.019
D122	0.11609	0.01833	0.10409	0.981
H122	-	-	-	0.019
C13	0.18457	-0.07126	0.24206	1.000
D131	0.07936	-0.05279	0.27188	0.981
H131	-	-	-	0.019
D132	0.26696	-0.03059	0.28187	0.981
H132	-	-	-	0.019
C14	0.22873	-0.15511	0.26582	1.000
D141	0.26260	-0.16933	0.35112	0.981
H141	-	-	-	0.019

Table A.2: (continued)

Atom	x	y	z	Occupation
D142	0.12730	-0.19352	0.22662	0.981
H142	-	-	-	0.019
C15	0.38062	-0.17622	0.20777	1.000
D151	0.40341	-0.23850	0.21568	0.981
H151	-	-	-	0.019
D152	0.48251	-0.14087	0.24892	0.981
H152	-	-	-	0.019
C16	0.33787	-0.15534	0.08498	1.000
D161	0.23777	-0.19243	0.04243	0.981
H161	-	-	-	0.019
D162	0.44650	-0.15944	0.04812	0.981
H162	-	-	-	0.019
N21	0.28835	0.14616	0.39860	1.000
D211	0.18356	0.12975	0.33806	0.981
H211	-	-	-	0.019
D212	0.39544	0.13644	0.36975	0.981
H212	-	-	-	0.019
C22	0.27659	0.22890	0.43269	1.000
D221	0.27883	0.26440	0.36327	0.981
H221	-	-	-	0.019
D222	0.38852	0.23785	0.48978	0.981
H222	-	-	-	0.019
C23	0.12535	0.24223	0.48685	1.000
D231	0.13974	0.30043	0.51811	0.981
H231	-	-	-	0.019
D232	0.01859	0.22714	0.42418	0.981
H232	-	-	-	0.019
C24	0.13195	0.17967	0.58155	1.000
D241	0.23221	0.19493	0.64809	0.981

Table A.2: (continued)

Atom	x	y	z	Occupation
H241	-	-	-	0.019
D242	0.02200	0.18882	0.61567	0.981
H242	-	-	-	0.019
C25	0.14418	0.09811	0.54482	1.000
D251	0.15218	0.05427	0.60813	0.981
H251	-	-	-	0.019
D252	0.03641	0.08214	0.48744	0.981
H252	-	-	-	0.019
C26	0.29608	0.08502	0.49010	1.000
D261	0.40623	0.09996	0.54911	0.981
H261	-	-	-	0.019
D262	0.30343	0.02444	0.46083	0.981
H262	-	-	-	0.019

Table A.3: Fullprof refinement of atomic positions $(C_5D_{12}N)_2CuBr_2Cl_2$ for data acquired at 1.8 K. Unit cell parameters are a = 8.23470Å, b = 16.79468Å, c = 12.26454Å, $\alpha = 90°$, $\beta = 101.66890°$, $\gamma = 90°$, Spacegroup = P21/c

Atom	**x**	**y**	**z**	**Occupation**
Cu	0.68938	0.08516	0.23991	1.000
Br1	0.70230	-0.03430	0.14914	0.194
Cl1	-	-	-	0.806
Br2	0.93981	0.13642	0.20357	0.587
Cl2	-	-	-	0.413
Br3	0.41703	0.11059	0.16673	0.569
Cl3	-	-	-	0.431
Br4	0.70623	0.12701	0.42002	0.458
Cl4	-	-	-	0.542
N11	0.29210	-0.06656	0.07346	1.000
D111	0.26029	-0.05198	-0.00178	0.984
H111	-	-	-	0.016
D112	0.37277	-0.02465	0.10351	0.984
H112	-	-	-	0.016
C12	0.13574	-0.04767	0.11450	1.000
D121	0.03394	-0.08754	0.07985	0.984
H121	-	-	-	0.016
D122	0.11379	0.01989	0.11246	0.984
H122	-	-	-	0.016
C13	0.18845	-0.07474	0.24588	1.000
D131	0.07692	-0.05647	0.27965	0.984
H131	-	-	-	0.016
D132	0.26215	-0.03191	0.27996	0.984
H132	-	-	-	0.016
C14	0.23457	-0.15536	0.26529	1.000
D141	0.25870	-0.16916	0.34622	0.984
H141	-	-	-	0.016

Table A.3: (continued)

Atom	x	y	z	Occupation
D142	0.13668	-0.20108	0.22386	0.984
H142	-	-	-	0.016
C15	0.37801	-0.17655	0.20342	1.000
D151	0.42080	-0.24053	0.21341	0.984
H151	-	-	-	0.016
D152	0.49057	-0.14055	0.24695	0.984
H152	-	-	-	0.016
C16	0.34449	-0.15422	0.08205	1.000
D161	0.24098	-0.18695	0.03967	0.984
H161	-	-	-	0.016
D162	0.45552	-0.15477	0.04460	0.984
H162	-	-	-	0.016
N21	0.28822	0.14547	0.40382	1.000
D211	0.18796	0.13013	0.33926	0.984
H211	-	-	-	0.016
D212	0.38574	0.14107	0.37129	0.984
H212	-	-	-	0.016
C22	0.27666	0.22315	0.43416	1.000
D221	0.27637	0.26615	0.36820	0.984
H221	-	-	-	0.016
D222	0.38582	0.24364	0.48663	0.984
H222	-	-	-	0.016
C23	0.12817	0.24321	0.49650	1.000
D231	0.13509	0.30602	0.51906	0.984
H231	-	-	-	0.016
D232	0.02071	0.22978	0.43328	0.984
H232	-	-	-	0.016
C24	0.12267	0.17733	0.58183	1.000
D241	0.23414	0.19381	0.64866	0.984

Table A.3: (continued)

Atom	x	y	z	Occupation
H241	-	-	-	0.016
D242	0.02335	0.19736	0.62220	0.984
H242	-	-	-	0.016
C25	0.14507	0.09752	0.54593	1.000
D251	0.15411	0.05705	0.60897	0.984
H251	-	-	-	0.016
D252	0.02739	0.07759	0.49052	0.984
H252	-	-	-	0.016
C26	0.30151	0.08339	0.49060	1.000
D261	0.41528	0.10185	0.55202	0.984
H261	-	-	-	0.016
D262	0.30728	0.02597	0.46279	0.984
H262	-	-	-	0.016

Table A.4: Fullprof refinement of atomic positions $(C_5D_{12}N)_2CuBr_{0.4}Cl_{3.6}$ for data acquired at 1.8 K. Unit cell parameters are a = 8.11780Å, b = 16.62282Å, c = 12.16973Å, $\alpha = 90°$, $\beta = 102.10440°$, $\gamma = 90°$, Spacegroup = P21/c

Atom	**x**	**y**	**z**	**Occupation**
Cu	0.69043	0.08464	0.24109	1.000
Br1	0.70377	-0.03220	0.15251	0.041
Cl1	-	-	-	0.959
Br2	0.94024	0.13382	0.20899	0.114
Cl2	-	-	-	0.886
Br3	0.41857	0.11681	0.16677	0.139
Cl3	-	-	-	0.861
Br4	0.69836	0.12584	0.41782	0.151
Cl4	-	-	-	0.849
N11	0.28476	-0.06421	0.07234	1.000
D111	0.25752	-0.04446	-0.00578	0.981
H111	-	-	-	0.019
D112	0.38212	-0.02542	0.10677	0.981
H112	-	-	-	0.019
C12	0.13962	-0.04662	0.12505	1.000
D121	0.03451	-0.08247	0.08113	0.981
H121	-	-	-	0.019
D122	0.10760	0.01746	0.11536	0.981
H122	-	-	-	0.019
C13	0.18418	-0.07106	0.25181	1.000
D131	0.07219	-0.05783	0.28453	0.981
H131	-	-	-	0.019
D132	0.28660	-0.03001	0.29106	0.981
H132	-	-	-	0.019
C14	0.24043	-0.15669	0.26658	1.000
D141	0.28456	-0.17081	0.35238	0.981
H141	-	-	-	0.019

Table A.4: (continued)

Atom	x	y	z	Occupation
D142	0.13496	-0.19731	0.22948	0.981
H142	-	-	-	0.019
C15	0.38715	-0.17088	0.20230	1.000
D151	0.42629	-0.23703	0.21747	0.981
H151	-	-	-	0.019
D152	0.49917	-0.13932	0.24638	0.981
H152	-	-	-	0.019
C16	0.34708	-0.14987	0.08081	1.000
D161	0.23787	-0.18653	0.03844	0.981
H161	-	-	-	0.019
D162	0.44917	-0.15297	0.03925	0.981
H162	-	-	-	0.019
N21	0.29278	0.14565	0.40104	1.000
D211	0.18474	0.13401	0.34310	0.981
H211	-	-	-	0.019
D212	0.40075	0.13762	0.36681	0.981
H212	-	-	-	0.019
C22	0.27946	0.23073	0.43350	1.000
D221	0.27449	0.26902	0.36477	0.981
H221	-	-	-	0.019
D222	0.39506	0.24324	0.49524	0.981
H222	-	-	-	0.019
C23	0.12397	0.24528	0.48998	1.000
D231	0.13316	0.30768	0.51907	0.981
H231	-	-	-	0.019
D232	0.01290	0.23029	0.42953	0.981
H232	-	-	-	0.019
C24	0.12954	0.18274	0.58427	1.000
D241	0.23819	0.19854	0.65459	0.981

Table A.4: (continued)

Atom	x	y	z	Occupation
H241	-	-	-	0.019
D242	0.02166	0.18894	0.62215	0.981
H242	-	-	-	0.019
C25	0.14775	0.09720	0.54954	1.000
D251	0.15454	0.05417	0.61729	0.981
H251	-	-	-	0.019
D252	0.02933	0.07825	0.48674	0.981
H252	-	-	-	0.019
C26	0.29345	0.08587	0.49479	1.000
D261	0.41204	0.09983	0.54953	0.981
H261	-	-	-	0.019
D262	0.30869	0.02611	0.46159	0.981
H262	-	-	-	0.019

Table A.5: Fullprof refinement of atomic positions $(C_5D_{12}N)_2CuCl_4$ for data acquired at 1.8 K. Unit cell parameters are a = 8.08657Å, b = 16.57704Å, c = 12.14457Å, $\alpha = 90°$, $\beta = 102.23950°$, $\gamma = 90°$, Spacegroup = P21/c

Atom	**x**	**y**	**z**	**Occupation**
Cu	0.69111	0.08646	0.24332	1.000
Cl1	0.70154	-0.03292	0.15210	1.000
Cl2	0.94343	0.13458	0.21096	1.000
Cl3	0.42073	0.11639	0.16623	1.000
Cl4	0.69717	0.12635	0.41794	1.000
N11	0.28324	-0.06510	0.06994	1.000
D111	0.25294	-0.04044	-0.00915	1.000
D112	0.37868	-0.02460	0.10460	1.000
C12	0.13406	-0.04538	0.12561	1.000
D121	0.03157	-0.08151	0.07948	1.000
D122	0.10632	0.01847	0.11580	1.000
C13	0.18894	-0.07053	0.25130	1.000
D131	0.07399	-0.06012	0.28669	1.000
D132	0.28688	-0.02844	0.28975	1.000
C14	0.24414	-0.15661	0.26700	1.000
D141	0.29048	-0.16991	0.35269	1.000
D142	0.13908	-0.19696	0.23040	1.000
C15	0.39038	-0.17203	0.20400	1.000
D151	0.42612	-0.23747	0.21654	1.000
D152	0.49816	-0.13830	0.24609	1.000
C16	0.34599	-0.14888	0.08058	1.000
D161	0.23713	-0.18615	0.03681	1.000
D162	0.44593	-0.15291	0.03787	1.000
N21	0.28921	0.14625	0.40007	1.000
D211	0.18146	0.13237	0.34114	1.000
D212	0.39766	0.14030	0.36681	1.000
C22	0.27868	0.23215	0.43714	1.000

Table A.5: (continued)

Atom	x	y	z	Occupation
D221	0.27636	0.26719	0.36524	1.000
D222	0.39895	0.24244	0.49488	1.000
C23	0.12441	0.24518	0.48959	1.000
D231	0.13163	0.30801	0.51824	1.000
D232	0.01142	0.23000	0.42772	1.000
C24	0.12810	0.18232	0.58588	1.000
D241	0.23697	0.19715	0.65329	1.000
D242	0.01975	0.18894	0.62049	1.000
C25	0.15136	0.09767	0.54962	1.000
D251	0.15155	0.05453	0.61802	1.000
D252	0.02900	0.07897	0.48809	1.000
C26	0.29441	0.08563	0.49467	1.000
D261	0.41501	0.09858	0.55150	1.000
D262	0.30762	0.02494	0.46208	1.000

Appendix B

Acknowledgements

First and foremost, I would like to thank my supervisor Prof. Christian Rüegg for the invaluable opportunities which have been presented to me and making this thesis possible. His overwhelming support and encyclopaedic knowledge in all aspects of condensed matter physics and the experimental technique is inspirational. I would also like to thank my advisor, Prof. Des McMorrow who was always available to keep me on track.

This thesis was heavily dependent on experimental work performed at institutions throughout Europe. I would like to thank Martin B "ohm on IN14 at the ILL, Christof Niedermeyer on RITA-II, Denis Cheptiakov on HRPT both at PSI and Kirrily Rule on Flex and Manh Duc Le on Flex2 both previously at HZB. Also I would like to thank Tatiana Guildi on LET at ISIS for the 24 hour support over the long experiments. Without these peoples on-site support, help with data analysis, patient advice and assistance, the data collected here would not be possible. Also, special thanks go to the sample environment teams at all institutions for their patience and ability to deal with our demanding requests.

None of this work would have been possible without high quality samples. I would like to thank Dr. Karl Krämer at the university of Bern for all of his help and for hosting me in his group whilst teaching me about sample growth. I would also like to thank Daniel Biner who has spent months growing endless numbers of samples. The pride and endless enthusiasm for creating the perfect sample is inspirational.

During my time both in the LCN and PSI I had the pleasure of working with many excellent officemates. I would like to thank Simon Gerber for instilling the importance of proper figures, Phil Merchant for revealing scientific discussions, Martin Ruminy for productive discussions and help with the German language. I would

also like to thank Shang Gao for posing interesting questions and keeping my mind open to the broader physics environment.

I would also like to thank my colleagues and friends who have kept me sane throughout this thesis. In no particular order I would like to thank Gwen and Tibo Demoulin, Mattia Mena, Daniel Mazzone, Nicolas Gauthier, Mickaël Morin, Katharina Rolfs, Sandor Toth and all members of the LNS.

I'm also indebted to my family for their constant support, help and all the guidance that they have provided.

Thank you.

References

[1] C. Rüegg *et al.*, Nature **423**, 62 (2003). (Cited on page 2.)

[2] S. E. Sebastian *et al.*, Nature **441**, 617 (2006). (Cited on page 2.)

[3] P. Fazekas, *Lecture Notes on Electron Correlation and Magnetism* (World Scientific, 1999). (Cited on page 2.)

[4] S. Sachdev, Nature Physics **4**, 173 (2008). (Cited on page 3.)

[5] S. Sachdev, *Quantum Phase Transitions* (John Wiley & Sons, Ltd, Chichester, UK, 2007). (Cited on page 3.)

[6] S. R. White, R. M. Noack, and D. J. Scalapino, Physical Review Letters (1994). (Cited on page 3.)

[7] P. Bouillot, *Statics and dynamics of weakly coupled antiferromagnetic spin-1/2 ladders in a magnetic field*, PhD thesis, Springer, Université de Genève, 2013. (Cited on pages 5, 64, 65, 111 and 114.)

[8] D. Schmidiger, S. Muhlbauer, S. N. Gvasaliya, T. Yankova, and A. Zheludev, Physical Review B **84** (2011). (Cited on page 6.)

[9] D. Schmidiger *et al.*, Physical Review Letters **108**, 167201 (2012). (Cited on pages 6 and 7.)

[10] D. Schmidiger *et al.*, Physical Review B **88** (2013). (Cited on page 6.)

[11] D. Schmidiger *et al.*, Physical Review Letters **111**, 107202 (2013). (Cited on page 7.)

[12] S. Notbohm *et al.*, Physical Review Letters **98**, 027403 (2007). (Cited on page 7.)

[13] T. Nunner, P. Brune, T. Kopp, M. Windt, and M. Grüninger, Physical Review B **66**, 180404 (2002). (Cited on page 7.)

[14] T. Vuletić *et al.*, Physics Reports **428**, 169 (2006). (Cited on page 7.)

[15] D. Tennant *et al.*, Physical Review B **67**, 054414 (2003). (Cited on pages 7 and 64.)

[16] B. Willenberg *et al.*, arXiv.org (2014), 1406.6149v1. (Cited on page 7.)

[17] M. B. Stone *et al.*, New Journal of Physics **9**, (2007). (Cited on page 7.)

[18] B. R. Patyal, B. L. Scott, and R. D. Willett, Physical Review B **41**, 1657 (1990). (Cited on pages 8, 32, 33 and 80.)

[19] B. Thielemann *et al.*, Physical Review Letters **102**, 107204 (2009). (Cited on pages 8, 9 and 112.)

[20] C. Rüegg *et al.*, Physical Review Letters **101**, 247202 (2008). (Cited on pages 8, 10, 11 and 111.)

[21] M. Klanjšek *et al.*, Physical Review Letters **101**, 137207 (2008). (Cited on pages 8 and 9.)

[22] E. Čižmár *et al.*, Physical Review B **82**, 054431 (2010). (Cited on pages 8, 10 and 80.)

[23] S. C. Furuya, M. Oshikawa, P. Bouillot, C. Kollath, and T. Giamarchi, Physical Review Letters **108**, 037204 (2012). (Cited on page 8.)

[24] F. Anfuso *et al.*, Physical Review B **77**, 235113 (2008). (Cited on page 8.)

[25] B. Watson *et al.*, Physical Review Letters **86**, 5168 (2001). (Cited on pages 8, 46 and 49.)

[26] B. Thielemann, C. Rüegg, K. Kiefer, and H. Rønnow, Physical Review B (2009). (Cited on pages 9 and 10.)

[27] G. L. Squires, *Introduction to the Theory of Thermal Neutron Scattering* (Cambridge University Press, 2012). (Cited on pages 15, 16 and 17.)

[28] S. W. Lovesey, Theory of Neutron Scattering from Condensed Matter. Vol. 1: Nuclear Scattering, 1984. (Cited on page 15.)

[29] S. W. Lovesey, Theory of Neutron Scattering from Condensed Matter. Vol. 2: Polatization Effects and Magnetic Scattering, 1984. (Cited on page 15.)

[30] A. Furrer, J. Mesot, and T. Strässle, *Neutron scattering in condensed matter physics* (World Scientific). (Cited on page 15.)

[31] W. R. Busing and H. A. Levy, Acta Crystallographica **22**, 457 (1967). (Cited on page 19.)

[32] M. D. Lumsden, J. L. Robertson, and M. Yethiraj, Journal of applied Crystallography **38**, 405 (2005). (Cited on page 19.)

[33] ILL :: Neutrons for science : IN14. (Cited on page 20.)

[34] M. J. Cooper and R. Nathans, Acta Crystallographica **23**, 357 (1967). (Cited on page 21.)

[35] M. Popovici, Acta Crystallographica Section A: Crystal Physics, Diffraction, Theoretical and General Crystallography **31**, 507 (1975). (Cited on page 21.)

[36] E. Bergbäck Knudsen *et al.*, Journal of applied Crystallography **46**, 679 (2013). (Cited on page 21.)

[37] R. I. Bewley, J. W. Taylor, and S. M. Bennington, Nuclear Instruments & Methods in Physics Research Section a-Accelerators Spectrometers Detectors and Associated Equipment **637**, 128 (2011). (Cited on page 23.)

[38] O. Arnold *et al.*, Nuclear Inst. and Methods in Physics Research **764**, 156 (2014). (Cited on page 23.)

[39] O. V. Lounasmaa and O. V. Louasmaa, Experimental principles and methods below 1 K, 1974. (Cited on page 25.)

[40] F. Pobell, *Matter and Methods at Low Temperatures* (Springer Berlin Heidelberg, Berlin, Heidelberg, 2007). (Cited on page 25.)

[41] F. J. Brown, Journal of Physics: Conference Series **251**, 012093 (2010). (Cited on page 26.)

[42] A. T. Holmes, G. R. Walsh, E. Blackburn, E. M. Forgan, and M. Savey-Bennett, Review of Scientific Instruments **83**, 023904 (2012). (Cited on page 26.)

[43] H. Ryll, *Magnetic and Caloric Properties of Ideal and Random Bond Quantum Spin Ladders in a Magnetic Field*, PhD thesis, Mathematik und Naturwissenschaften der Technischen Universitat Berlin, 2012. (Cited on pages 27 and 29.)

[44] M. J. Naughton *et al.*, Review of Scientific Instruments **68**, 4061 (1997). (Cited on page 28.)

[45] A. M. Tishin and Y. I. Spichkin, *The Magnetocaloric Effect and its Applications* (CRC Press, 2003). (Cited on page 29.)

[46] H. Ryll *et al.*, Physical Review B **89**, 144416 (2014). (Cited on pages 30, 52, 54, 56 and 139.)

[47] K. Kiefer, *Kalorimetrische und magnetische Untersuchungen am Spin-Peierls-System CuGeO3*, PhD thesis, Universitaet des Saarlandes, 2004. (Cited on page 30.)

[48] T. Tajiri *et al.*, Journal of Magnetism and Magnetic Materials **272-276**, 1070 (2004). (Cited on pages 32 and 33.)

[49] B. Thielemann, *Spin Ladder Physics*, PhD thesis, ETH Zürich, 2009. (Cited on pages 33, 61, 62, 64, 66 and 90.)

[50] G. W. C. Kaye and T. H. Laby, *Tables of physical and chemical constants and some mathematical functions*, 16 ed. (Longman Publishing Group, 1986). (Cited on page 33.)

[51] T. Komm, D. Biner, A. Neels, and K. Krämer, Crystals **2**, 1434 (2012). (Cited on page 34.)

[52] H. M. Rietveld, Journal of applied Crystallography (1969). (Cited on page 36.)

[53] A. R. West, *Solid State Chemistry and Its Applications* (John Wiley & Sons, 1985). (Cited on page 38.)

[54] M. M. Turnbull, C. P. Landee, and B. M. Wells, Coordination Chemistry Reviews **249**, 2567 (2005). (Cited on pages 40, 41 and 51.)

[55] G. Van Kalkeren, W. W. Schmidt, and R. Block, Physica B+C **97**, 315 (1979). (Cited on page 40.)

[56] B. Koteswararao, S. Salunke, A. Mahajan, I. Dasgupta, and J. Bobroff, Physical Review B **76**, 052402 (2007). (Cited on page 45.)

[57] S. Majumdar *et al.*, Physical Review B **69** (2004). (Cited on page 45.)

[58] N. Maeshima *et al.*, Journal of Physics-Condensed Matter **15**, 3607 (2003). (Cited on page 45.)

[59] D. C. Johnston *et al.*, arXiv.org , 01147 (2000). (Cited on pages 46 and 47.)

[60] B. Normand and C. Rüegg, Physical Review B **83**, 54415 (2011). (Cited on pages 46, 83 and 87.)

[61] B. Bauer *et al.*, Journal of Statistical Mechanics: Theory and Experiment **2011**, P05001 (2011). (Cited on pages 46 and 67.)

[62] A. Bühler, U. Löw, and G. S. Uhrig, Physical Review B **64** (2001). (Cited on page 48.)

[63] A. Klümper and D. Johnston, Physical Review Letters **84**, 4701 (2000). (Cited on page 48.)

[64] J. Piekarewicz and J. R. Shepard, Physical Review B **58**, 9326 (1998). (Cited on pages 52 and 53.)

[65] L. Zhu, M. Garst, A. Rosch, and Q. Si, Physical Review Letters **91**, 066404 (2003). (Cited on page 55.)

[66] M. Garst and A. Rosch, Physical Review B **72**, 205129 (2005). (Cited on page 56.)

[67] F. Weickert *et al.*, Physical Review B **85**, 184408 (2012). (Cited on page 56.)

[68] B. Wolf *et al.*, Proceedings of the National Academy of Sciences **108**, 6862 (2011). (Cited on page 56.)

[69] T. Giamarchi, *Quantum Physics in One Dimension* (Clarendon Press, 2003). (Cited on pages 57 and 110.)

[70] M. Reigrotzki, H. Tsunetsugu, and T. M. Rice, Journal of Physics-Condensed Matter **6**, 9235 (1994). (Cited on pages 59 and 67.)

[71] M. Muller and H. J. Mikeska, Journal of Physics-Condensed Matter **12**, 7633 (2000). (Cited on pages 61 and 63.)

[72] N. Cavadini *et al.*, The European Physical Journal B - Condensed Matter and Complex Systems **7**, 519 (1999). (Cited on page 61.)

[73] J. Oitmaa, R. Singh, and W. H. Zheng, Physical Review B **54**, 1009 (1996). (Cited on pages 62 and 64.)

[74] M. Zhitomirsky, Physical Review B **73**, 100404 (2006). (Cited on page 63.)

[75] M. B. Stone, I. A. Zaliznyak, T. Hong, C. L. Broholm, and D. H. Reich, Nature **440**, 187 (2006). (Cited on page 63.)

[76] T. Barnes, E. Dagotto, J. Riera, and E. Swanson, Physical Review B **47**, 3196 (1993). (Cited on pages 64 and 142.)

[77] P. Hammar, D. Reich, C. Broholm, and F. Trouw, Physical Review B **57**, 7846 (1998). (Cited on page 64.)

[78] B. Leuenberger, H. U. Güdel, R. Feile, and J. Kjems, Physical Review B **28**, 5368 (1983). (Cited on page 66.)

[79] B. Leuenberger *et al.*, Physical Review B **30**, 6300 (1984). (Cited on page 66.)

[80] N. Cavadini *et al.*, Physica B: Condensed Matter **276-278**, 540 (2000). (Cited on page 66.)

[81] B. Normand and C. Rüegg, Physical Review B **83**, 054415 (2011). (Cited on pages 67 and 74.)

[82] W. Zheng, C. Hamer, R. Singh, S. Trebst, and H. Monien, Physical Review B **63**, 144410 (2001). (Cited on page 67.)

[83] K. Damle and S. E. Nagler, arXiv.org , 04438 (1999). (Cited on page 67.)

[84] B. Normand, Quantum antiferromagnets in a magnetic field, in *Acta Physica Polonica B*, pp. 3005–3019, 2000. (Cited on page 78.)

[85] S. Miyahara *et al.*, Physical Review B **75**, 184402 (2007). (Cited on page 80.)

[86] P. W. Anderson, Local Moments and Localized States, in *Nobel Lecture*, p. 1, 1978. (Cited on page 84.)

[87] T. Hara, Solid State Communications **132**, 109 (2004). (Cited on page 84.)

[88] D. Hüvonen *et al.*, Physical Review B **86**, 214408 (2012). (Cited on pages 84, 87, 88, 90 and 107.)

[89] X. Feng, Z. Xu, and J. Dai, Journal of Physics-Condensed Matter **16**, 4245 (2004). (Cited on page 84.)

[90] M. Azzouz, K. Shahin, and G. Chitov, Physical Review B **76**, 132410 (2007). (Cited on page 84.)

[91] K. Trinh, S. Haas, R. Yu, and T. Roscilde, Physical Review B **85**, 035134 (2012). (Cited on page 86.)

[92] M. Fujisawa *et al.*, Journal of Physics: Conference Series **150**, 042034 (2009). (Cited on page 86.)

[93] K. Trinh and S. Haas, Physical Review B **87**, 075137 (2013). (Cited on page 86.)

[94] K. Trinh, S. Haas, R. Yu, and T. Roscilde, Physical Review B **85**, 035134 (2012). (Cited on pages 87 and 89.)

[95] D. A. Tennant *et al.*, Physical Review B **85**, 014402 (2012). (Cited on page 90.)

[96] D. L. Quintero-Castro *et al.*, Physical Review Letters **109**, 127206 (2012). (Cited on page 90.)

[97] F. Essler and R. Konik, Physical Review B **78**, 100403 (2008). (Cited on page 90.)

[98] B. Náfrádi, T. Keller, H. Manaka, U. Stuhr, and A. Zheludev, Physical Review B **87**, 020408 (2013). (Cited on page 90.)

[99] Y. Sasago, K. Uchinokura, A. Zheludev, and G. Shirane, Physical Review B **55**, 8357 (1997). (Cited on page 90.)

[100] G. Xu, C. Broholm, D. Reich, and M. Adams, Physical Review Letters **84**, 4465 (2000). (Cited on page 90.)

[101] N. Cavadini *et al.*, The European Physical Journal B - Condensed Matter and Complex Systems **18**, 565 (2000). (Cited on page 90.)

[102] M. Vojta, Physical Review Letters **111**, 097202 (2013). (Cited on pages 91, 92 and 105.)

[103] T. Giamarchi, C. Rüegg, and O. Tchernyshyov, Nature Physics **4**, 198 (2008). (Cited on page 92.)

[104] T. Giamarchi and H. J. Schulz, Physical Review B **37**, 325 (1988). (Cited on page 92.)

[105] M. P. A. Fisher, G. Grinstein, and D. S. Fisher, Physical Review B **40**, 546 (1989). (Cited on page 92.)

[106] B. Kramer and A. MacKinnon, Reports on Progress in Physics **56**, 1469 (1993). (Cited on page 92.)

[107] R. Yu *et al.*, Nature **489**, 379 (2012). (Cited on page 93.)

[108] P. Hitchcock and E. S. Sorensen, Physical Review B **73** (2006). (Cited on page 93.)

[109] S. Morrison *et al.*, New Journal of Physics **10**, 073032 (2008). (Cited on page 93.)

[110] A. Zheludev and T. Roscilde, Comptes Rendus Physique **14**, 740 (2013). (Cited on page 93.)

[111] A. Furrer *et al.*, Physical Review Letters **107**, 115502 (2011). (Cited on page 99.)

[112] A. Azzalini, Scandinavian journal of statistics **12**, 171 (1985). (Cited on page 100.)

[113] S. Ward, S. Furuya, T. Giamarchi, and C. Rüegg, Private correspondence . (Cited on page 101.)

[114] L. D. Landau, Soviet Physics Jetp-Ussr **3**, 920 (1957). (Cited on page 110.)

[115] L. D. Landau, Soviet Physics Jetp-Ussr **5**, 101 (1957). (Cited on page 110.)

[116] C. Kittel and P. McEuen, Introduction to solid state physics, 1976. (Cited on page 110.)

[117] E. Levy *et al.*, Physical Review B **85**, 045315 (2012). (Cited on page 111.)

[118] M. Bockrath *et al.*, Nature **397**, 598 (1999). (Cited on pages 111 and 129.)

[119] R. Konik and P. Fendley, Physical Review B **66**, 144416 (2002). (Cited on page 111.)

[120] M. Jeong *et al.*, Physical Review Letters **111**, 106404 (2013). (Cited on page 111.)

[121] D. A. Tennant, T. G. Perring, and R. A. Cowley, Physical Review Letters **70**, 4003 (1993). (Cited on page 112.)

[122] B. Bellazzini, M. Mintchev, and P. Sorba, Journal of Physics A: Mathematical and Theoretical **40**, 2485 (2007). (Cited on page 112.)

[123] S. Das Sarma and A. Pinczuk, *Perspectives in Quantum Hall Effects*Novel Quantum Liquids in Low-Dimensional Semiconductor Structures (Wiley, Weinheim, Germany, 1996). (Cited on page 112.)

[124] O. Zachar, S. Kivelson, and V. Emery, Physical Review Letters **77**, 1342 (1996). (Cited on page 112.)

[125] T. Giamarchi, *Quantum Physics in One Dimension* (Clarendon Press, 2003). (Cited on page 112.)

[126] J. von Delft and H. Schoeller, Annalen der Physik **7**, 225 (1998). (Cited on page 112.)

[127] K. Schonhammer, arXiv.org , 10330 (1997), cond-mat/9710330. (Cited on page 112.)

[128] J.-S. Caux, R. Hagemans, and J. M. Maillet, Journal of Statistical Mechanics: Theory and Experiment **2005**, P09003 (2005). (Cited on page 113.)

[129] P. Bouillot *et al.*, Physical Review B **83**, 54407 (2011). (Cited on page 114.)

[130] T. Giamarchi and A. M. Tsvelik, Physical Review B **59**, 11398 (1999). (Cited on page 121.)

[131] S. Ward *et al.*, Journal of Physics-Condensed Matter **25**, 4004 (2013). (Cited on pages 128 and 139.)

[132] Z. Yao, H. W. C. Postma, L. Balents, and C. Dekker, Nature **402**, 273 (1999). (Cited on page 129.)

[133] M. Kindermann and P. Brouwer, Physical Review B **74**, 115121 (2006). (Cited on page 129.)

[134] A. E. Feiguin and G. A. Fiete, Physical Review B **81**, 075108 (2010). (Cited on pages 129 and 136.)

[135] G. A. Fiete, Reviews of Modern Physics **79**, 801 (2007). (Cited on page 130.)

[136] A. Feiguin and S. White, Physical Review B **72**, 020404 (2005). (Cited on page 131.)

[137] S. R. White and A. E. Feiguin, Physical Review Letters **93**, 076401 (2004). (Cited on page 131.)

[138] B. Lake, D. A. Tennant, C. D. Frost, and S. E. Nagler, Nature Materials **4**, 329 (2005). (Cited on pages 131, 140 and 141.)

[139] R. Pereira *et al.*, Physical Review Letters **96**, 257202 (2006). (Cited on page 132.)

[140] S. Sachdev, T. Senthil, and R. Shankar, Physical Review B **50**, 258 (1994). (Cited on page 140.)

[141] K. Y. Povarov, D. Schmidiger, N. Reynolds, A. Zheludev, and R. Bewley, arXiv.org , 6876 (2014), 1406.6876. (Cited on pages 140 and 141.)

[142] E. Dagotto and T. M. Rice, Science **271**, 618 (1996). (Cited on page 142.)

[143] E. Dagotto, J. Riera, and D. Scalapino, Physical Review B (Condensed Matter) **45**, 5744 (1992). (Cited on page 142.)

[144] J L Manson *et al.*, Inorganic Chemistry **46**, 213 (2006). (Cited on page 143.)